INFORMATION TO USERS

This manuscript has been reproduced from the microfilm master. UMI films the text directly from the original or copy submitted. Thus, some thesis and dissertation copies are in typewriter face, while others may be from any type of computer printer.

The quality of this reproduction is dependent upon the quality of the copy submitted. Broken or indistinct print, colored or poor quality illustrations and photographs, print bleedthrough, substandard margins, and improper alignment can adversely affect reproduction.

In the unlikely event that the author did not send UMI a complete manuscript and there are missing pages, these will be noted. Also, if unauthorized copyright material had to be removed, a note will indicate the deletion.

Oversize materials (e.g., maps, drawings, charts) are reproduced by sectioning the original, beginning at the upper left-hand corner and continuing from left to right in equal sections with small overlaps.

Photographs included in the original manuscript have been reproduced xerographically in this copy. Higher quality 6" x 9" black and white photographic prints are available for any photographs or illustrations appearing in this copy for an additional charge. Contact UMI directly to order.

ProQuest Information and Learning
300 North Zeeb Road, Ann Arbor, MI 48106-1346 USA
800-521-0600

THREE-DIMENSIONAL POSITION SENSITIVE CdZnTe GAMMA RAY SPECTROMETERS

by

Wen Li

A dissertation submitted in partial fulfillment
of the requirements for the degree of
Doctor of Philosophy
(Nuclear Engineering and Radiological Sciences)
in The University of Michigan
2001

Doctoral Committee:

Associate Professor David K. Wehe, Chairman
Assistant Professor Zhong He
Professor Glenn F. Knoll
Professor W. Leslie Rogers

UMI Number: 3016903

UMI Microform 3016903

Bell & Howell Information and Learning Company
300 North Zeeb Road
P.O. Box 1346
Ann Arbor, MI 48106-1346

ACKNOWLEDGEMENTS

First of all, I am forever grateful to my advisor, Dr. David Wehe, for his inspiring and encouraging way to guide me through my graduate studies, and his invaluable comments during the whole work with this dissertation. I am also deeply indebted to Dr. Zhong He for his knowledgeable guidance and mentoring in the research works related to this dissertation. Also I would like to thank the other members of my committee, Dr. Leslie Rogers and Dr. Glenn Knoll for their great help and guidance in the preparation of this dissertation. I would like to acknowledge the help and support from: Mr. Jim Berry, Dr. Douglas McGregor, Dr. Jose Perez and Dr. Alex Bielajew. In addition, I am grateful to a number of former and fellow students for their support and encouragement, namely: Dr. Eric Smith, Dr. Jim LeBlanc, Yanfeng Du, Clair Sullivan, Jim Baciak and Mark Hammig. Lastly, I would like to thank all department staff and especially Ms. Pat Moore for their help regarding this research.

This research was performed while I was under the financial support from US DOE Grants DOE-FG08-94NV13357 and DOE-FG08-98NV13357. In my last year working on the dissertation, I was appointed to the Rackham Predoctoral Fellowship program of the University of Michigan, with additional support from US DOE Grant DOE-FG08-98NV13357. The financial support was greatly appreciated.

TABLE OF CONTENTS

LIST OF FIGURES

Figure

LIST OF TABLES

CHAPTER I

INTRODUCTION

In many gamma-ray spectroscopy applications, an ideal gamma-ray detector should have high energy resolution, high gamma-ray detection efficiency, and low cost. High energy resolution currently implies a semiconductor detector. High gamma-ray detection efficiency requires it to consist of high atomic number materials and have high density. For a semiconductor detector, low operational cost requires that it can work at room temperature. To date, the most widely used semiconductor detectors are Si and Ge detectors. Neither of them is an ideal gamma-ray detector according to the above criteria. The atomic number of Si is too low (Z=14) for gamma-ray detection over a broad energy range, and the Ge detectors need to be operated under liquid nitrogen temperature because of the small band gap of Ge (0.74 eV). In theory, it is possible to find certain high atomic number semiconductors with proper band gap ($\sim$1.5 eV), that can be operated as radiation detectors at room temperature without much loss of energy resolution.

1.1 Room Temperature Semiconductor Materials

In last four decades, extensive efforts have been devoted to the investigation and development of wide band gap, high atomic number semiconductor materials that

can be used as radiation detectors. To date, there are three room temperature semiconductor materials, namely HgI_2, CdTe, CdZnTe, which can be used to fabricate gamma-ray detectors larger than tens of cubic millimeters in volume and demonstrate good energy resolution[Sak.1][Cuz.1][But.1]. Table 1.1 shows the characteristics of the three materials, as well as those of Si and Ge[Kno.1][Sak.1][Eis.1].

The wide band gap and high atomic number of a semiconductor material does not guarantee it can be used to build superior gamma-ray detectors. In practice, the performance of the detector heavily depends on the mobility-life time products of the charge carriers, the resistivity and uniformity of the materials. The mobility-life time product determines the charge collection efficiency for a fixed drift distance of the charge carriers and electric field in the detector. To get higher charge collection efficiency in a detector, a stronger electric field is needed which requires higher detector bias. At a fixed detector bias, the resistivity of the detector material determines the leakage current and the associated noise from the detector. Thus, resistivity of the material usually sets the limit on the maximum bias which can be applied to the detector.

HgI_2 usually has very high resistivity because of its large band gap (2.13 eV). With this high resistivity, HgI_2 can withstand a very high detector bias (e.g., more than 2000 V across 0.5 mm crystal). For a $10\times 8 \times 0.5$ mm^3 HgI_2 detector with 2700 V bias, an energy resolution of 4.5 keV FWHM at 662 keV has been achieved[Sch.1]. For larger detectors with increased thickness, the detector performance suffers from the trapping of holes due to its inherently poor hole mobility-life time product[Arm.1]. A further degradation of the detector performance with time has also been reported[Bra.1], which is caused by the polarization effect (buildup of space charge from the charge carriers trapped in the detector).

Table 1.1: Characteristics of some semiconductor materials used as detectors.

	Si	Ge	HgI_2	$CdTe$	$Cd_{0.9}Zn_{0.1}Te$
Atomic Number	14	32	80,53	48,52	48,30.52
Density (g/cm^3)	2.33	5.32	6.4	6.06	6.06
Operating Temperature (K)	300	77	300	300	300
Band Gap (eV)	1.12	0.74	2.13	1.47	1.70
Average Energy Per e-h Pair (eV)	3.61	2.98	4.2	4.43	4.7
Electron Mobility (cm^2/Vs)	1350	3.6×10^4	100	1100	1100
Hole Mobility (cm^2/Vs)	480	4.2×10^4	4	100	100
Electron Mobility-Life Time Product (cm^2/V)	2.7×10^{-2}	0.72	10^{-4}	10^{-3}	10^{-3}
Hole Mobility-Life Time Product (cm^2/V)	9.6×10^{-3}	0.84	10^{-5}	5×10^{-5}	3×10^{-5}

CdTe material grown by the travelling heater method has the high resistivity (10^8-10^9 $\Omega\cdot$ cm) desired to build large volume gamma-ray detectors[Cuz.1]. An energy resolution of 8.5 keV FWHM at 662 keV was reported for a CdTe detector of 5 mm diameter $\times$ 5 mm thickness[Wal.1]. Similar to HgI_2, CdTe detector also has the problems of hole trapping and polarization[Bel.1][Mal.1][Sif.1]. But with its lower resistivity, the leakage current limits increasing charge collection by increasing the detector bias.

CdZnTe is a comparatively new material in this field, introduced after the discovery that alloying CdTe with ZnTe leads to crystaline CdZnTe with improved material properties[But.1][But.2]. Compared with CdTe, CdZnTe has a higher band gap (1.70 eV), and thus higher resistivity ($\sim 10^{11}$ $\Omega\cdot$ cm)[Eis.1]. By using the new high pressure Bridgman method (HPBM), large detector grade CdZnTe crystals have been grown[Ton.1][Chi.1]. More importantly, although thick CdZnTe detectors still suffer from the trapping of holes, they do not exhibit polarization effects[But.1]. Because of these advantages, CdZnTe quickly became a promising material for large volume, room temperature gamma-ray detectors and has attracted most of the detector research interest in recent years. In order to achieve better spectroscopic performance from large CdZnTe detectors built using the commercially available CdZnTe, three problems need to be addressed: severe hole trapping, electron trapping, and material non-uniformity.

1.2 Severe Hole Trapping

In order to get good detection efficiency for gamma rays, thick(5 mm) detector material is desired. For example, a cubic CdZnTe detector of volume 1 cm^3 has $\sim$65% overall detection efficiency and $\sim$8% photopeak efficiency for 662 keV gamma

rays. However, for thick conventional planar room temperature semiconductor detectors, spectroscopic performance is severely limited by the poor collection of holes. The performance degradation is especially significant for high energy gamma-rays, because their interactions spread over the whole detector depth. This hole collection problem was initially addressed by pulse processing techniques[Jon.1][War.1][Lun.1]. The idea is based on the monotonic relationship between the interaction depth and the pulse rise time of the anode signal. In practice, the pulse rise time is derived for each event and the result is used to compensate the pulse amplitude for hole trapping or reject those events near the anode having poor signal-to-noise ratios. While this method produces some improvement in energy resolution, it involves the loss of active detector volume, and does not solve the problem of the degradation of signal-to-noise ratio due to hole trapping. In recent years, another approach called single polarity charge sensing has been developed. This approach has proven to be a more effective solution to the hole collection problem.

The idea of single polarity charge sensing is to get uniform detector response (independent of interaction depth) by sensing only the contribution from electron motion. The transport properties of the much slower holes have no impact on the spectroscopic performance of the detector. This concept can be realized in room temperature semiconductor detectors by implementing special electrode geometries. Most of the recent work has been concentrated on large volume ($\geq$1 cm^3) CdZnTe detectors. The first example of this approach is the coplanar-grid detector invented by P.N. Luke in 1994[Luk.1][Luk.2]. The anode of a coplanar-grid detector consists of two groups of parallel strips, arranged in an interdigitated pattern. During operation, the two groups of strips are relatively biased by a few tens of volts. The group with higher potential serves as the collecting electrode, the other set forms the non-

collecting electrode. In practice, the difference of the signals from the collecting and non-collecting anodes is the single polarity charge sensing readout. For interaction events occurring in most of the detector volume, the difference signal is proportional to the number of electrons arriving the anode and is independent of the motion of holes. As a result, the problem of severe hole trapping is avoided.

The single polarity charge sensing effect was also achieved using pixellated detectors by H.H. Barrett in 1994[Bar.1] by choosing the size of the anode pixel to be much smaller than the detector thickness. This "small pixel effect" has been exploited by others, showing good spectroscopic performance can be achieved from the small anode pixels despite poor collection of holes[Mar.1][Apo.1]. A very similar result was found in detectors with thin strip anodes when the signal from each anode strip was read out separately[He.1].

Other single polarity charge sensing geometries have also been developed for room temperature semiconductor detectors. These include hemispherical detectors[Hag.1], Frisch grid detectors[Mcg.1][Mcg.2][Lee.1], and detectors with an extended surface cathode[Par.1]. While significant improvements in the spectroscopic performance are demonstrated when compared to the conventional planar readout, these other geometries are inherently limited by either small detector volume or a nonuniform electric field in the detector.

1.3 Electron Trapping

While the approaches of single polarity charge sensing mitigate the problem of poor hole transport, the trapping of electrons can also be an issue for thicker detectors. As an example, for a CdZnTe detector of 1 cm thickness and -2000 V cathode bias, typically ~15% of those electrons generated near the cathode will not be col-

lected at the anode due to electron trapping. This means even if the problem of hole trapping is eliminated using a single polarity charge sensing anode, the pulse height of the anode signal still may vary by 15% for the same energy deposition depending upon the interaction depth. This variation due to electron trapping will cause significant degradation of the energy resolution in the gamma spectrum if the gamma rays interact with the detector at random detector depths. This problem must be solved if high energy resolution is to be achieved.

In coplanar grid detectors, a partial solution to this problem is to use an adjustable gain in the subtraction of the signals from the collecting and non-collecting electrodes[Luk.1]. By using a smaller gain on the non-collecting signal, the subtraction will yield smaller net signals for the events near the anode. This effect can be used to approximately compensate for electron trapping. In pixellated detectors, the signal generated from the anode pixel also has the tendency to yield smaller signal for the events near the anode, especially when the ratio of the pixel size to detector thickness is not small enough. This effect tends to compensate for the electron trapping under certain detector bias and helps to achieve improved energy resolution from the anode pixel[Sho.1].

A more general approach was proposed by Z. He to solve the problem of electron trapping. For this method, the interaction depth is determined for each event and used to correct the pulse height for electron trapping[He.2]. This approach can be applied to room temperature semiconductor detectors with a single polarity charge sensing anode and a conventional planar cathode. For an energy deposition in the detector, the interaction depth can be determined by the ratio of the signals from the cathode and anode pixel (C/A ratio). Using this technique, an energy resolution of 11.8 keV FWHM (1.79%) at 662 keV was achieved from a 1 cubic centimeter

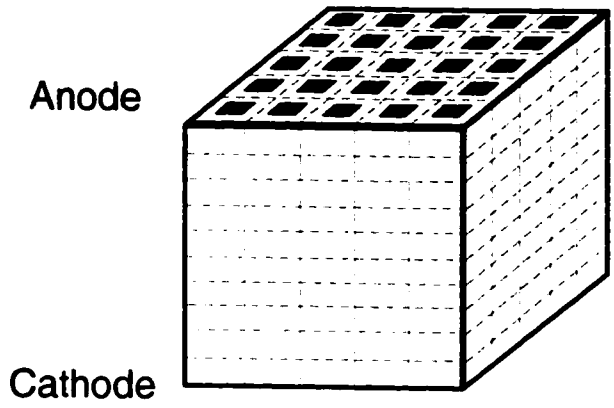

Figure 1.1: Interaction position sensing in 3-D.

CdZnTe detector with a coplanar-grid anode[He.3].

1.4 Material Non-uniformity

The single polarity charge sensing techniques and the corrections for electron trapping have been implemented on large volume CdZnTe detectors and yielded the best energy resolution to date. Further improvements in the energy resolution for these larger volume CdZnTe detectors are limited by the quality of the CdZnTe material. Crystal defects and inhomogeneities are still generally observed in commercially available CdZnTe materials. Those material non-uniformities cause nonuniform electron generation and transport in CdZnTe detectors and contribute to the degradation of energy resolution[Luk.2][Amm.1][Bur.1]. In theory, if it is possible to determine the interaction location in three dimensions in the detector, a 3-D pulse height correction could be applied to mitigate the problem of material non-uniformity. In order to achieve better spectroscopic performance, there is a motivation to develop CdZnTe detectors with a 3-D position sensitivity to the interaction locations.

While it is impossible to determine the 3-D interaction locations from the coplanar-grid detectors, 3-D position sensing can be achieved by applying the interaction depth sensing technique to pixellated CdZnTe detectors[He.1]. For each gamma-ray interaction in the detector, the interaction location in the lateral dimension (parallel to the anode or cathode plane) can be determined by the coordinates of the anode pixel yielding the signal. The interaction depth can be determined by the ratio of the signals from the cathode and anode pixel. With the information about the 3-D interaction location, the whole detector volume can be virtually divided into small voxels, as illustrated in figure 1.4. The energy spectrum from each voxel can be collected separately. The voxel-based variation of the photo peak centroid reflects the 3-D variation of the detector response, which includes electron trapping, non-ideal single polarity charge sensing, and material non-uniformity. Knowing the 3-D variation of the photopeak centroid a priori would permit the 3-D pulse height correction during the spectrum collection. By this means, better spectroscopic performance should be expected from this kind of 3-D position sensitive gamma-ray spectrometer.

1.5 Focus of This Research

This research has two goals. The first goal is to achieve a good understanding of the underlying principles of the 3-D CdZnTe detector by modeling its operation. The second goal is to identify and overcome the problems in the development and operation of the 3-D position sensitive gamma-ray spectrometers. The work presented here covers three parts: the theoretical background and modeling of the 3-D CdZnTe detectors (Chapters 2 and 3), the design and development of two generations of the 3-D position sensitive CdZnTe gamma-ray spectrometers (Chapters 4 and 5), and experiments using the 3-D CdZnTe spectrometers and the analysis of the results

(Chapter 6).

In particular, Chapter 2 presents the theoretical background needed to understand the 3-D position sensitive CdZnTe detectors. As a tool for deriving the induced signals at the electrodes due to the motion of charges in the detector, the Shockley-Ramo theorem is introduced first, followed by introductions to the single polarity charge sensing technology and its different implementations for various room temperature semiconductor detector geometries. The principles of interaction depth sensing by the C/A ratio and by electron drift time are then presented and discussed. The final part of Chapter 2 is a discussion of methods for determining the mobility and lifetime of electrons in the 3-D CdZnTe detectors.

Chapter 3 presents our modeling of the 3-D CdZnTe detectors. The first part is an introduction to the Monte Carlo simulations performed using EGS4[EGS.1]. The objective of the simulation is to investigate the gamma-ray detection efficiency and the fraction of multiple-pixel events in the 3-D CdZnTe detectors. The simulation results show that the reconstruction of multiple-pixel events is necessary to avoid significant photopeak efficiency loss. The second part of Chapter 3 covers the modeling of the signals from the cathode and anode pixels due to the motions of the charge carriers in the detector. Based on that, interaction depth sensing by the C/A ratio method and by measuring the electron drift time are modeled separately. The modeling results demonstrate that both depth sensing techniques can be used to determine the interaction depth for single-pixel events, and depth sensing by electron drift time can be used to locate the multiple interaction depths for multiple-pixel events.

Chapter 4 introduces the design and development of the two generations of the 3-D CdZnTe detectors. Each of the first generation 3-D CdZnTe detectors was devel-

oped with an 11×11 pixellated anode, a cathode and a ceramic substrate surrounding the anode electrode. Each anode pixel was wirebonded to the substrate and the substrate was connected to the front-end circuits through wirebonding. The design and implementation of a non-collecting grid electrode at the anode is also discussed. Compared to the first generation 3-D detectors, the second generation detector has the same general structure, but with larger detector volume and larger anode pixel size. In addition, the connections between the anode pixels and the substrate are improved by using the technique of plate-through-via instead of wirebonding.

Chapter 5 describes the two generations of our readout electronics. The first generation readout system was developed based on a 128-channel integrated readout chip (VA1) from IDE AS[IDE.1]. The working principle of the VA1 chip is introduced first. The trigger signal, electronic noise, and the software of the readout system are described and discussed. Compared to the first generation readout system, the second generation system was designed and developed with improved energy readout channels and new timing readout channels based on VAS-TAT chip pairs. The second generation system has the new functions of self-triggering, peak-hold and multi-channel timing readout, which enable the reconstruction of multiple-pixel events in the 3-D CdZnTe detectors.

Chapter 6 presents the experimental results from the two generations of the 3-D CdZnTe gamma-ray spectrometers and discussions about the results. The investigations of the interaction depth sensing techniques are introduced first, which include the measurement of the correlation between the C/A ratio and the electron drift time, and an experiment using collimated gamma rays. The results clearly demonstrate the effectiveness of both depth sensing techniques. The second part of Chapter 6 reports on the energy resolutions from single-pixel events, which include the collec-

tion of the energy spectrum with 3-D pulse height correction and the investigation of the spatial variation of the energy resolution. The third part of Chapter 6 shows the measurement of the electron mobility-lifetime product and its variation across the detector. Using the results from this chapter, the material non-uniformity of the CdZnTe crystals and the importance of the 3-D pulse height correction in spectrum collection are clearly demonstrated. The measured fraction of multiple-pixel events as a function of the number of pixels involved is presented, as well as the measured signal sharing in the two-pixel events. The results are seen to match well with the modeling results. It is demonstrated that depth sensing by electron drift time can be used to reconstruct the multiple interaction depths of a multiple-pixel event, if the timing signals from all the involved pixels are available. The reconstruction of the energy spectrum from the two-pixel events is investigated and the result is discussed.

Chapter 7 is a summary of the major results of this dissertation work. It also includes discussions of recommended future work.

CHAPTER II

THEORY

2.1 Signal Generation Due to Charge Motion

In an ionization radiation detector, the motion of the charge carriers generated by an energy deposition should cause the variation of the induced charges at the detector electrodes. Typically, the variation of the induced charge at an electrode is read out by a charge sensitive preamplifier as the signal associated with the original energy deposition. To understand the signal generated from the motion of the charge carriers, we should first understand the variation of the induced charge as function of the location of the charge carriers in the detector. For a detector with fixed geometry, this induced charge distribution can be described using the Shockley-Ramo theorem[Ram.1][Sho.2].

2.1.1 Shockley-Ramo Theorem

Before introducing Schockley-Ramo theorem, let us first look at a very important concept: weighting potential. Consider a detector fabricated with several electrodes noted as A, B, C, D, as illustrated in figure 2.1 (a). The weighting potential associated with an arbitrarily selected electrode (e.g., electrode C) is defined as the potential distribution in the detector with the potential of the selected electrode set to 1 and the potentials of all other electrodes set to 0, and without any space charge in the

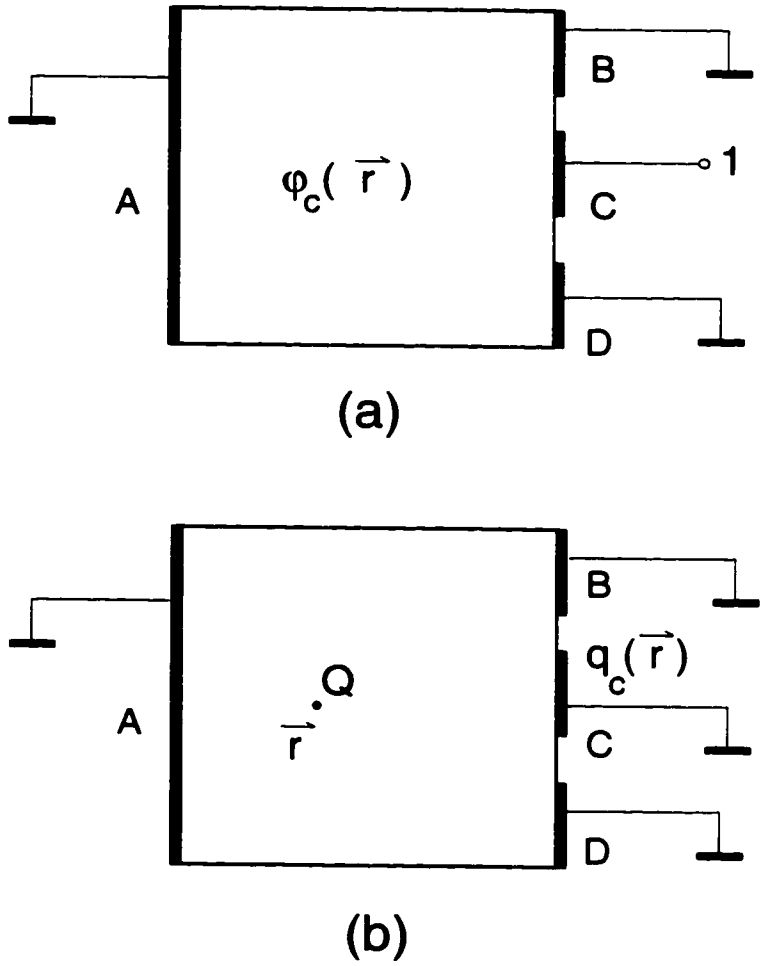

Figure 2.1: Illustration of Shockley-Ramo theorem. (a) Geometry to calculate weighting potential of electrode C. (b) Induced charge at electrode C.

detector. Therefore the weighting potential has a value between 0 and 1, and has no units. As an example, the weighting potential of the electrode C, $\varphi_c(\vec{r})$, can be uniquely determined by solving the Laplace equation:

$$\nabla^2 \varphi_c(\vec{r}) = 0 \tag{2.1}$$

with the following boundary conditions:

$$\begin{cases} \varphi_c(A) = 0 \\ \varphi_c(B) = 0 \\ \varphi_c(C) = 1 \\ \varphi_c(D) = 0 \end{cases} \tag{2.2}$$

According to Shockley-Ramo theorem, if all the electrodes of the detector are biased with constant potentials, the induced charge at an electrode due to a point space charge in the detector can be determined from the weighting potential produced by that electrode. As illustrated in figure 2.1 (b), with all the electrodes grounded, the induced charge on the electrode C due to a point space charge Q at location $\vec{r}$ will be:

$$q_c(\vec{r}) = -Q \cdot \varphi_c(\vec{r}) \tag{2.3}$$

The weighting potential $\varphi_c(\vec{r})$ is only determined by the geometry of the detector, so the induced charge $q_c(\vec{r})$ due to Q has nothing to do with other space charges in the

detector. $q_c(\vec{r})$ is also independent of the actual potentials applied to the electrodes. During the operation of the detector, the actual potentials at the electrodes define the operating potential in the detector, which determines the operating electric field and the trajectory of the charge carriers. Once the trajectory of a charge carrier is determined, the variation of the induced charge at an electrode due to the motion of this charge carrier can then be determined from the variation of the weighting potential along the trajectory.

2.1.2 Transport of Charge Carriers

To predict the actual signal currents from the electrodes, knowledge of the weighting potential and operating potential is not enough. We also need knowledge of the transport of the charge carriers in the detector. In semiconductor materials, the transport of the charge carriers (electrons and holes) can be described by two parameters: the mobility μ and the lifetime τ (we ignore detrapping). The mobility μ determines the drift velocity $\vec{v}$ of the charge carrier in an electric field $\vec{E}$. With low-to-moderate electric field intensity, $\vec{v}$ is simply proportional to $\vec{E}$:

$$\vec{v} = \mu\vec{E} \tag{2.4}$$

The lifetime τ is used to describe the trapping of charge carriers. If P denotes the probability of a charge carrier not being trapped during the time period t after its generation, P can be determined by τ as:

$$P(t) = e^{-t/\tau} \tag{2.5}$$

If the electric field is uniform in the detector, the drift velocity of the charge carrier should be constant. Thus the drift time t of the charge carrier should be proportional to the drift distance z: $t = z/(\mu E)$. Then P can be expressed as:

$$P = e^{-\frac{z}{(\mu\tau)E}} \tag{2.6}$$

In this case, $(\mu\tau)E$ is referred as mean drift length of the charge carrier. For the example shown in figure 2.1, if μ and τ are known, the signal current from the electrode C can be derived from equation 2.3 as:

$$i_c(t) = \frac{\Delta q_c(\vec{r})}{\Delta t} = -Q\mu\vec{E} \cdot \nabla\varphi_c(\vec{r}) \tag{2.7}$$

2.1.3 Conventional Planar Readout

The conventional planar readout in room temperature semiconductor detectors can be explained in terms of its weighting potential. Let us consider a conventional planar detector in figure 2.2 (a). At a normalized depth z ($0 \leq z \leq 1$, normalized to detector thickness) and assuming we read out the signal from the anode, the weighting potential φ(z) of the anode electrode should be proportional to z as shown in figure 2.2 (b). Since the signal read out from the anode is the variation of the induced charge, and this is proportional to the variation of the weighting potential along the trajectory of the charge carriers, the signal contributed by the motion of a charge in the conventional planar detector should be proportional to the drift distance of that charge. Assume n electron-hole pairs are generated at depth z by

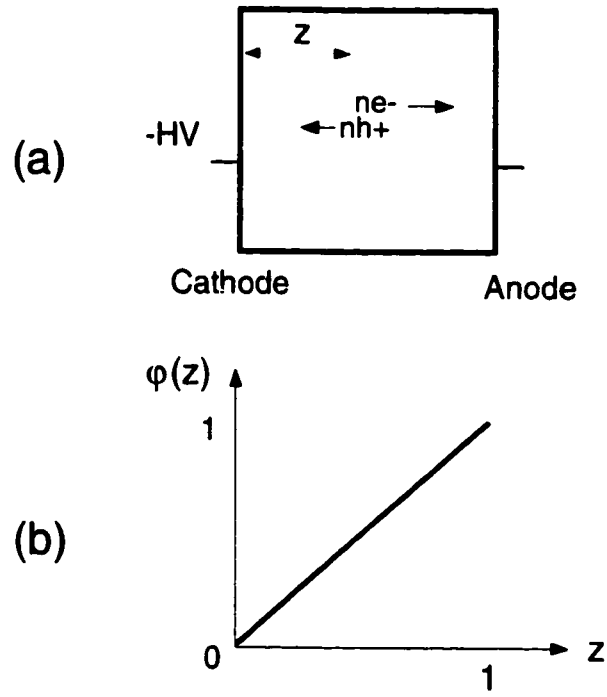

Figure 2.2: Conventional planar detector: (a) Electrode configuration. (b) Weighting potential of the anode electrode.

an energy deposition. If there is no charge loss, the signal from the anode, q_a, will be:

$$q_a = ne(1 - z) + nez = ne \tag{2.8}$$

The first term is the contribution from electrons and is proportional to the drift distance of electrons, $(1 - z)$. The second term is the contribution from holes and is proportional to the drift distance of holes, z. The overall signal is independent of z and only determined by the number of charge carriers generated n, which is proportional to the original energy deposition. This makes the detector a perfect spectrometer. However, for a room temperature semiconductor detector, the trapping of holes is so severe that the overall signal is mainly determined by the contribution of electrons:

$$q_a \sim ne(1-z) \tag{2.9}$$

In this case the signal heavily depends on the interaction depth z. The spectroscopic performance of this detector will be particularly poor for high energy gamma rays since interactions will be spread over the whole detector depth. In the next section, we will see how this problem can be overcome using single polarity charge sensing.

2.1.4 Single Polarity Charge Sensing Readout

By using the technique of single polarity charge sensing, a uniform detector response can be achieved using only the contribution from the motion of electrons. An example of using this technique in gas detectors is the Frisch grid ion chamber[Fri.1], whose structure is shown in figure 2.3 (a). The whole detector volume is divided into two parts by the grounded Frisch grid electrode. During operation the cathode is negatively biased and the anode is positively biased. Electrons generated in the detector drift from the cathode to the grid, and then from the grid to the anode. Because of the electrical shielding effect of the grid, any charge between the cathode and the grid produces no induced charge at the anode. The electrons will induce charge at the anode only after they drift through the grid towards the anode. The weighting potential of the anode $\varphi(z)$ is shown in figure 2.3 (b)[Luk.1]. Assume n electron-ion pairs are generated by an energy deposition at depth z_0 between the cathode and grid. If all the electrons drift through the grid and are collected at the anode, the signal from the anode q_a is given by:

$$q_a = ne(\varphi(1) - \varphi(z_0)) = ne(1-0) = ne \tag{2.10}$$

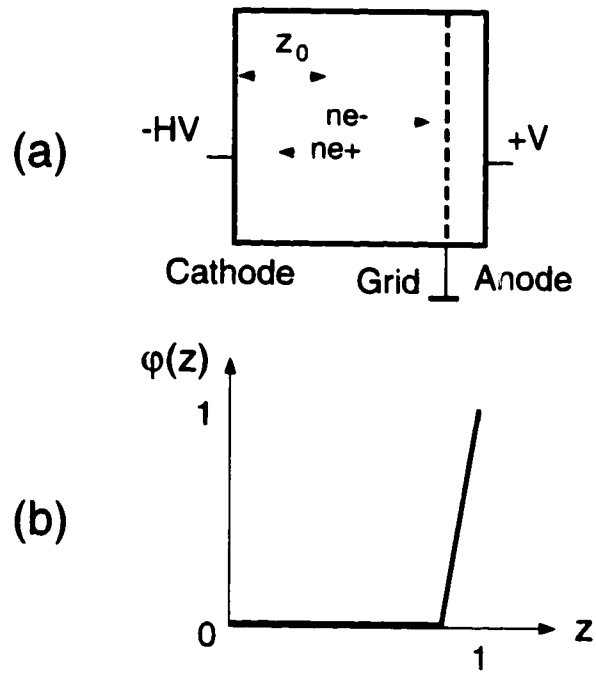

Figure 2.3: Frisch Grid Chamber: (a) Electrode configuration. (b) Weighting potential of the anode electrode.

Therefore the signal is independent of the interaction depth z_0 and proportional to n, the number of charge carriers generated. Most importantly, the signal is only dependent on the collection of the electrons. This single polarity charge sensing thus avoids the problem from the slow drift of the ions.

Techniques employing the same concept can be applied to room temperature semiconductor detectors by implementing special electrode geometries. One of the implementations, called the coplanar-grid detector, has an anode pattern illustrated in figure 2.4 (b). In contrast to a conventional planar anode, this anode consists of two groups of parallel strips. During operation, the two groups of strips are relatively biased by several tens of volts. The group with higher potential is the collecting electrode, the other is the non-collecting electrode. The weighting potential distributions of the two anode electrodes along a path underneath a collecting strip are shown in figure 2.4 (c)[Luk.1], as well as their difference. Because the distribution of the difference of the weighting potentials resembles that in figure 2.3 (b), this difference signal is used as a single polarity charge sensing readout. Except for events originating very near the anode, the difference signal is proportional to the number of electrons arriving the anode and independent of the motion of holes.

Another implementation of the single polarity charge sensing technique is the pixellated detector. For a detector with a pixellated anode (cf. figure 2.5 (b)), the weighting potential distribution from a single anode pixel is illustrated in figure 2.5 (c)[Bar.1]. The shape of this distribution is determined by the ratio of the pixel size to the detector depth. When the ratio is small ($\leq$0.1), the distribution is similar to those in figure 2.3 (b) and figure 2.4 (c), the desired weighting potential distributions for single polarity charge sensing. This is called the small pixel effect and produces a means to achieve single polarity charge sensing in pixellated detectors.

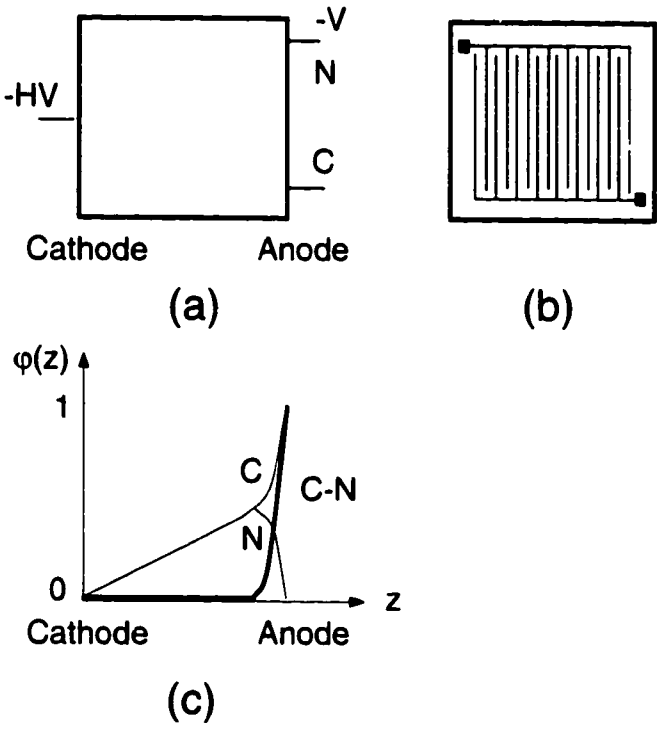

Figure 2.4: Coplanar-Grid Detector: (a) Electrode configuration. (b) Anode pattern. (c) Weighting potential of both anode electrodes and their difference.

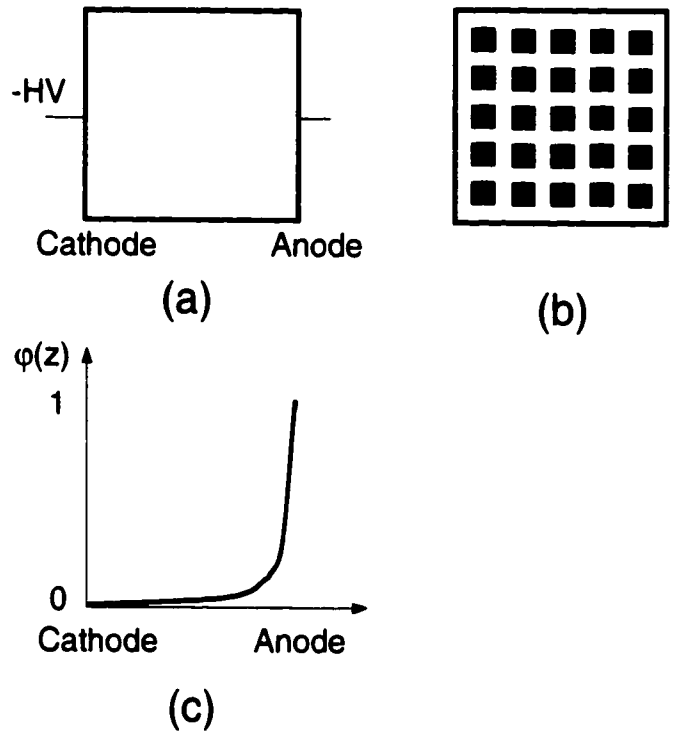

Figure 2.5: Pixellated Detector: (a) Electrode configuration. (b) Anode Pattern. (c) Weighting potential of a typical anode pixel electrode.

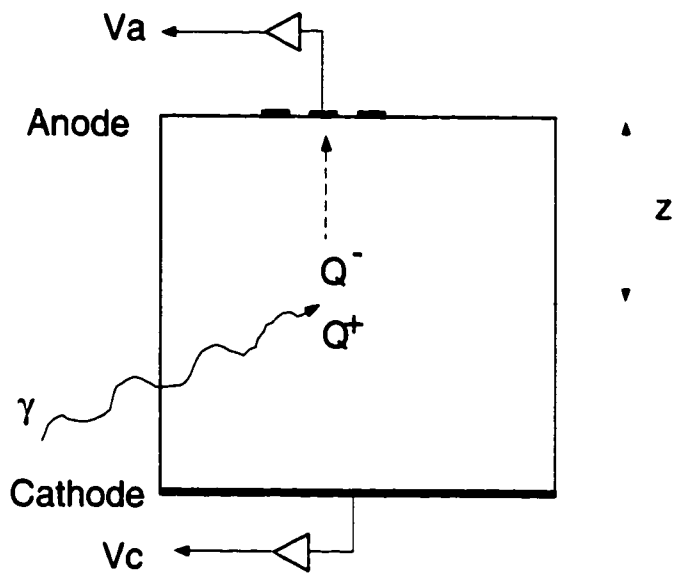

Figure 2.6: Interaction depth sensing by C/A ratio.

2.2 Interaction Depth Sensing

2.2.1 Depth Sensing by C/A Ratio

The technique of interaction depth sensing using a signal ratio can be applied to room temperature semiconductor detectors fabricated with a single polarity charge sensing anode and a conventional planar cathode, as illustrated in figure 2.6. For an energy deposition in the detector at arbitrary interaction depth z, the signals from both the anode V_a and the cathode V_c can be read out. Because of the single polarity charge sensing, V_a should be proportional to n, the number of electrons generated (assuming no electron trapping), or:

$$V_a = K_a n \tag{2.11}$$

where K_a is a constant. Because the cathode is a conventional planar electrode,

V_c should be proportional to the product of n and z (the interaction depth), so:

$$V_c = K_c n z \tag{2.12}$$

where K_c is a constant. In the ratio V_c/V_a, n is cancelled and only the information about z is left. This suggests that the C/A ratio, e.g., V_c/V_a, is proportional to the interaction depth z and independent of the deposited energy. In practice, the C/A ratio is not exactly proportional to z because of electron trapping and/or non-ideal single polarity charge sensing. However, in most cases, the C/A ratio still has a monotonic relationship with the interaction depth and can be used for interaction depth sensing. This technique is particularly useful in the coplanar designs discussed earlier.

2.2.2 Depth Sensing by Electron Drift Time

For multiple energy depositions in a 3-D pixellated CdZnTe detector from a single incident gamma ray, we expect to see signals from multiple pixels. For future reference, we shall refer to this as a multiple-pixel event. While the technique of interaction depth sensing by C/A ratio is effective on single-pixel events, it can not provide the interaction depths for multiple-pixel events. To explain this, consider a two-interaction event in the detector: a gamma ray first interacts by Compton scattering, and the scattered photon is captured elsewhere in the detector by a photoelectric interaction. The electrons generated by the two interactions are collected by two distinct pixels, as shown in figure 2.7. In order to accurately reconstruct the energy depositions from the two interactions, first we need to read out the pulse heights from the two pixels (V_{a1}, V_{a2}) correctly. Second, we want to know the two interaction depths (z_1, z_2). With this information, each individual pulse height could

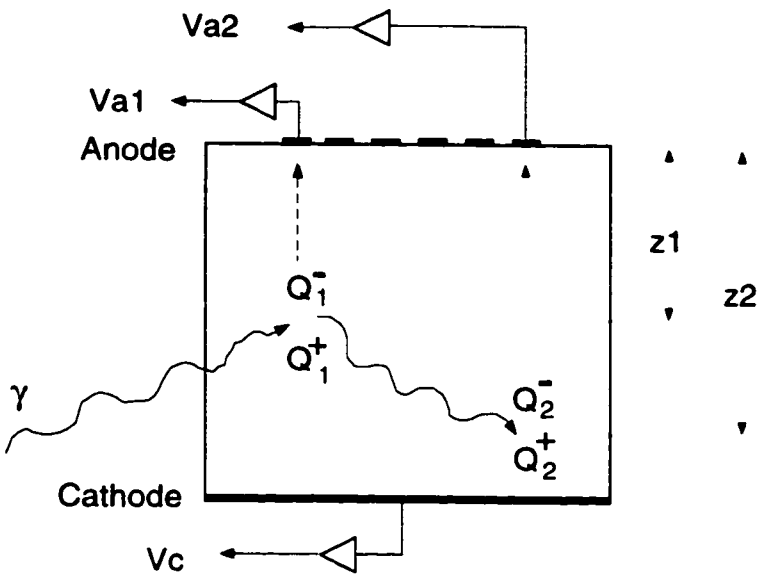

Figure 2.7: A Two-Interaction Event in the 3-D CdZnTe Detector. See the text for a description of symbols.

be corrected for electron trapping and material non-uniformity. However, with only the information about the signal pulse heights, it is impossible to derive each of the two interaction depths (z_1, z_2). Here the C/A ratio can only provide a weighted centroid of z_1 and z_2:

$$\frac{V_c}{V_{a1} + V_{a2}} = \frac{V_{a1} z_1 + V_{a2} z_2}{V_{a1} + V_{a2}} \tag{2.13}$$

Therefore more information than the signal pulse heights is needed to reconstruct the multiple-pixel events in 3-D CdZnTe detectors.

A solution to this problem is to read out the timing information associated with the cathode and anode pixel signals. For a two-interaction event which results in a two-pixel event from the detector, the signals (preamplifier outputs) from the cathode and the two anode pixels are illustrated in figure 2.8. The leading edge timing of the cathode signal t_c provides the time origin when the electrons start to drift towards the anode, and the leading edge timing of the anode pixel signals t_1, t_2 tell the

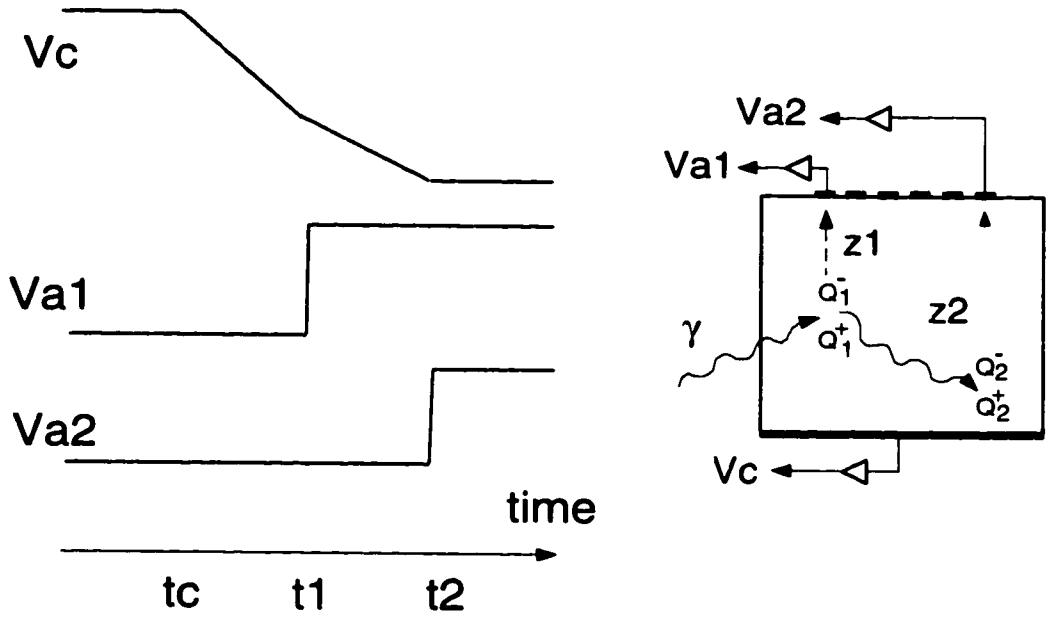

Figure 2.8: Reconstruction of multiple-pixel events.

electron arrival times at each individual pixel. Therefore the electron drift times for the two interactions t_{d1}, t_{d2} can be determined by reading out t_c, t_1 and t_2. For interaction events in 3-D CdZnTe detectors, the electron drift time and electron drift distance have a monotonic relationship which depends on the detector bias. With a calibration, the interaction depths z_1, z_2 can be determined from the measured t_{d1}, t_{d2} since z_1, z_2 can be considered as the electron drift distances corresponding to the two interactions.

As an alternative method to reconstruct z_1 and z_2, only the timing information from the two pixels t_1, t_2 need to be read out to determine z_2-z_1. The weighted centroid of z_1 and z_2 can be determined from the C/A ratio according to equation 2.13. Thus z_1, z_2 can be determined.

The first approach is simpler, and the concept of interaction depth sensing by electron drift time can be considered as a general approach applicable to both single-pixel and multiple-pixel events. For the 3-D CdZnTe detectors, because the dimension of

the anode pixels is small (~10% of the detector thickness), we can assume the electrical field in the detector is uniform and so the electron drift velocity is constant. This should be true in most of the detector volume except for a thin layer (< 10% of the detector thickness) near the anode. With this assumption, the electron drift time should be proportional to the electron drift distance. Therefore, if the maximum electron drift time is T, then z_1, z_2 (normalized to detector thickness) can be determined by:

$$\begin{cases} z_1 = t_{d1}/T = (t_1 - t_c)/T \\ z_2 = t_{d2}/T = (t_2 - t_c)/T \end{cases} \tag{2.14}$$

Because the leading edge timing readout of the cathode and anode pixel signals are independent, the uncertainties in the reconstructed z_1 and z_2 should be:

$$\begin{cases} (FWHM)^2_{z_1} = ((FWHM)^2_{t_1} + (FWHM)^2_{t_c})/T^2 \\ (FWHM)^2_{z_2} = ((FWHM)^2_{t_2} + (FWHM)^2_{t_c})/T^2 \end{cases} \tag{2.15}$$

Therefore the timing resolutions $(FWHM)_{t_c}$, $(FWHM)_{t_1}$, $(FWHM)_{t_2}$ from the cathode and anode pixel signals directly determine the accuracies of the reconstructed z_1 and z_2.

2.3 3-D Non-uniformity Correction

To correct for non-uniformity in the 3-D position sensitive CdZnTe detector, the detector is divided into $i \times j \times k$ voxels, where $i \times j$ is the number of anode pixels and k is the number of depth layers we choose to consider. Even if the

response from the detector were uniform, the measured signal amplitude will vary due to the difference in the gains of each individual electronic channel. Denote the relative electronic gain for pixel (i, j), which can be measured separately, as f^e_{ij}. The 3-D variation in the electron generation (e.g., due to nonuniform zinc concentration[TON.1]) and collection is given by f^d_{ijk}, which is the expected pulse height per unit energy deposition in detector voxel (i, j, k). With energy deposition E_{ijk} in voxel (i, j, k), the signal measured on pixel (i, j) should be:

$$V_{ij}(k) = f^e_{ij} \cdot f^d_{ijk} \cdot E_{ijk} = f_{ijk} \cdot E_{ijk} \tag{2.16}$$

where the overall variation of f_{ijk} is independent of the energy deposition. For mono-energetic gamma rays of energy E, f_{ijk} can be determined from the measured photopeak centroids for each voxel: $f_{ijk} = V^{centroid}_{ij}(k)/E$.

2.3.1 Calibration

The purpose of calibration is to measure the 3-D distribution of the photopeak centroids and thus determine the f_{ijk} needed for the non-uniformity correction. Since the values of f^d_{ijk} are influenced by electron trapping along the collection path, a calibration has to be performed for each cathode bias.

2.3.2 Spectrum Gain Adjustment for Discrete Channels

The overall gain adjustment $1/f_{ijk}$ needs to be applied to the pulse height spectrum from each voxel before these spectra can be combined. It is difficult to perform the gain adjustment before the A/D conversion. We also can not simply apply the adjustment factor to the A/D conversion result because of the distortions caused by the round-off error. Instead, the gain adjustment is performed by software in the following manner. Assuming the original spectrum is collected with an ADC

channel width of ΔV and the nonlinearities in the A/D conversion are negligible, the boundaries of the ith channel should be $V_{i-1} = (i-1) \cdot \Delta V$ and $V_i = i \cdot \Delta V$. Applying a gain correction G to the original spectrum is equivalent to changing the channel width to $\Delta V' = \Delta V/G$. The new spectrum has channel boundaries $V'_j = j \cdot \Delta V'$, and the count number in the new jth channel is calculated assuming the count density $(N_i/\Delta V)$ is constant in each original channel (cf. figure 2.9). If N_i and N'_j are the counts in channel i of the original spectrum and channel j in the new spectrum respectively, and the boundaries of the jth channel in the new spectrum satisfy $V_{i-2} < V'_{j-1} < V_{i-1} < V'_j < V_i$, then the count number N'_j can be calculated as:

$$\begin{aligned} N'_j &= N_{i-1}\frac{V_{i-1} - V'_{j-1}}{\Delta V} + N_i\frac{V'_j - V_{i-1}}{\Delta V} \\ &= N_{i-1}(i - 1 - \frac{j-1}{G}) + N_i(\frac{j}{G} - (i-1)) \end{aligned} \tag{2.17}$$

The mapped spectrum is only determined by the related channel numbers and the coefficient G. Figure 2.10 shows the result of a gain adjustment to a ^{137}Cs spectrum. The gain adjustment is applied to the original spectrum (A) to move the photopeak centroid to channel 1000 and yield spectrum (B). The effect of an identical gain adjustment on a rectangular distribution is also shown in figure 2.10. No obvious distortion is observed with this gain adjustment method and the total counts are preserved. In practice, we sample more than 8 channels within the FWHM of the photopeak to avoid any undersampled photopeak which may be artificially broadened by applying this gain adjustment technique.

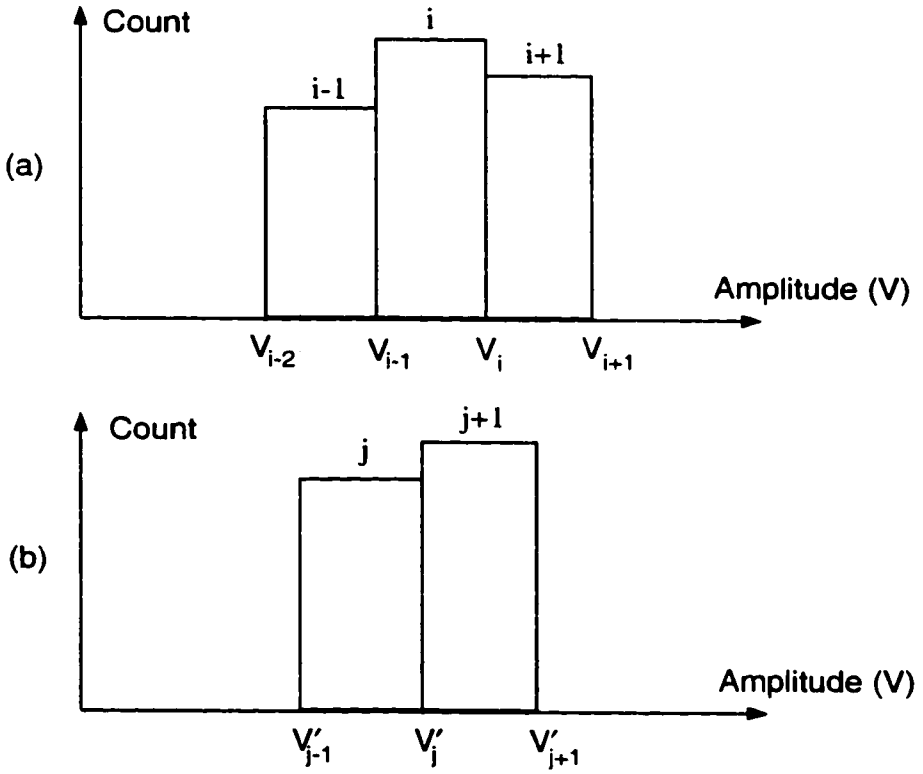

Figure 2.9: Calculation of the new count number of a channel in the gain adjustment. Shown are (a) the original spectrum, and (b) the corrected spectrum.

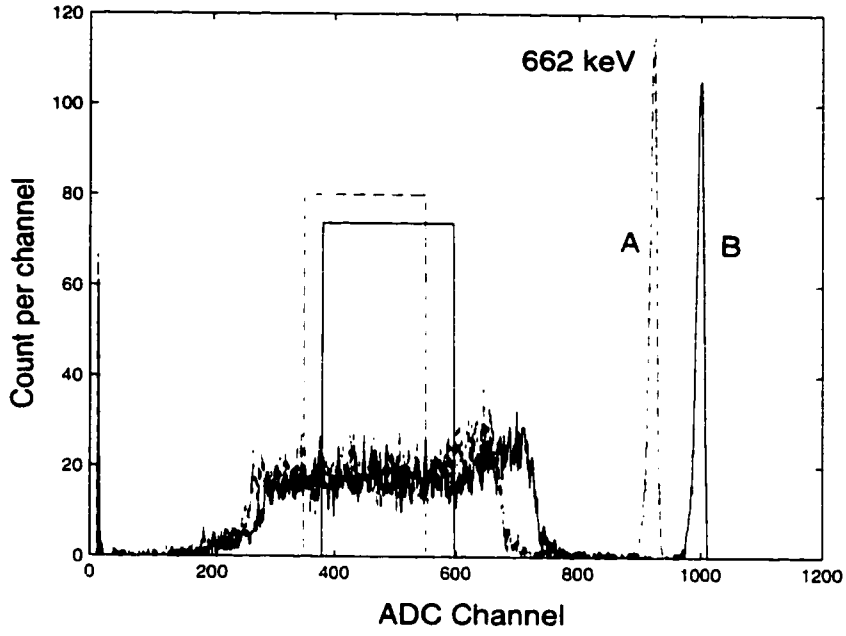

Figure 2.10: Result of gain adjustment to a ^{137}Cs spectrum. See text for a description of the method.

2.4 Determination of the Mobility and Lifetime of the Electrons

The electron mobility and lifetime determine the transport of electrons in the detector. In the investigation of the performance of the 3-D CdZnTe detectors, it is usually necessary to measure these two parameters.

2.4.1 Determination of μ_e

In a cubic 3-D CdZnTe detector, the electric field can be considered uniform except for the region very near the anode. Thus the mobility of electrons, μ_e, can be estimated from the maximum electron drift time, t_{max}:

$$\mu_e = v_e/E = (D/t_{max})(D/V) = D^2/(Vt_{max}) \tag{2.18}$$

where D is the detector thickness and V is the cathode bias. Since t_{max} can be

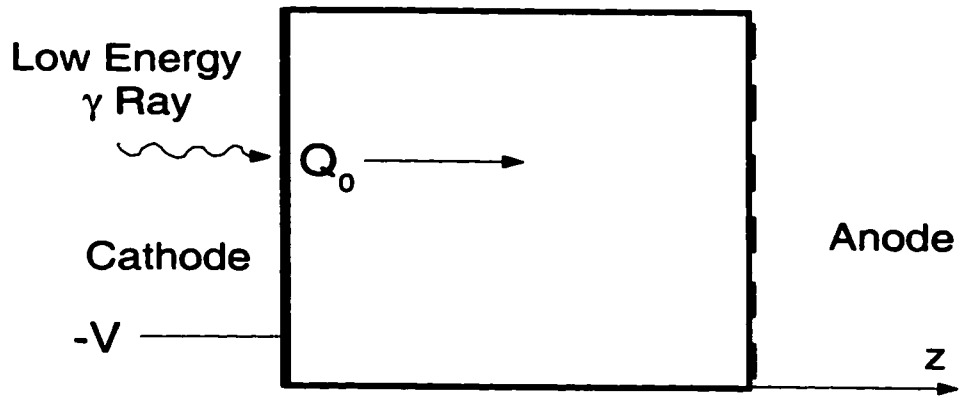

Figure 2.11: Determination of $(\mu\tau)_e$ Using Hecht Relation.

measured as the maximum rise time from the cathode preamplifier output, and D and V are known, μ_e is determined.

2.4.2 Determination of $(\mu\tau)_e$ Using the Hecht Relation

The mobility-lifetime product of electrons can be measured through the readout from a conventional planar electrode. A traditional way to do this measurement is to irradiate the cathode with low energy gamma rays, and measure the relationship between the photopeak centroid in the cathode spectrum and the detector bias. As illustrated in figure 2.11, most of the interactions should occur very near the cathode surface. Assume all the electrons with total electric charge of Q_0 are generated due to the energy deposition near the cathode. When the electrons drift through the detector a distance z, the electric charge should decrease to $Q(z)$ due to the electron trapping:

$$Q(z) = Q_0 e^{-\frac{zD}{(\mu\tau)_e V}} \tag{2.19}$$

where D is the detector thickness and V is the cathode bias. Thus the variation of the induced charge on the cathode dq, due to the displacement dz, of the charge

$Q(z)$, should be:

$$dq = Q(z)\frac{dz}{D} = Q_0 e^{-\frac{zD}{(\mu\tau)_e V}} \cdot \frac{dz}{D} \tag{2.20}$$

The total induced charge at the cathode, q_c, can then be calculated from the integration of dq:

$$q_c = \int_0^D Q_0 e^{-\frac{zD}{(\mu\tau)_e V}} \frac{dz}{D} = Q_0 \frac{(\mu\tau)_e V}{D^2}[1 - e^{-\frac{D^2}{(\mu\tau)_e \cdot V}}] \tag{2.21}$$

q_c is proportional to the pulse height from the cathode, so the photopeak centroid, H_c, in the cathode spectrum should be related to V and $(\mu\tau)_e$ using equation 2.21 as:

$$H_c = K(\mu\tau)_e V[1 - e^{-\frac{D^2}{(\mu\tau)_e V}}] \tag{2.22}$$

where K is a constant. Using equation 2.22, known as the Hecht relation[Hec.1], the variation of photopeak centroid H_c as a function of V can be predicted for different $(\mu\tau)_e$ values, and then compared to the measured result to find the true $(\mu\tau)_e$ for the detector material.

2.4.3 Determination of $(\mu\tau)_e$ Using Anode Signals

In the 3-D CdZnTe detectors, $(\mu\tau)_e$ can also be measured through the energy spectra from the anode pixels. In the experiment illustrated in figure 2.11, the photopeak centroids in the low energy gamma spectra from an anode pixel can be used to determine $(\mu\tau)_e$ with the assumption of the perfect small pixel effect. In this case, the photopeak centroid, H_a, from the anode pixel is proportional to the number of electrons arriving the pixel and should follow equation 2.19:

$$H_a = Ce^{-\frac{D^2}{(\mu\tau)_e \cdot V}} \tag{2.23}$$

where C is a constant. Compared with equation 2.22, the photopeak centroid has a simpler relationship with the detector bias V. The measured correlation between H_a and V can be fitted to get a more accurate value for $(\mu\tau)_e$.

Another alternative to measure the $(\mu\tau)_e$ is to use high energy gamma rays and collect the energy spectra from the anode pixels using interaction depth sensing. The photopeak centroid in the spectrum, H_a, should be related to the interaction depth z as (again, using equation 2.19):

$$H_a = C \cdot e^{-\frac{z \cdot D}{(\mu\tau)_e \cdot V}} \tag{2.24}$$

where C is a constant. Therefore the measured correlation between H_a and z can be fitted to yield $(\mu\tau)_e$.

The $(\mu\tau)_e$ measured using the signals from a specific anode pixel is associated with the CdZnTe material underneath that pixel. The results from different pixels may be different, and the variation implies material non-uniformity across the detector. We shall exploit this method for determining $(\mu\tau)_e$ in Chapter 6 and investigate the spatial variation of the results.

CHAPTER III

MODELING

3.1 Modeling the Energy Deposition

In order to understand the performance of the 3-D position sensitive CdZnTe detectors used as gamma-ray spectrometers, it is necessary to model the energy depositions in the detector due to the interactions with gamma rays. In the modeling, the detection efficiency for 662 keV gamma rays is estimated. The charge sharing among the adjacent pixels is investigated, as well as its impact on the fraction of the multiple-pixel events in the total interaction events from the detector.

3.1.1 EGS4 Modeling Tool

Among several fully-verified Monte Carlo simulation codes available from the high energy physics society, EGS4 is selected as the modeling tool for this work. EGS4 is designed and developed for the Monte Carlo simulation of the radiation transport of electrons and/or photons. The EGS4 code takes into account all the major physics processes involved in the interactions of electrons and photons. The simulation can be done in an arbitrary geometry for any element, compound, or mixture. The dynamic range of electron kinetic energies goes from a few tens of keV up to a few thousand GeV, and the dynamic range of photon energies lies between 1 keV and several thousand GeV[Nel.1].

The EGS4 applications are developed using the Mortran language[Coo.1]. The structure of a typical EGS4 simulation code is illustrated in figure 3.1. To develop an EGS4 simulation, the user must write a MAIN program which contains two subroutines: HOWFAR and AUSGAB. HOWFAR defines the geometry and AUSGAB defines the output information extracted. MAIN should also call two important subroutines included in the EGS4 system code: HATCH and SHOWER. The call to HATCH performs the initialization of the simulation. Each call to SHOWER generates one EGS history, and the parameters of the incident particle are passed to SHOWER by the arguments.

Before the executable generated by EGS4 can be run, the user must generate the media data using PEGS4. The user needs to prepare an input file for PEGS4 which specifies the media involved in the simulation. The PEGS4 will generate the necessary data about the cross sections and branching ratios accordingly and save the data into a file which can be read by the EGS4 code in the initialization of the simulation.

3.1.2 Modeling Setup

The simulation setup is illustrated in figure 3.2. The detector is a cubic 3-D CdZnTe detector of 1 cm thickness and with an 11×11 pixellated anode. The dimension of each pixel is 0.7×0.7 mm^2. In the simulation, the detector is irradiated from the cathode side by an uniform parallel beam of gamma rays. The detector volume is divided into 121 regions, each region corresponding to the column of CdZnTe material underneath each anode pixel. For each interaction with an incoming gamma ray, the total energy deposition in the detector and the energy depositions in each region are recorded.

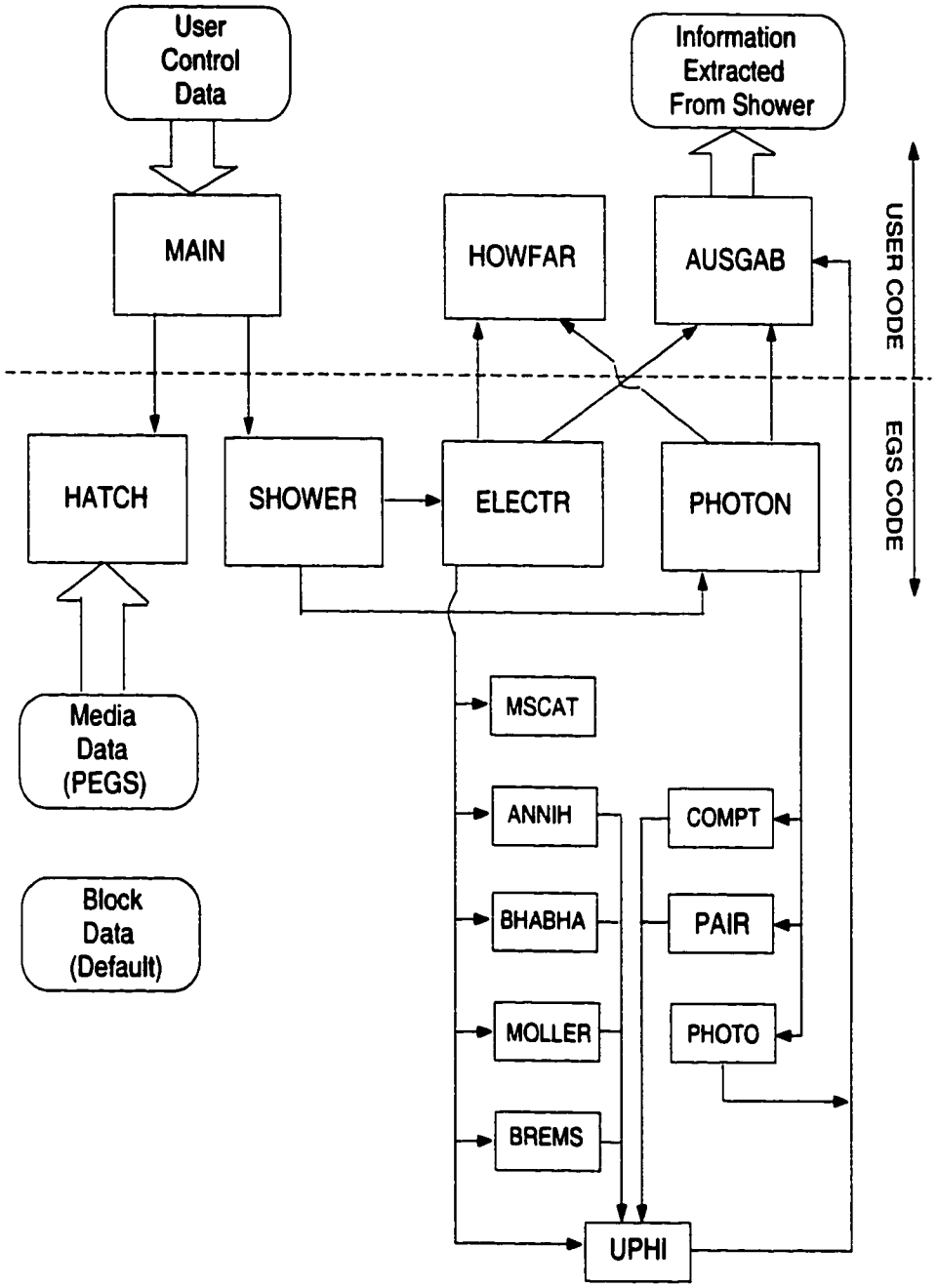

Figure 3.1: Typical structure of an EGS4 simulation code.

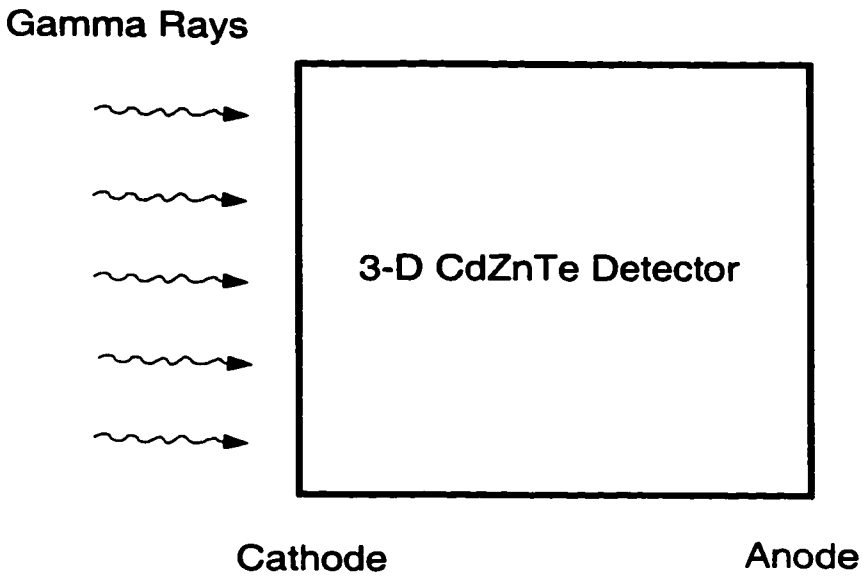

Figure 3.2: Simulation setup for 3-D CdZnTe detector.

3.1.3 Modeling Results and Discussions

Simulations using 662 keV incident gamma rays have been performed. Table 3.1 shows the results from events having total energy deposition in the detector. The results predict an intrinsic detection efficiency of ~35.5% and an intrinsic photopeak efficiency of ~8.1% for 662 keV gamma rays.

During the operation of a 3-D CdZnTe detector, the electrons generated by a single incident photon could be shared by multiple pixels due to multiple interactions, transport of K-shell X-rays, or non-negligible electron cloud size. In the first simulation, the electron cloud size is neglected by setting a high electron cutoff energy. The recorded fractions of multiple-pixel events with full 662 keV energy depositions are shown in figure 3.3 (a). Here the threshold, used to determine whether a pixel yields a signal, is set to 10 keV. The results show ~55% of the full energy deposition events are multiple-pixel events due to multiple interactions in the detector, and ~40% of the full energy deposition events are two-pixel events. For two-pixel events with full

Table 3.1: 662 keV simulation results from total energy deposition in the detector.

Name	*Number*	*Fraction of Total Incident Photons*
Incident Photons	5000000	100%
Interacted Photons	1778659	35.5%
Full Energy Depositions	405421	8.1%

energy deposition, the distribution of the distance (calculated from the coordinates of the two pixels, in the unit of pixel size) between the two pixels is recorded and shown in figure 3.3 (b). For the two-adjacent-pixel events, the energy spectrum recorded from one of the two pixels is shown in figure 3.3 (c). For those events with distance of 2, meaning the two pixels are separated by another pixel, the energy spectrum recorded from one of the two pixels is shown in figure 3.3 (d). Figure 3.3 (a) shows that ~90% of the 662 keV full energy deposition events involve only 1 or 2 interactions. Figure 3.3 (b) shows that most two-pixel events involve neighboring pixels. In addition, from the prominent backscattering peak in the energy spectra in figure 3.3 (c) and (d), a significant feature of the two-pixel full energy deposition events, it is shown that the first interaction is a back-scattering interaction yielding an energy deposition of ~0.48 MeV. The other pixel sees the relatively low energy (~200 keV) backscattered photon, which can be easily captured in the detector.

In practice, the electron cloud size can not be neglected because of the small pixel size we choose to consider. When the electron cloud arrives at the anode, its size is determined by two factors: the original cloud size and the expansion due to the electron diffusion. The original electron cloud size can be simulated by lowering the

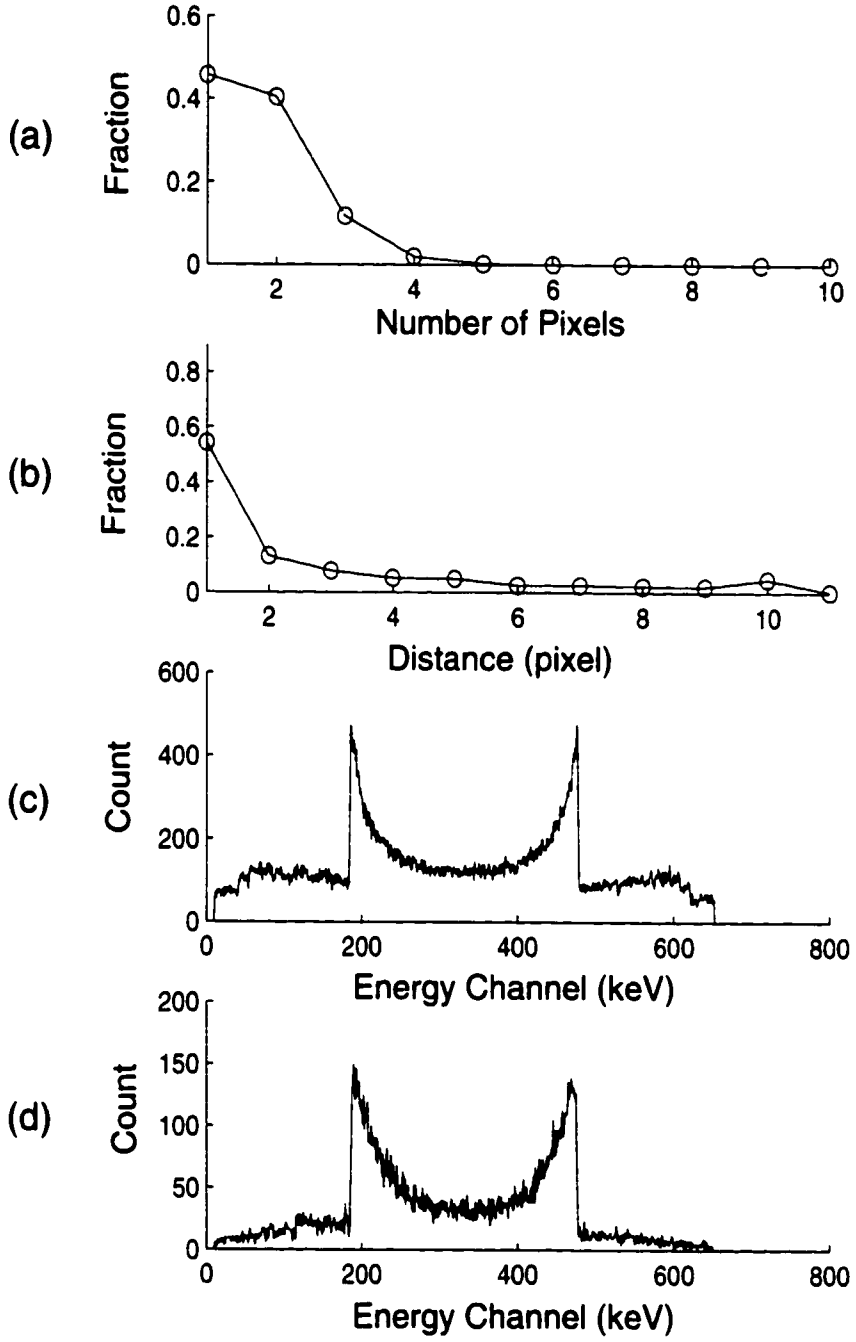

Figure 3.3: Simulation results from 662 keV full energy deposition events, not considering the electron cloud size. (a) Fraction of total events as a function of the number of pixels yielding signals. (b) For two-pixel events: the distribution of the distance between the two pixels. (c) The energy spectrum from one pixel in two-adjacent-pixel events. (d) The energy spectrum from one pixel in two-pixel events with distance of two pixels.

electron cutoff energy to ~10 keV, thereby extending tracking over larger distances. The electron cloud expansion due to diffusion can be included in the simulation using the theory of electric charge drift and diffusion. In a semiconductor material, the continuity equation for electrons is given by[Jer.1]:

$$\nabla(e(D\nabla n - \mu n E)) = 0 \tag{3.1}$$

where n is the electron density, μ is the electron mobility, and E is the electric field. D is the diffusion coefficient which is related to μ as:

$$D = \frac{KT}{e}\mu, \tag{3.2}$$

where T is the absolute temperature, and e is the unit charge. For electrons in CdZnTe, a typical value of D is 26 cm^2/s[Pre.1]. The solution of the electron density n(r,t) in equation 3.1 is a radially symmetric distribution[Pre.1]:

$$n(r,t) = \frac{exp(-t/\tau)}{\sqrt{(2\pi tD)^3}} exp(-\frac{r^2}{4tD}) \tag{3.3}$$

Identifying the spatial component as a Gaussian distribution with $2\sigma^2$ as $4tD$, the FWHM of the electron density can be determined from equation 3.3 as:

$$(FWHM)_n(r,t) = 2.355\sqrt{2tD} = 2.355\sqrt{2zdD/(\mu V)} \tag{3.4}$$

where $t = z/v = (zd)/(\mu V)$ and z is the depth of the origin of the electron cloud, d is the detector thickness, and V is the cathode bias applied to the detector. Thus the expansion of the electron cloud due to the diffusion of the electrons can be estimated from z, which is available in the simulation. In practice, for each energy deposition smaller than 10 keV (the electron cutoff energy), the electron cloud arriving the anode is approximated as a ball with radius $(FWHM)_n(r,t)$ and a uniform electron density. Once the size and location of the electron cloud is determined, the electron sharing over different anode pixels can then be calculated from the boundaries of the involved pixels.

Including the electron cloud size, the simulation results for 662 keV full energy deposition events in a 3-D CdZnTe detector under the cathode bias of -2000 V are shown in figure 3.4. By comparing figure 3.3 (a) to figure 3.4 (a), we note the fraction of single-pixel 662 keV full energy deposition events drops from ~45% to ~27% due to the sharing of the electron cloud among the adjacent pixels. By comparing the number of counts shown in figure 3.3 (c) to figure 3.4 (c), we can clearly see the impact of electron cloud sharing on the spectrum from one pixel of the two-adjacent-pixel events with full energy deposition. By comparing the number of counts shown in figure 3.3 (d) to figure 3.4 (d), we also note the decrease of the number of those two-pixels events in which the two pixels are separated by another pixel, due to electron cloud sharing.

Among the 662 keV full energy deposition events, the fraction of the single-pixel events is small (~27%) for the 3-D CdZnTe detectors simulated. In case the 3-D CdZnTe detectors are used as gamma-ray spectrometers, the photopeak efficiency loss due to charge sharing will be significant for the energy spectrum from the single-pixel events. This situation can be improved if the energy spectrum from the multiple-

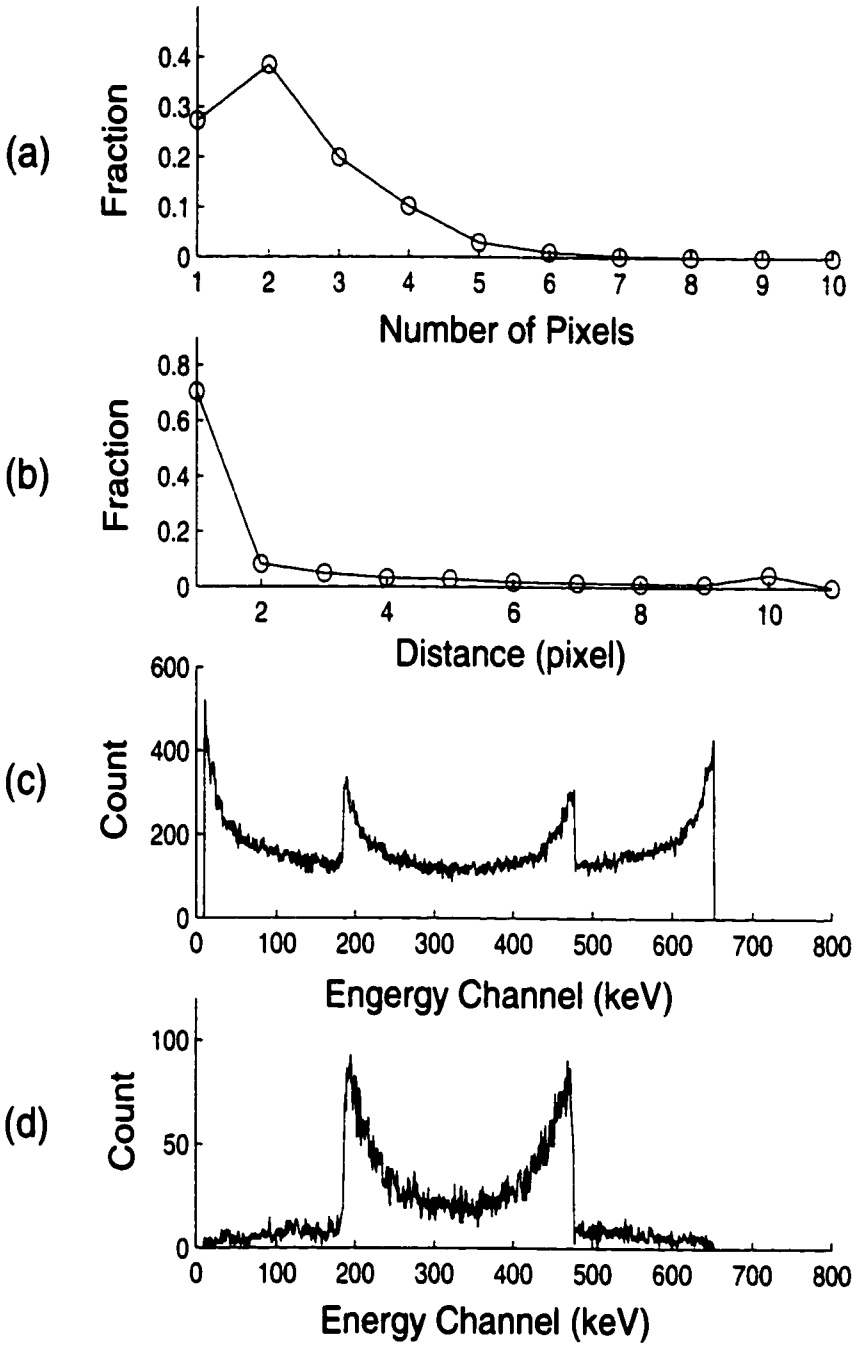

Figure 3.4: Simulation results from 662 keV full energy deposition events, considering the electron cloud size with a cathode bias of -2000 V. (a) Fraction in the total events as a function of the number of pixels yielding signals. (b) For two-pixel events: the distribution of the distance between the two pixels. (c) The energy spectrum from one pixel in two-adjacent-pixel events. (d) The energy spectrum from one pixel in two-pixel events with distance of two pixels.

pixel events can be reconstructed. The energy spectrum from the multiple-pixel events intrinsically has worse energy resolution than the spectrum from single-pixel events, because the equivalent electronic noise in the signal reconstructed from a multiple-pixel event should be the quadrature sum of the noises from all the involved pixels. Therefore there is a tradeoff between the photopeak efficiency and the energy resolution for 3-D CdZnTe gamma-ray spectrometers, especially when the electronic noise has a significant influence on the energy resolution. On the other hand, the fraction of the single-pixel events can be increased by using larger pixel dimensions. Figure 3.5 shows the simulation results for the fraction of the multiple-pixel 662 keV full energy deposition events using three other pixel dimensions: 1×1, 1.2×1.2, 1.8×1.8 mm^2. In the simulations, the anode pixel array is still 11×11. Therefore each different pixel size indicates a different detector size. The results in figure 3.5 show that the fraction of the single-pixel 662 keV full energy deposition events increases only from ~27% to ~37% when the pixel size is increased drastically from 0.7×0.7 mm^2 to 1.8×1.8 mm^2. This result confirms the importance of the reconstruction of the energy spectrum from the multiple-pixel events.

In the reconstruction of the total energy deposition of the multiple-pixel events, accurate reconstruction of the multiple interaction depths is critical for the electron trapping correction. For 662 keV two-pixel full energy deposition events from a 3-D detector with pixel size of 1.2×1.2 mm^2, figure 3.6 shows the distribution of the difference of the two interaction depths. In Chapter 6, this distribution will be compared with the measurement result from a 3-D CdZnTe detector in the reconstruction of the two-pixel events as a simple verification of the interaction depth sensing method.

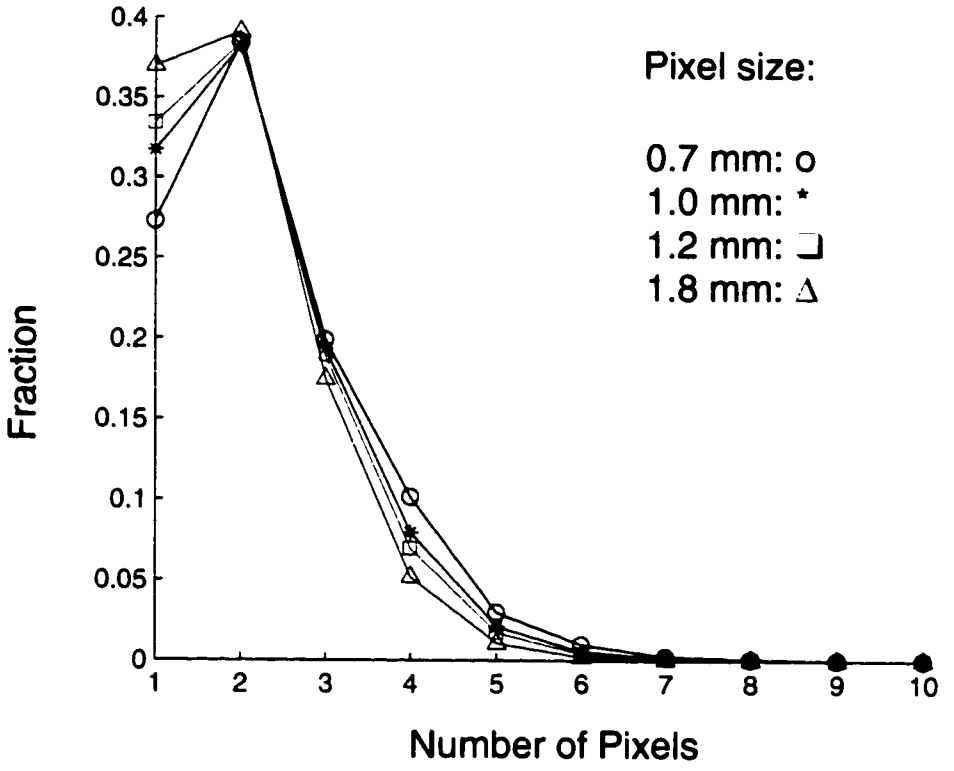

Figure 3.5: Fractions of multiple-pixel 662 keV full energy deposition events with different pixel sizes.

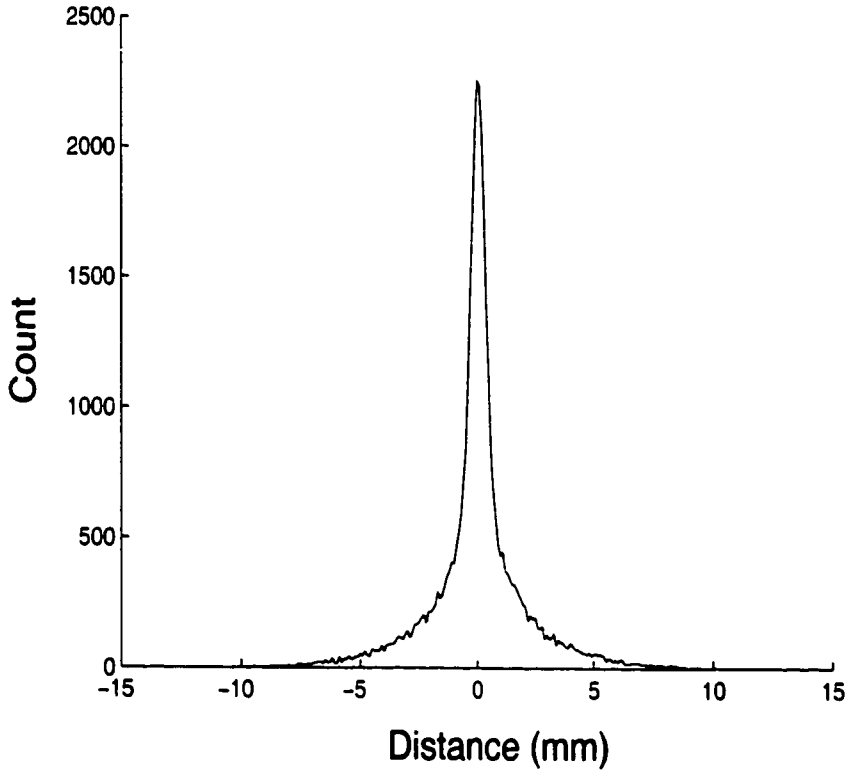

Figure 3.6: Distribution of depth separation of simulated 662 keV two-pixel full energy deposition events with pixel size of 1.2×1.2 mm^2.

3.2 Modeling the Signals from the Cathode and Anode Pixel

The 3-D CdZnTe detectors are fabricated with pixellated anodes and conventional planar cathodes. During the operation of a 3-D CdZnTe detector, each signal from the cathode and anode pixels is read out by a charge sensitive preamplifier, a shaping amplifier and the pulse height analyzer. To model the signal pulse heights from the cathode and anode pixels, we first model the signal current from the electrode due to the charge transport in the detector, and then model the signal processing through the preamplifier and shaping amplifier.

The modeling is based on a cubic 3-D CdZnTe detector with a thickness of 1 cm and an 11×11 pixellated anode. The dimension of each anode pixel is assumed to be 0.7×0.7 mm^2. Consider the situation presented in figure 3.7. Assume that at time $t = 0$ an electric charge Q_0 is located at depth z_0 in the detector and drifts towards the cathode due to an electric field. By time $t = T$ the charge is at depth z but has decreased to Q because of charge trapping. On an electrode whose weighting potential distribution is $\varphi(z)$ as a function of the detector depth, at time $t = T$ the signal current induced by the charge's motion is determined according to equation 2.7:

$$i(z(t)) = Q(z)\mu(V/d)d\varphi(z)/dz \tag{3.5}$$

where μ is the mobility of Q, V is the detector bias, and d is the detector thickness. Equation 3.5 assumes a uniform electric field inside the detector. Including the charge trapping associated with the mobility-lifetime product $\mu\tau$, we have (ignoring charge detrapping):

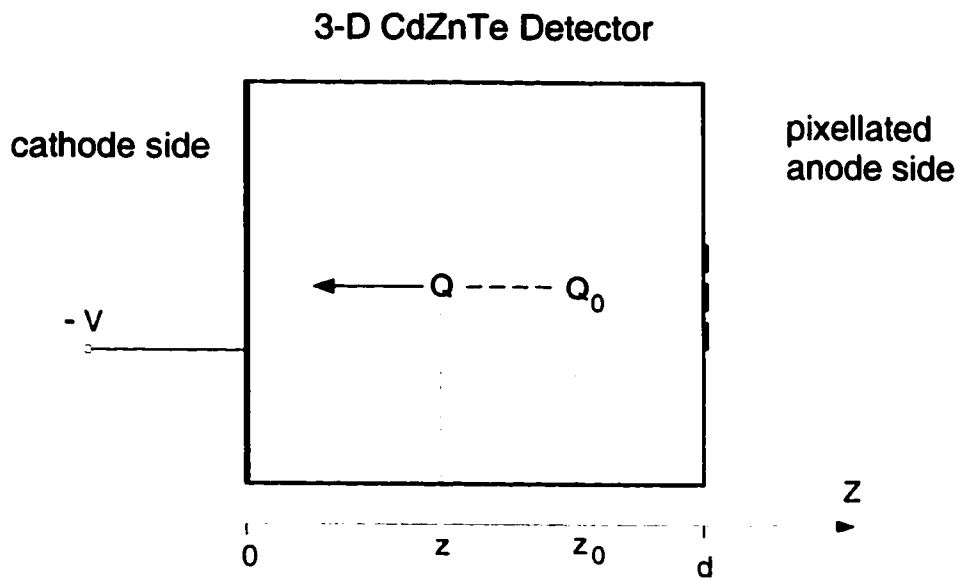

Figure 3.7: Signal generation in 3-D CZT detector.

$$i(z(t)) = \frac{Q_0 \mu V}{d} \frac{d\varphi(z)}{dz} e^{-\frac{|z_0 - z|d}{\mu \tau V}} \tag{3.6}$$

with

$$z(t) = z_0 - \frac{\mu V}{d} t \tag{3.7}$$

For a gamma interaction event in the detector, the signal currents induced by the motion of electrons and holes can be calculated separately using equation 3.6-3.7. The overall signal current on an electrode is the sum of the contributions from the electrons and the holes.

As an example of the modeling for a 3-D CdZnTe detector with detector thickness of 1 cm and pixel dimension of 0.7×0.7 mm^2, the weighting potential distribution for an anode pixel along the path parallel to the detector depth and through the center

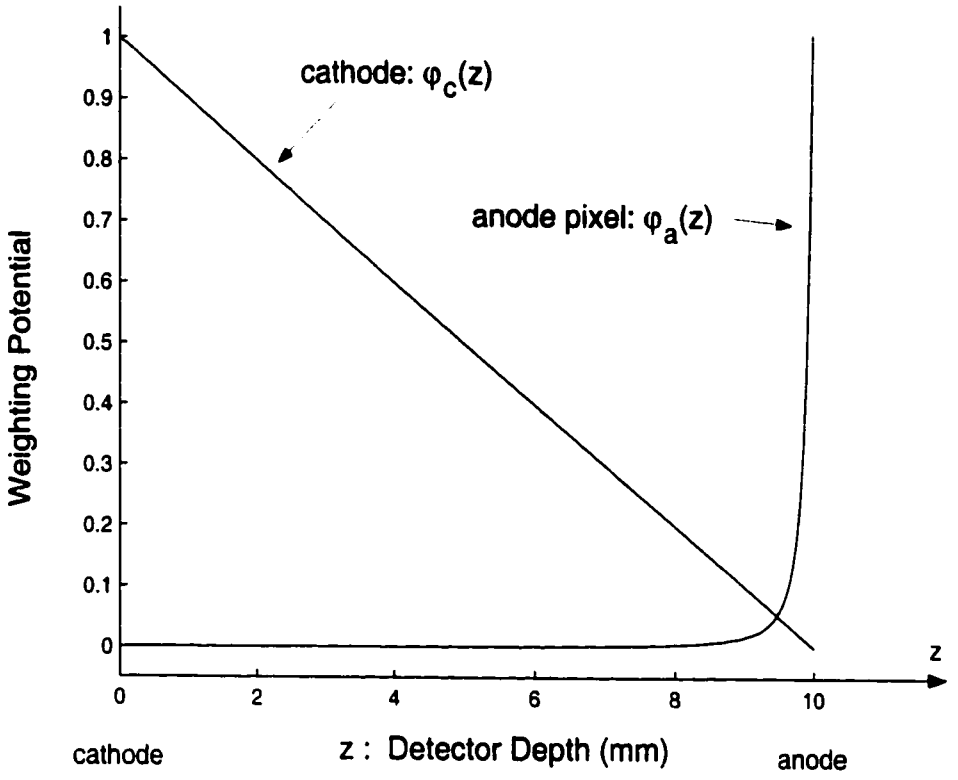

Figure 3.8: Weighting potentials between centers of the cathode and anode pixel in 3-D CdZnTe detector.

of this pixel is shown in figure 3.8 as $\varphi_a(z)$ (calculated using COULOMB[COU.1]), along with the weighting potential for the cathode $\varphi_c(z)$.

The charge-sensitive preamplifier and the shaping amplifier can be considered as an integrated signal processing system. The input of this system is the signal current from the detector and the output is the voltage signal from the output of the shaping amplifier. The width of the impulse response function $H(t)$ of this system is determined by the shaping time of the shaping amplifier. If the signal current is constant or the duration of the signal current is much narrower than the width of $H(t)$, the normalized output pulse height of this system is simply proportional to the integration of the signal current (the total charge collected). Otherwise, ballistic deficit should be taken into account to get an accurate normalized output pulse

height[Kno.1]. In the 3-D CdZnTe detector, the duration of the signal current from the cathode depends on the interaction depth, and the average duration time is comparable to the width of $H(t)$. Therefore the signal processing hardware should be considered in the modeling. In practice, $H(t)$ is approximated by a Gaussian shape $H(t) = H_0 \cdot e^{-(t-t_0)^2/(2\cdot\tau_s^2)}$ where τ_s is the shaping time of the amplifier. With known $H(t)$ and the signal current $i(t)$ from the detector, the cathode output signal $V(t)$ can be calculated as their convolution:

$$V(t) = \int_{-\infty}^{\infty} i(t')H(t-t')dt' \tag{3.8}$$

3.3 Modeling of Interaction Depth Sensing

Interaction depth sensing is the core of the 3-D position sensing technology used in the 3-D CdZnTe detectors. This section introduces the modeling of the two interaction depth sensing techniques involved in this work: depth sensing by C/A ratio and by electron drift time.

3.3.1 Modeling of Depth Sensing by C/A Ratio

To investigate interaction depth sensing by the C/A ratio, we need to model the pulse heights of signals from cathode and anode pixels as a function of the interaction depth. We choose $(\mu\tau)_e$ and $(\mu\tau)_h$ of 6×10^{-3} and 5×10^{-5} cm^2/V respectively and assume a uniform electric field inside the detector with a given cathode bias. For each signal from the cathode or the anode pixels, the normalized pulse height as a function of the interaction depth can be calculated using equation 3.8. The results calculated with the typical cathode bias of -2000 V are shown in figure 3.9 (a). The

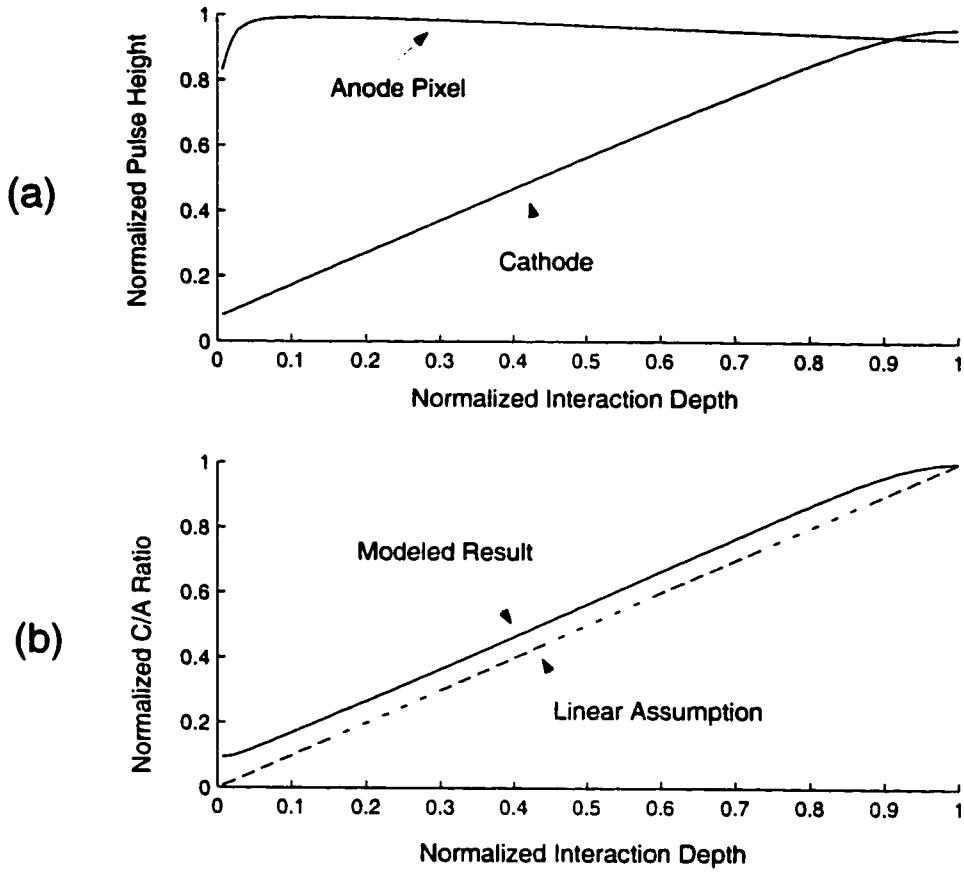

Figure 3.9: (a) Modeled pulse heights of signals from cathode and anode pixels as a function of interaction depth. (b) Calculated relationship between C/A ratio and interaction depth.

calculated relationship between the C/A ratio and the interaction depth is shown in figure 3.9 (b). Note that assuming the C/A ratio is the normalized depth (the dashed curve) will produce an 8% systematic error over most of the interaction depths. In the experiments with the 3-D CdZnTe detector under the same cathode bias, the calculated relation in figure 3.9 (b) can be used to calibrate the measured C/A ratio to the true interaction depth for the single-pixel events in the detector. This calibration relies on the pixel-based values of $(\mu\tau)_e$ and $(\mu\tau)_h$, which may vary from pixel to pixel. Different calibration curves may be applied to different pixels if there is a significant lateral variation of $(\mu\tau)_e$ and $(\mu\tau)_h$.

From the result in figure 3.9 (b), fluctuations in the signals from the cathode and anode pixel will lead to a predictable depth resolution of depth sensing by the C/A ratio. Assuming the relative FWHM of the cathode and anode pixel signals are η_c and η_a respectively, then the FWHM of the C/A ratio, $(FWHM)_R$, should be:

$$(FWHM)_R = \sqrt{\eta_c^2 + \eta_a^2} \cdot R \tag{3.9}$$

where R is defined as the C/A ratio. The depth resolution $(FWHM)_z$ can then be determined from $(FWHM)_R$ and $\Delta R/\Delta z$, the first-order derivative of the calibration curve in figure 3.9 (b), as:

$$(FWHM)_z = \frac{(FWHM)_R}{\Delta R/\Delta z} \tag{3.10}$$

As an example, if the fluctuations in the cathode and anode pixel signals are 12 keV and 9 keV in FWHM respectively, for 662 keV single-interaction events, $(FWHM)_R$ as a function of the interaction depth is shown in figure 3.10 (a). $\Delta R/\Delta z$ as a function of the interaction depth is shown in figure 3.10 (b). Thus the depth resolution, $(FWHM)_z$, can then be estimated following equation 3.10, and is shown in figure 3.10 (c). According to the result, the depth resolution (FWHM) of $2 \sim 3\%$ of the detector thickness can be achieved at most of the interaction depths, except in the region very near the cathode and the anode. The degradation of the depth resolution at the cathode side is due to the unusual change of the cathode signal in that region (as shown in figure 3.9 (a)), which makes the C/A ratio less sensitive to the change of the interaction depth. The degradation of the depth resolution at

the anode side is due to the significant change of the anode pixel signal along the interaction depth in that region, which is associated with the significant change of the weighting potential of the anode pixel.

3.3.2 Modeling of Depth Sensing by Electron Drift Time

As demonstrated in equation 2.15, the depth resolution of depth sensing by electron drift time should be determined by the resolutions of the leading edge timing readout of the cathode and anode pixel signals. Usually a simple leading edge timing readout circuit consists of a shaper and a discriminator, as shown in figure 3.11 (a). The shaper receives the pulse from the preamplifier as its input. When the output from the shaper exceeds a preset threshold, the discriminator generates a digital pulse with the desired timing information. In most cases, the time jitter Δt in the output of the discriminator is mainly caused by the random noise ΔV in the signal from the shaper, as illustrated in figure 3.11 (b). Usually ΔV is small compared with the signal amplitude, so Δt can be estimated as:

$$\Delta t = \Delta V/(dV/dt)|_{t=t_d} \tag{3.11}$$

dV/dt is the slope of the output signal from the shaper when the signal crosses the threshold of the discriminator. Given the transfer function and the input pulse waveform of the shaper, the output pulse waveform in the time domain can be simulated using the Simulink toolbox in Matlab[MAT.1]. In the simulation, dV/dt and ΔV are determined separately by using the signal and the random noise from the preamplifier as the input. By this means, Δt can be estimated if the signal and noise from the preamplifier are provided. To simplify the calculations involved, the

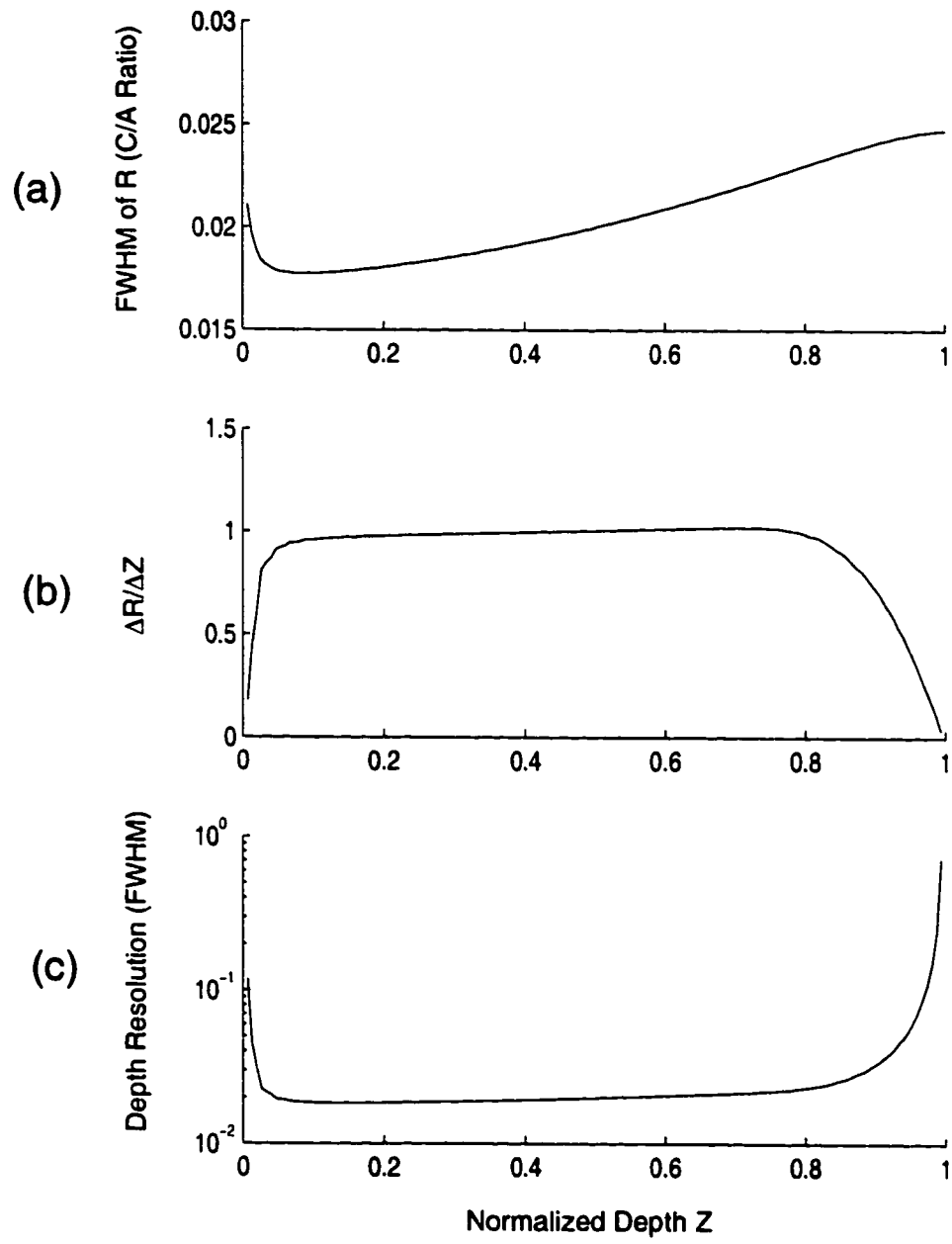

Figure 3.10: (a) The FWHM of the C/A ratio. (b) The first-order derivative of the calibration curve in figure 3.9 (b). (c) The modeled depth resolution of depth sensing by C/A ratio.

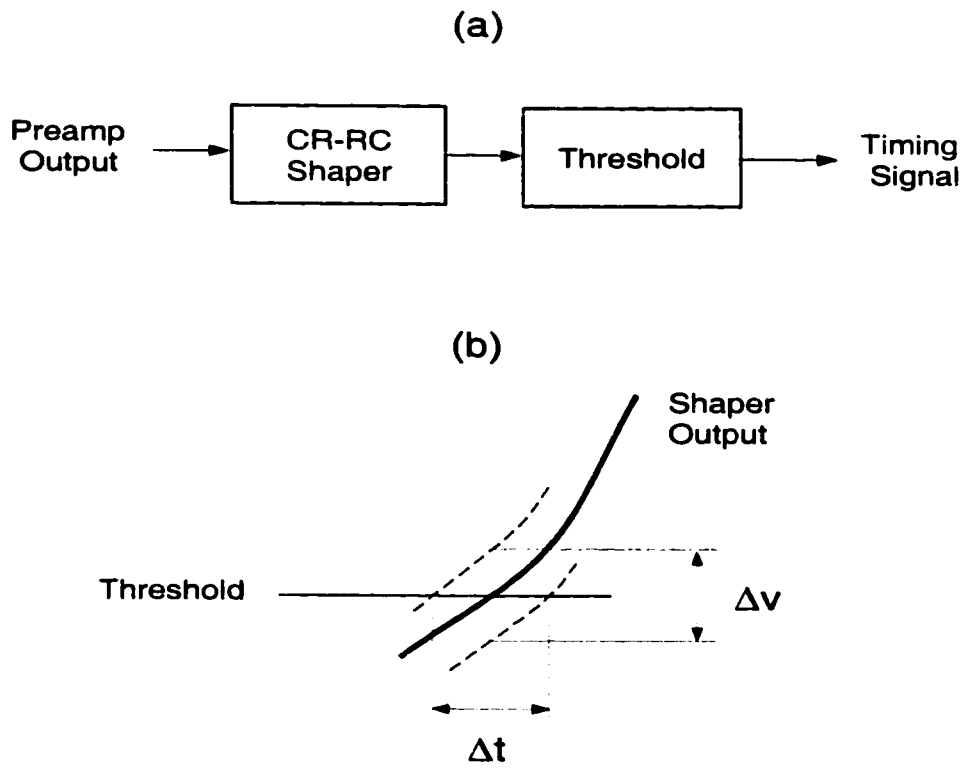

Figure 3.11: The readout of the leading edge timing.

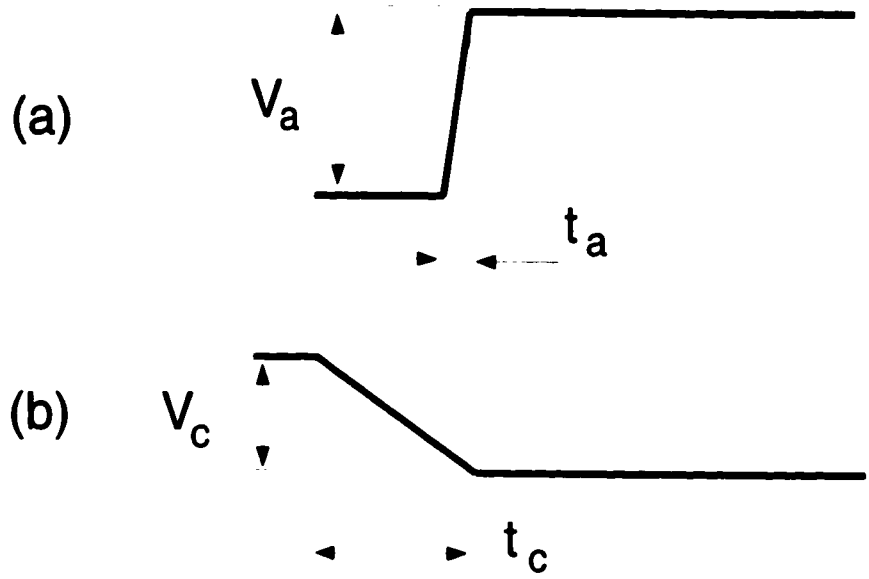

Figure 3.12: Simplification of the preamp outputs. (a) anode pixel. (b) cathode.

simulation is based on the following assumptions:

1. The electric field in the detector is uniform. All the electrons can be collected, and none of the holes move. Along the path perpendicular to the anode plane and underneath an anode pixel, the weighting potential of the anode pixel increases linearly from zero to one in the layer of one tenth of the detector thickness underneath the anode. For a single-site interaction event with n electron-hole pairs generated at normalized interaction depth $z > 0.1$, the preamplifier outputs simplified with the above assumptions are shown in figure 3.12. The pulse amplitudes (V_a, V_c) and rise times (t_a, t_c) of the signals from the cathode and anode pixels are determined (using the maximum electron drift time T and the preamplifier gain G) as:

$$\begin{cases} V_a = Gne \\ t_a = 0.1T \\ V_c = Gnez \\ t_c = zT \end{cases} \tag{3.12}$$

2. The noise at the preamplifier output is white noise.

3. The shaper is a CR-RC shaper with equal differential and integration time constant τ (shaping time). Therefore the transfer function of the shaper, $H(s)$, with unit gain is:

$$H(s) = \frac{s \cdot 1/\tau}{(s + 1/\tau)^2} \tag{3.13}$$

A simulation was performed on a 3-D CdZnTe detector of one centimeter thickness under the cathode bias of -1000 V. With the normal electron mobility of 1000 $cm^2/V{\cdot}s$, the maximum electron drift time T should be 1 μs according to equation 2.18. Figure 3.13 (a) shows the simplified output of a preamplifier connected to an anode pixel, figure 3.13 (b) shows the simulated output of the corresponding shaper which has a shaping time of 0.5 μs. The time delay from the starting time of the shaper output to the time when the shaper output cross the threshold is denoted as t_d, which can be determined for each shaper output with a given threshold. The fluctuation in t_d due to a given noise level can be estimated by equation 3.11, and indicates the achievable timing resolution. In the simulation, the noise levels from the cathode and anode pixel are adjusted to resemble the situation in the first gener-

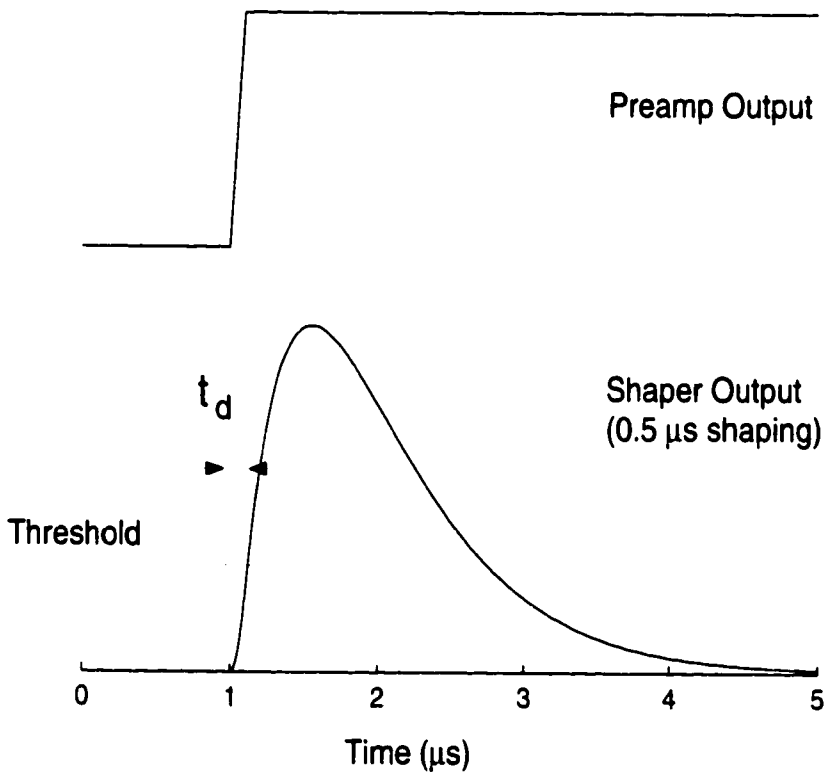

Figure 3.13: Pulse waveforms assumed in the simulation. (a) Preamplifier output. (b) Shaper output calculated using Simulink[MAT.1].

ation 3-D CdZnTe detectors: ~6 keV in FWHM from the anode pixel, and ~8 keV in FWHM from the cathode after 1 μs shaping.

The simulation results for the signals from the anode pixels are shown in figure 3.14. For a 662 keV energy deposition event at an interaction depth $z > 0.1$, figure 3.14 (a) shows the simulated timing resolutions with different shaping times and thresholds. The best timing resolution of ~1 ns (standard deviation) can be achieved with a shaping time of 0.2 μs and the energy threshold of ~330 keV. However, the energy threshold should be set much lower in the practice, so the timing information can be determined for the events with comparatively small energy depositions. With the energy threshold set to ~40 keV, the simulated timing resolutions with different shaping times and energy depositions are shown in figure 3.14 (b). When the energy deposition is above 200 keV, different shaping times do not make much difference in the timing resolutions. However, when the energy deposition is smaller than 100 keV, the timing resolutions from the larger shaping times (1 μs, 2μs) degrade much more rapidly with decreasing energy deposition than the timing resolutions from the smaller shaping times (0.1 μs, 0.2μs). Therefore, shorter shaping times should be used in the leading edge timing readout of the signals from the anode pixels. Figure 3.14 (c) shows the variation of t_d associated with different energy depositions and shaping times. The variation in t_d associated with different energy depositions (e.g., amplitude walk) could introduce a systematic error in the measurement of the electron drift time, so the smaller variations in t_d from the smaller shaping times are preferred. In practice, this systematic error can be corrected according to the signal pulse heights from the anode pixels.

The situation in the leading edge timing readout of the cathode signal is more complicated. The pulse waveform of the cathode signal is determined by not only

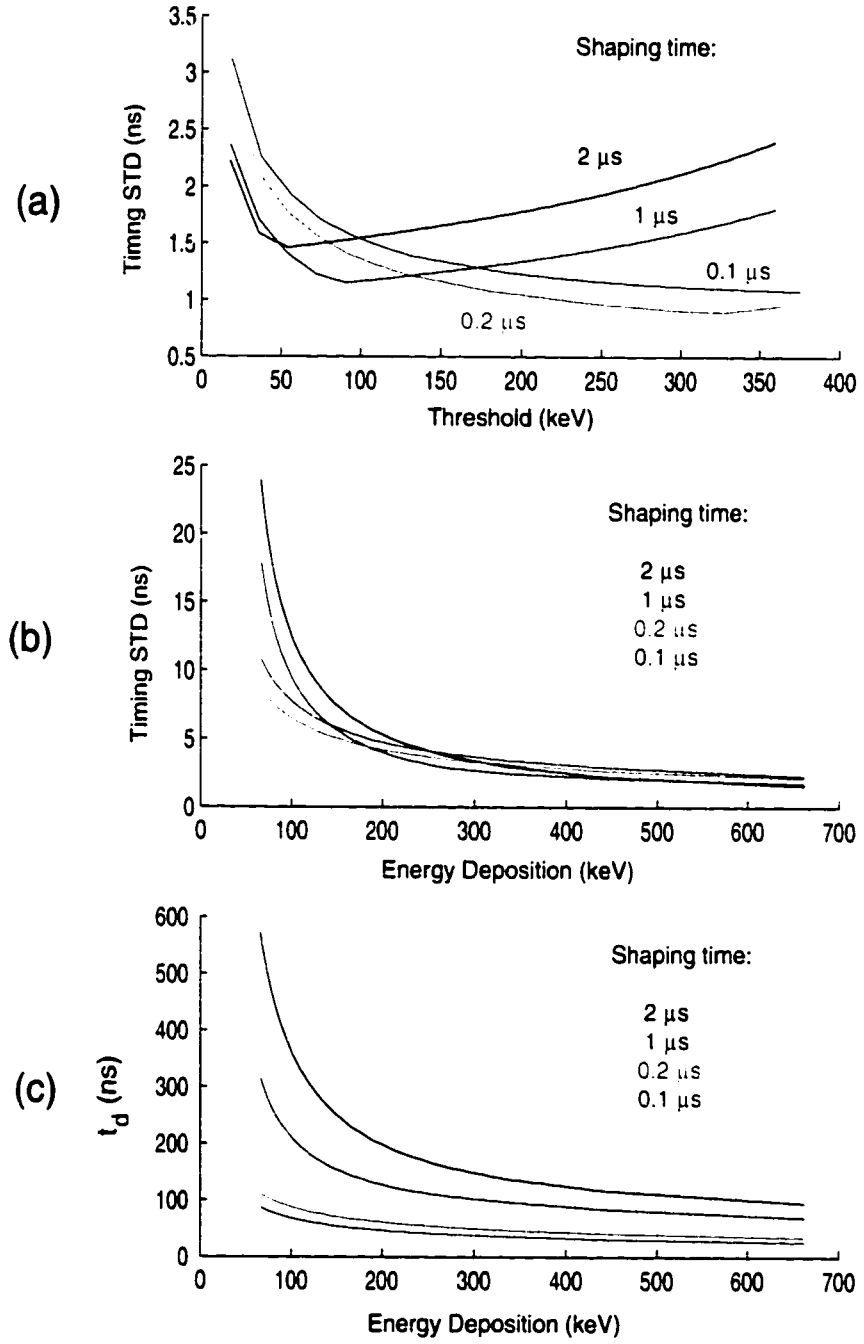

Figure 3.14: Estimated timing resolutions of the anode pixel signals. (a) For 662 keV energy depositions having $z > 0.1$. (b) For an energy threshold of ~40 keV. (c) Estimated time walk with the energy threshold of ~40 keV.

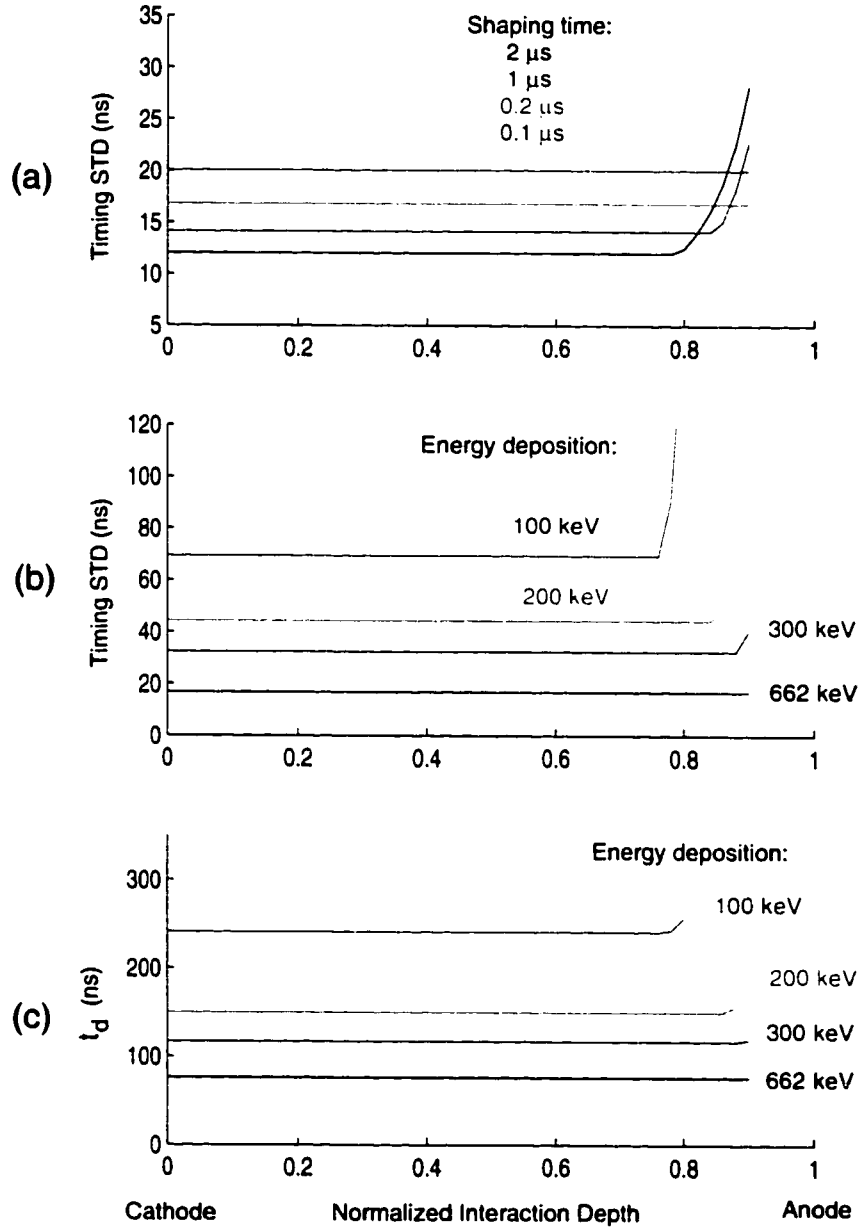

Figure 3.15: Estimated timing resolution of the cathode signal from single-pixel events. (a) For 662 keV energy depositions, and energy threshold equivalent to ~20 keV. Energy deposition near cathode and 1 μs shaping. (b) For 0.2 μs shaping time. (c) Estimated time walk for 0.2 μs shaping time.

the amount of the energy deposition, but also the interaction depth z, according to equation 3.12. With small z (the interaction is near the anode), the signal pulse height from the cathode could be small even for large energy depositions. Thus it is very important to keep a low threshold to make the timing information available from the energy depositions over a broad energy range and over the most of the interaction depths. In the simulation, the threshold is set equal to the pulse height from $\sim$20 keV energy deposition near the cathode after 1 μs shaping. Figure 3.15 (a) shows the simulated timing resolution for the single-site 662 keV energy depositions as a function of the interaction depth. From the results we can see the smaller shaping times (0.1 μs, 0.2μs) yield more uniform timing resolutions over a larger depth range for the events from different interaction depths. The larger shaping times (1 μs, 2μs) yield better values over a majority of the different interaction depths, but the results from the events near the anode are significantly worse. The non-uniformity in the timing resolution from the different interaction depths becomes more severe with smaller energy depositions. To achieve good timing resolution for small energy depositions from the majority of the different interaction depths, the shaping time of 0.2 μs is a reasonable choice. Figure 3.15 (b) shows the simulated timing resolutions for different energy depositions at different interaction depths, with the shaping time of 0.2 μs. The results show a uniform timing resolution can be achieved for the energy deposition as low as 100 keV from the majority of the different interaction depths. The degradation of the timing resolution with the decreasing energy deposition is due to the deteriorated signal-to-noise ratio. Figure 3.15 (c) shows the expected t_d from different energy depositions as a function of the interaction depth (with the shaping time of 0.2 μs). For energy depositions above 100 keV over most of the interaction depths, t_d only depends on the amount of the energy deposition. This

result indicates that the variation of t_d can be corrected with the signal pulse height read out from the anode pixel, which can be considered proportional to the deposited energy.

By comparing the results from figure 3.14 (b) and figure 3.15 (b), we can see that the timing resolution of the cathode signal is much worse than that of the anode pixel signal. Therefore the timing resolution of the measured electron drift time should be dominated by the timing resolution of the cathode signal, and should be about 50 ns FWHM for the 662 keV full energy deposition events from most of the interaction depth. This result indicates a depth resolution of $\sim$0.5 mm FWHM using the method of depth sensing by measuring the electron drift time, according to equation 2.14 and equation 2.15. A similar estimation was performed for the events with 200 keV energy depositions. The results show that a depth resolution of $\sim$1 mm FWHM can be achieved in depth sensing by electron drift time. These results clearly demonstrate that the electron drift time can be effectively used for interaction depth sensing in the 3-D CdZnTe detectors.

CHAPTER IV

3-D POSITION SENSITIVE CdZnTe DETECTORS

4.1 General Considerations

As introduced in the previous chapters, a 3-D position sensitive CdZnTe detector was fabricated with a pixellated anode and a conventional planar cathode. The location of each gamma-ray interaction in the detector can be determined in 3-D using the interaction depth sensing techniques discussed in Chapters 2 and 3. In the design of the 3-D CdZnTe detectors, there are two general parameters considered: the thickness of the detector and the dimension of the anode pixels.

In order to get high detection efficiency for high energy gamma rays, thick detectors are needed. However, the thicker the detector, the more severe the problems of electron trapping and material non-uniformity, and the worse the spectroscopic performance of the detector. To achieve good energy resolution for the events from all of the detector volume, usually a high cathode bias is needed to keep the maximum electron trapping across the detector under ~10%. For a typical $(\mu\tau)_e$ of 3×10^{-3} cm^2/V[Eis.1][Li.3], the cathode bias needed to meet this requirement as a function of the detector thickness is obtained using equation 2.19, and the result is shown in figure 4.1 (a). Assuming a cubic CdZnTe detector with a typical bulk resistivity of

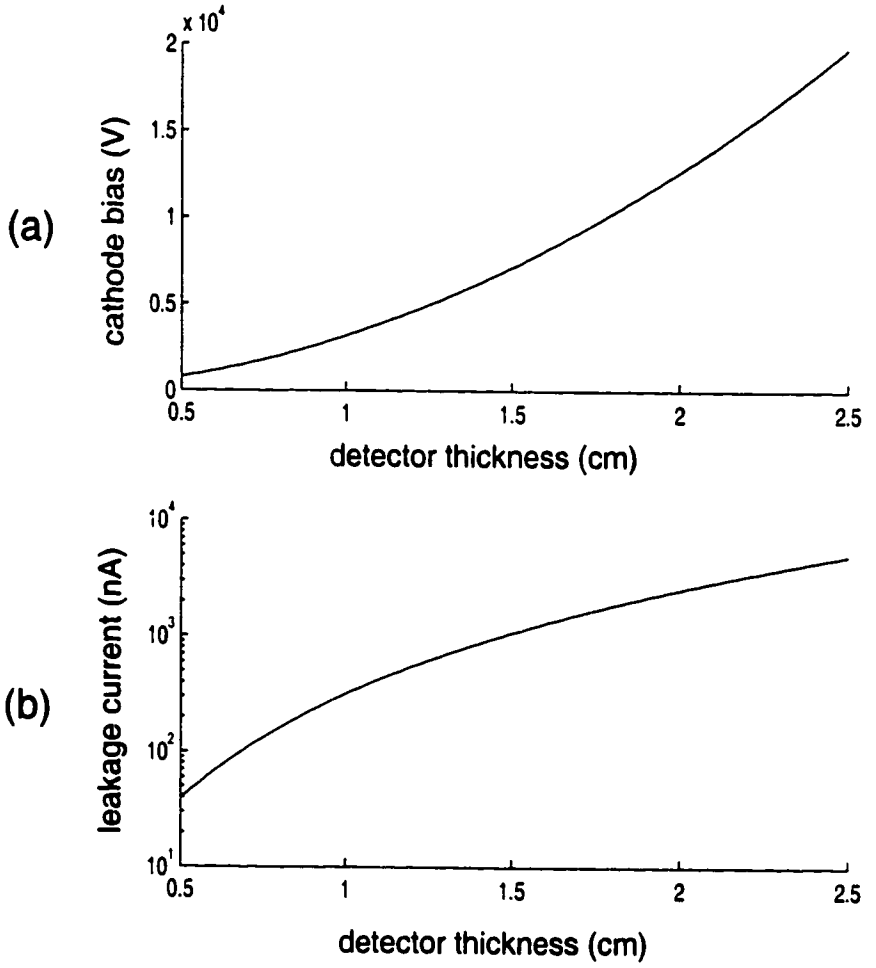

Figure 4.1: (a) The cathode bias needed to keep the maximum electron trapping under 10%. (b) The leakage current in the detector with the cathode bias in (a).

10^{10} Ω-cm[Eis.1][Li.3], the leakage current under the cathode bias in figure 4.1 (a) is shown in figure 4.1 (b). In practice, the leakage current in the detector needs to be kept below $\sim$ 1 μA for a reasonably low electronic noise ($\leq$20 keV FWHM) in the cathode signal, which is important to the interaction depth sensing. In addition, a cathode bias of $\leq$3000 V is preferred for the operation of the detector. With these two considerations, the detector thickness was chosen as 1 centimeter in the design of the two generations of 3-D CdZnTe detectors. According to the simulation in Chapter 3, a 1 cubic centimeter CdZnTe detector has an intrinsic detection efficiency of $\sim$35% and an intrinsic photopeak efficiency of $\sim$8% for 662 keV gamma rays.

In the selection of the pixel dimension, a small ratio of the pixel size to the detector thickness ($\sim$0.1) is desired in order to achieve single polarity sensing (the small pixel effect)[Bar.1]. Therefore, with a detector thickness of 1 centimeter, a pixel size smaller than 1 millimeter should be used. In theory, the smaller the pixel size, the better the likelihood of uniform CdZnTe material underneath the pixel, which implies better energy resolutions from those anode pixels. However, choosing a smaller pixel size will decrease the fraction of the single-pixel events according to the simulation in Chapter 3, and will increase the total number of the electronic readout channels. Therefore, the pixel size used in the two generations of 3-D CdZnTe detectors was $\sim$1 millimeter.

4.2 First Generation 3-D CdZnTe Detectors

The first two 3-D position sensitive CdZnTe detectors were built using 1 centimeter cubic CdZnTe crystals from eV products[EV.1](#eV – 1404 – 10 and #eV – 1404 – 11). Each detector was fabricated with a single planar cathode and an 11×11 pixellated anode by engineers at the NASA Goddard Space Flight Center. The an-

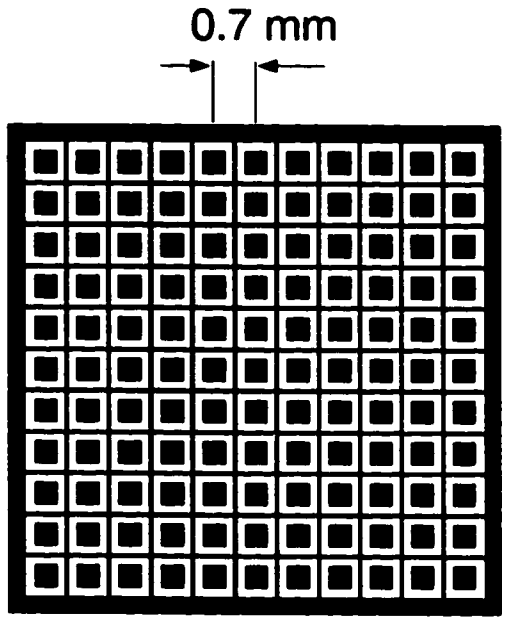

Figure 4.2: Anode pattern of the first generation 3-D CdZnTe detectors.

ode pattern is shown in figure 4.2. In contrast to the conventional pixellated anode illustrated in figure 2.5 (b), our anode pattern has a unique non-collecting grid electrode (100 μm width). During operation, the grid electrode is negatively biased relative to each of the collecting pixel pads. When the electrons from the detector volume move to the region near the anode, the non-collecting grid help to focus the collection of those electrons at the pixel pads. In addition, the transient signal from the grid electrode can be used to monitor the working condition of the detector and, in some cases, used to generate the system trigger signal. The implementation of this non-collecting grid electrode also makes it possible to use a pixel pad (0.2×0.2 mm^2) that is smaller than the pixel size (0.7×0.7 mm^2). Therefore the small pixel effect is enhanced and better single polarity charge sensing is expected.

Figure 4.3 shows the first generation 3-D CdZnTe detector and the electronic

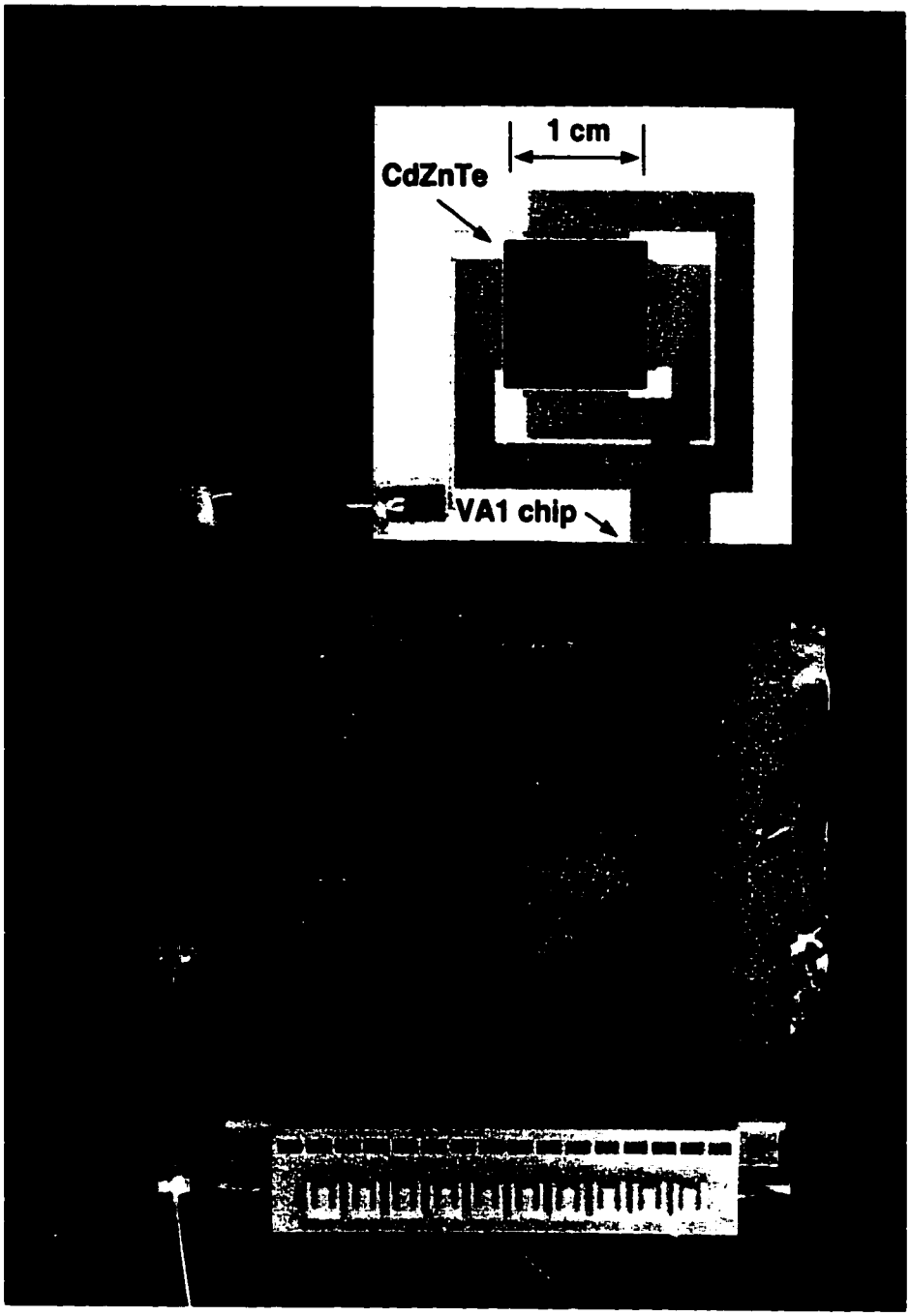

Figure 4.3: Layout of the first generation 3-D CdZnTe detector and the front-end electronics.

readout front-end. The 1 cm^2 anode surface is surrounded by a ceramic substrate. Each anode pixel is wirebonded to the substrate and the substrate is wirebonded to the front-end readout chip, which will be introduced in the next chapter. All the wirebonding was done at the Applied Physics Lab of the Johns Hopkins University.

4.3 Second Generation 3-D CdZnTe Detectors

A second generation of 3-D CdZnTe detectors were fabricated with two differences from the first generation. First, larger CdZnTe crystals ($1.5\times1.5\times1$ cm^3) were used so the detector volume is more than doubled. While the detector thickness (1 cm) and the number of anode pixels (11×11) were kept unchanged, the pixel size was enlarged from 0.7×0.7 mm^2 to 1.2×1.2 mm^2, with the collecting pad of each pixel enlarged from 0.2×0.2 mm^2 to 0.7×0.7 mm^2.

The second difference is in the design of the ceramic substrate and its connection to the 3-D detector. In the first generation 3-D CdZnTe detectors, each anode pixel was wirebonded to a corresponding pad on the ceramic substrate. After the wirebonding, the 121 arching bare wires above the anode surface make the detector very fragile. For the second generation 3-D CdZnTe detectors with larger anode area (1.5×1.5 cm^2, from eV products), the wirebonding would have been more challenging because of the longer wires needed. Instead of wirebonding, an alternative technique called plate-through-via was used to make the detector-readout connections. An array of 11×11 holes was fabricated on a ceramic plate (the substrate) that geometrically aligns with the 11×11 anode pixels of the detector. Each hole is connected to a pad located at the edge of the plate by a fan-out line built in the multi-layer plate. A bottom view of the ceramic plate is shown in figure 4.4. Before the ceramic plate is connected to a detector, each hole on the plate is filled with

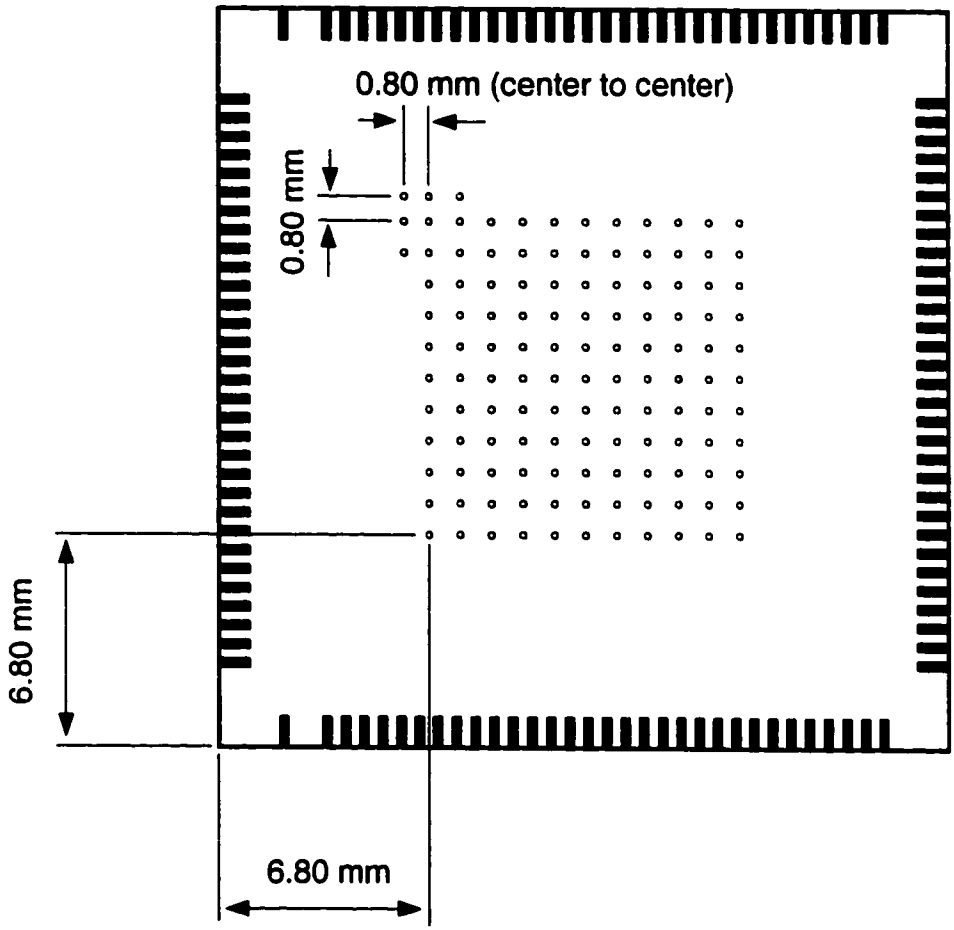

Figure 4.4: Bottom view of the ceramic substrate.

a small amount of conductive glue. After the array of holes is accurately aligned with the array of anode pixels on the detector, the ceramic plate is placed onto the anode of the detector so each pixel is connected to the corresponding hole by the conductive glue. By using this technology, rigid connections between the substrate and the detector were achieved.

Figure 4.5 shows the second generation 3-D CdZnTe detector and the electronic readout front-end. The second generation readout front-end consists of 4 VAS-TAT chip pairs, which will be introduced in the next chapter.

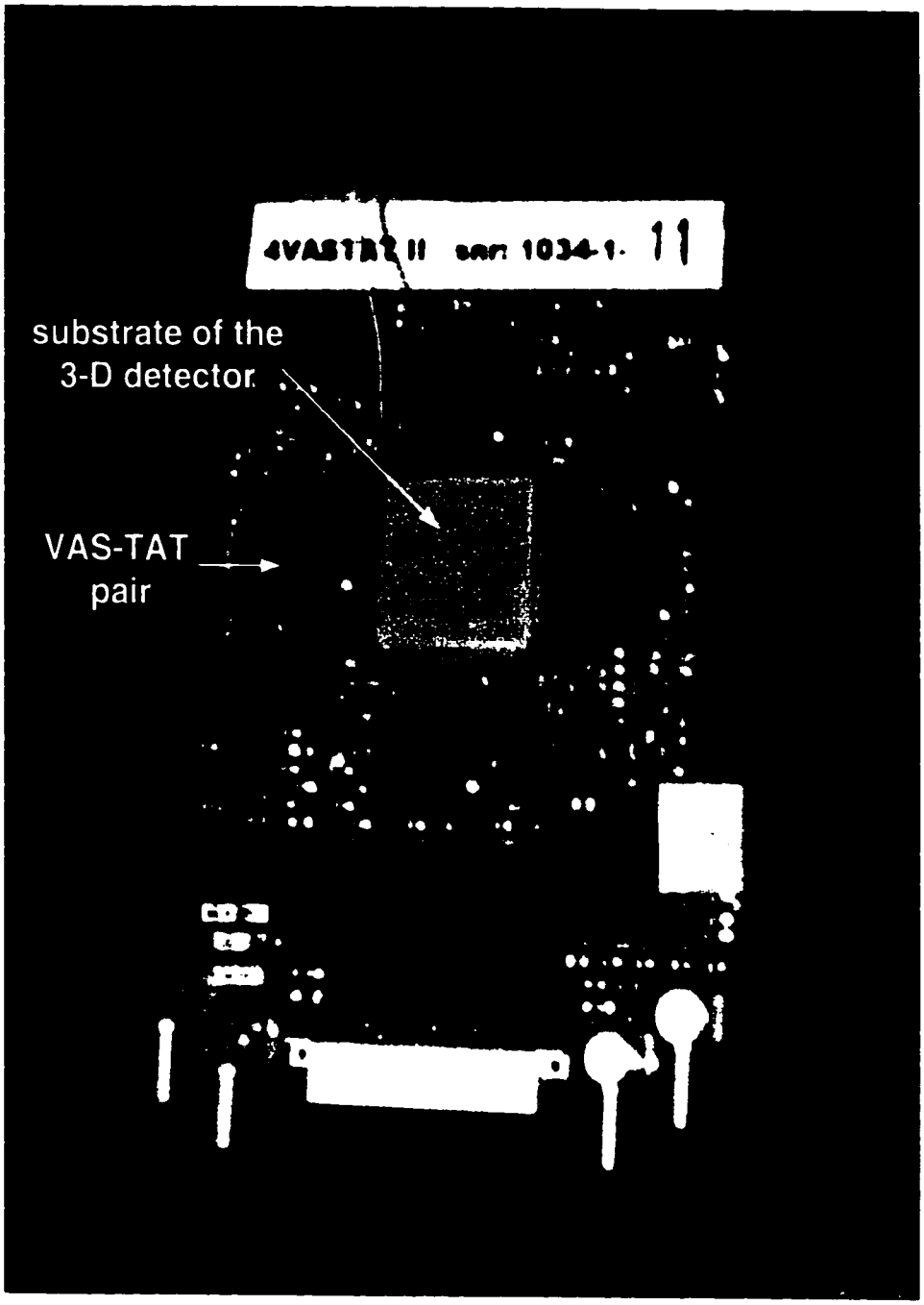

Figure 4.5: Layout of the second generation 3-D CdZnTe detector and the front-end electronics.

CHAPTER V

ELECTRONICS

According to the working principle of the 3-D CdZnTe detectors, for each gamma-ray interaction in the detector, the signals from the 11×11 anode pixels and the cathode need to be read out and combined together to determine the amount and 3-D location of the energy deposition. To serve this purpose, a multiple-channel readout system needs to be developed, preferably using integrated multiple-channel readout chips because of the large number of independent readout channels needed.

5.1 First Generation Readout System

The first generation readout system was designed and developed to work with the first generation 3-D CdZnTe detectors. In the first generation system, interaction depth sensing by the C/A ratio is used to determine the interaction depth for the single-pixel events. Therefore, multiple-pixel events are not depth registered correctly, but only the signal pulse heights from the cathode and anode pixels need to be read out. The first step in the electronic system design is the selection of an appropriate multiple-channel readout chip.

Table 5.1 shows the characteristics of three typical analogue multiple-channel readout chips: the VA1 chip from IDE AS[IDE.1], the Alice128C chip from IreS[Mar.1],

Table 5.1: Characteristics of some multiple-channel readout chips.

	VA1	*Alice128C*	*RENA*
Channel/chip	128	128	32
Dynamic Range (fC)	40	48	8
Signal Polarity	Both	Both	Both
Peaking Time (μs)	0.5~3	1.4~2	0.4~6
ENC (electrons)	165+6.1/pF	290+8/pF	~150
Power Consumption (mW/ch)	1.2	0.34	6.5
Sparse Readout	Coming	No	Yes

and the RENA chip from NOVA R&D[NOV.1]. The selection of the readout chip depends on if the chip's major characteristics (such as dynamic range, electronic noise) meet the requirements from the expected performance of the detectors. Each of the two first generation 3-D CdZnTe detectors is a 1 cm^3 cubic crystal. The energy range of interest is from a few keV to a few MeV. Therefore, the equivalent dynamic range of the readout chip must be at least 1 MeV (~40 fc according to 4.7 eV per signal carrier for CdZnTe). In addition, the expected energy resolution (~1% FWHM at 662 keV) implies the equivalent electronic noise of the system should be no more than a few keV. Table 5.1 shows the VA1 chip has the preferred combination of a large dynamic range (40 fC) with a low electronic noise (165+6.1/pF electrons rms), so it was adopted as the front end of the first generation 3-D CdZnTe detectors. For CdZnTe, the equivalent dynamic range and electronic noise of the VA1 chip are ~1 MeV and 0.8 keV + 0.033 keV/pF rms respectively.

The block diagram of a VA1 chip is shown in figure 5.1. Each VA1 chip has

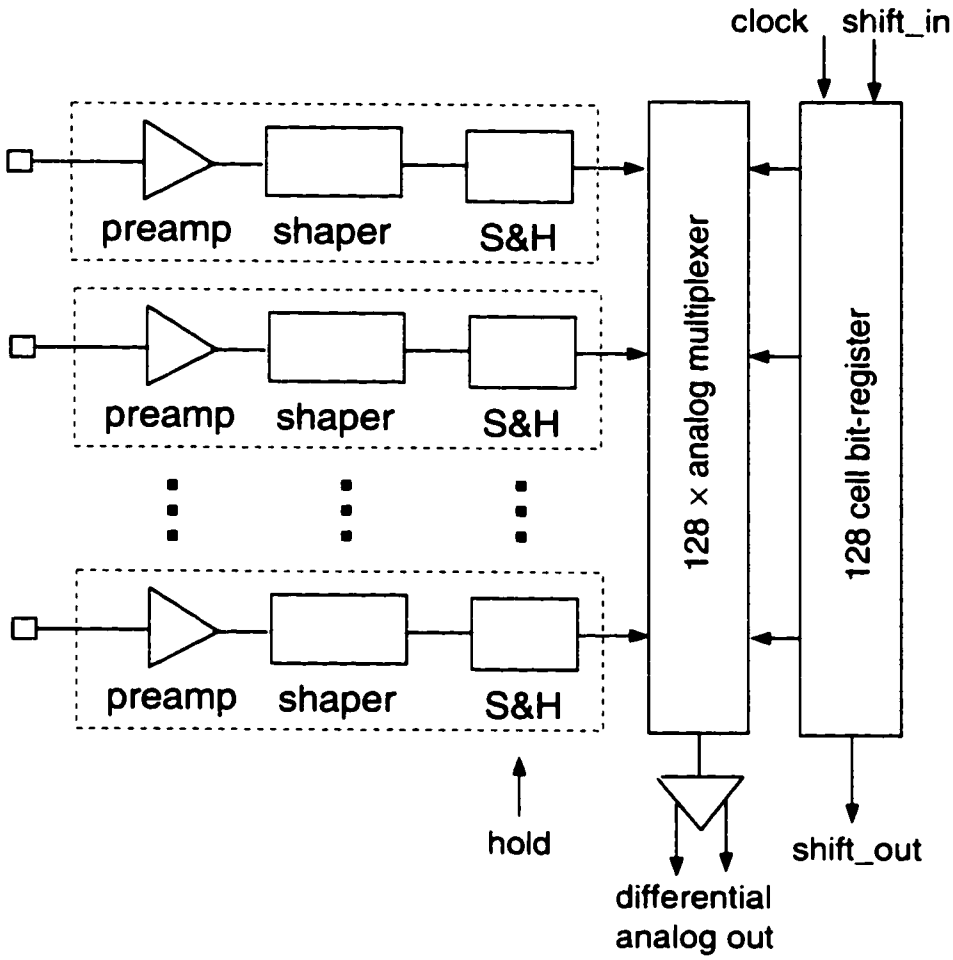

Figure 5.1: Block diagram of the VA1 chip.

128 independent signal readout channels. All VA1 readout channels are "identical" and each includes a preamplifier, a shaper and a sample/hold circuit. For an event from the detector, the outputs of the 128 channels are read out serially through a multiplexer built in the chip, under the control of two digital signals: clock and shift_in. This working mode of parallel processing and serial readout simplifies the communication with the follow-up circuits, but at the expense of a long dead time for serially reading out every channel in the VA1 chip. Sparse readout capability (available in the RENA chips) would increase this throughput rate, but is unavailable in the VA1 chip. The event processing rate of the VA1-based readout system is $\sim$1 K/sec.

In the first generation readout system, the VA1 chip is mounted on a "hybrid" circuit board which provides the physical support to the VA1 chip and is responsible for the communications with the follow-up circuits. The connection between the VA1 chip and the 3-D CdZnTe detector was shown in figure 4.3. Two separate charge-sensitive preamplifiers (A250) from AMPTEK[AMP.1] are used to read out the signals from the cathode and grid electrode. These two signals are very useful for monitoring the working condition of the detector, and provide the system trigger signal for the triggerless VA1 chip. The cathode signal is also used in the derivation of the interaction depth. An AT-MIO-16E-1 DAQ board from National Instruments[NAT.1] is used as the A/D converter. The additional D/A converter, timers and DIO lines on this board are used to generate the analog and digital signals for system testing and control.

The block diagram of the first generation readout system is shown in figure 5.2. For each 3-D CZT detector, a VA1-based hybrid/repeater module from IDE AS is used to read out the signals from the 11$\times$11 anode pixels. The repeater card

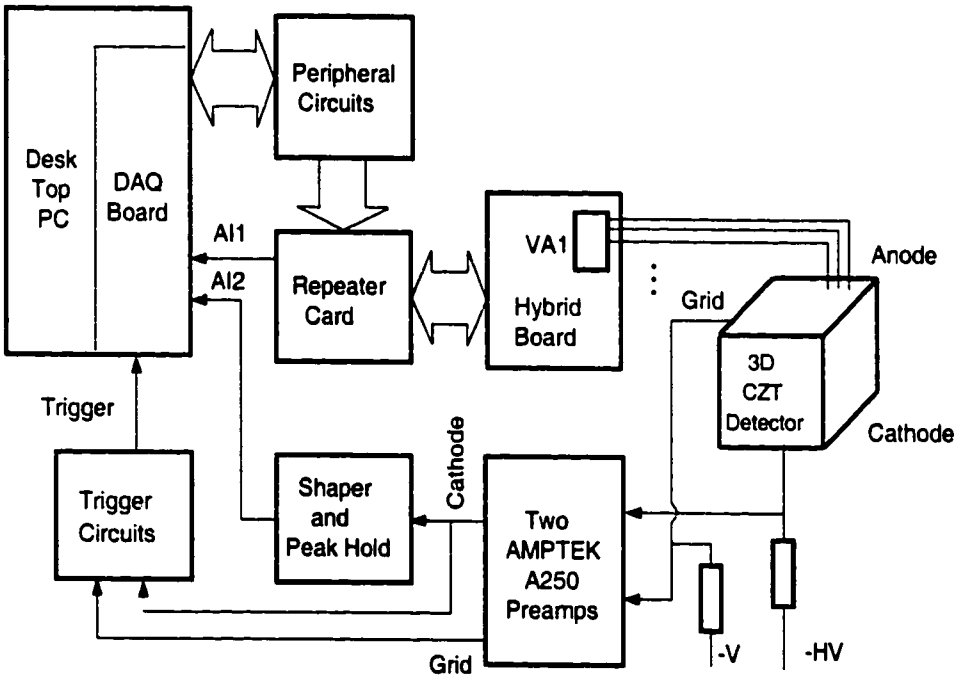

Figure 5.2: Block diagram of the readout system.

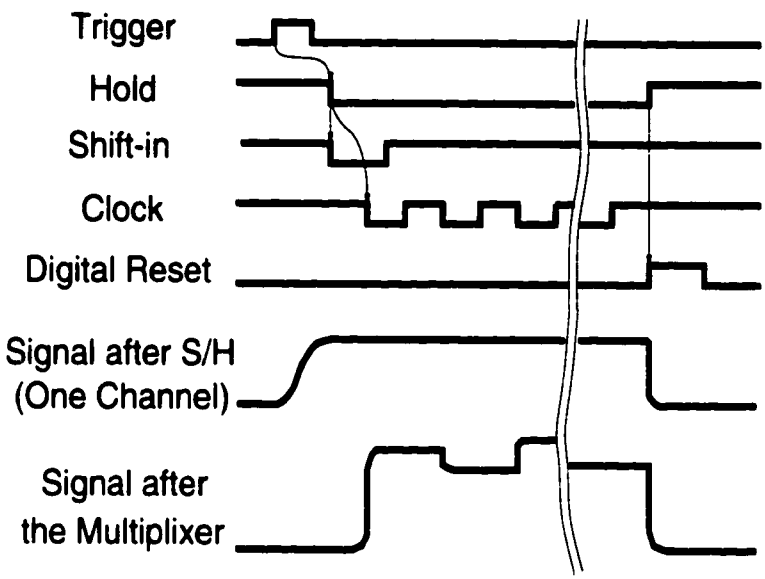

Figure 5.3: The control signals of the readout system and the corresponding output from VA1 chip.

acts as an interface between the hybrid board and the follow-up DAQ circuits. The peripheral circuit performs the level shift from TTL to differential TTL for the digital control signals sent to the repeater card, and also generates the clock signal which synchronizes the A/D conversion and VA1 channel switching. The control signals of this system are shown in figure 5.3. For each interaction event in the detector, the system trigger signal is generated by the trigger circuits from either the cathode signal or the grid signal. Initiated by the trigger signal, the DAQ board and peripheral circuits generate the four digital control signals for the VA1 chip: Sample/Hold, Shift-in, Clock and Digital-reset. The falling edge of Sample/Hold signal holds the signal of each VA1 readout channel at the peak (if the timing is correct), then the first clock pulse works with the valid (low) Shift-in signal to start the channel switching. Each falling edge of the clock signal switches the output of VA1 chip to the next

channel and starts the corresponding A/D conversion. After the 128th clock pulse, all the VA1 channels have been read out, and the Sample/Hold signal returns to high and initiates the Digital-reset signal to reset the VA1 chip.

5.1.1 Sample/Hold Signal Timing

In the first generation readout system, the Sample/Hold signal is generated by a programmable timer on the DAQ board. Triggered by a system trigger signal, the timer outputs the Sample/Hold signal after certain delay. The length of delay and the pulse width are preset by software. The delay ($\sim$1 μs) is set according to the shaping time of the shapers on VA1 chip to make the beginning of the Sample/Hold signal coincide with the peak of the signal from each shaper. The pulse width is set to be long enough ($\sim$300 μs) to cover the channel switching and A/D conversion time. Since the timer uses the 20 MHz clock on the DAQ board, the maximum time walk on the Sample/Hold signal due to the timer itself is 50 ns. The relative error in amplitude sampling induced by this time interval is less than 0.3% and so is negligible when the shaping time of VA1 chip is larger than 1 μs.

5.1.2 System Trigger Signal

The system trigger signal has to be generated from the cathode or the grid signal since it is not available from the VA1 chip. Because the Sample/Hold signal is initiated by the system trigger signal, the trigger signal needs to occur at a fixed time relative to the pixel signal to guarantee accurate sampling of peak amplitude. However, the time-dependence of the signals from the cathode and the anode pixels are depth-dependent, and variations arise from the different electron drift times from the interaction location to the anode. Thus, the cathode signal can not be used to generate the trigger signal since interactions may occur at any depth. Instead the

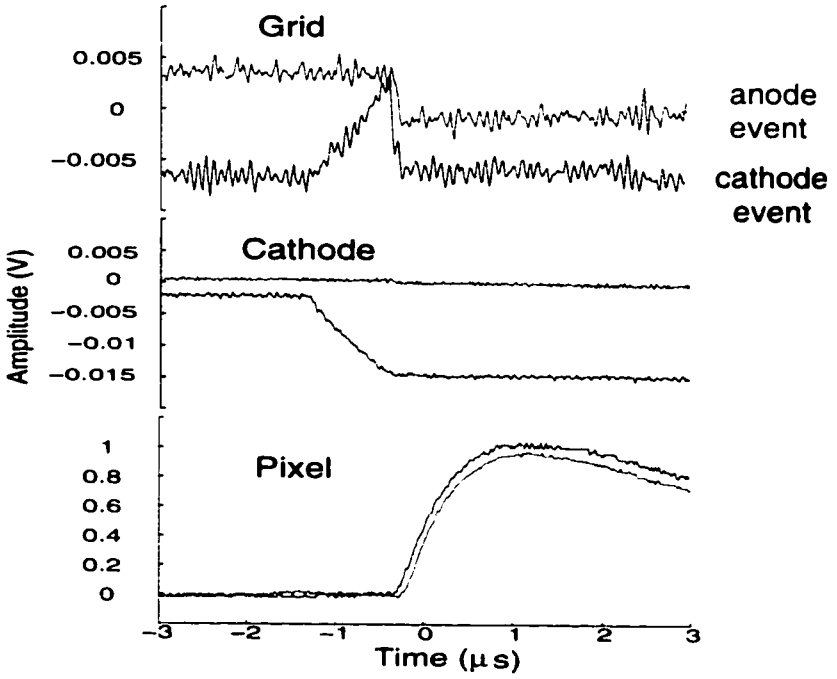

Figure 5.4: Signal waveforms from two events in a first generation 3-D CZT detector. Event 1: near anode surface. Event 2: near cathode surface.

transient signal from the anode grid is used to generate the trigger signal. Figure 5.4 shows the signal waveforms for two single-pixel events from 662 keV photons. The waveforms of the cathode and the grid signals are recorded from the outputs of the preamplifiers, and the waveform of the pixel signal is taken after the shaper on the VA1 chip. The interaction depths are near the anode surface (shown in red) and near the cathode surface (shown in blue). Figure 5.4 clearly shows the sharply falling edge on the grid signals which correspond to the time when electrons are collected by the anode pixel. These sharp falling edge coincide with the starting times of the pixel signals. In the trigger circuits, a differentiator is used with a threshold circuit to pick out the falling edge and generate the system trigger signal. Because the grid signal is transient, the signal-to-noise ratio is poor. As a result, the energy threshold of this triggering mode is kept larger than 100 keV, which precludes detecting low

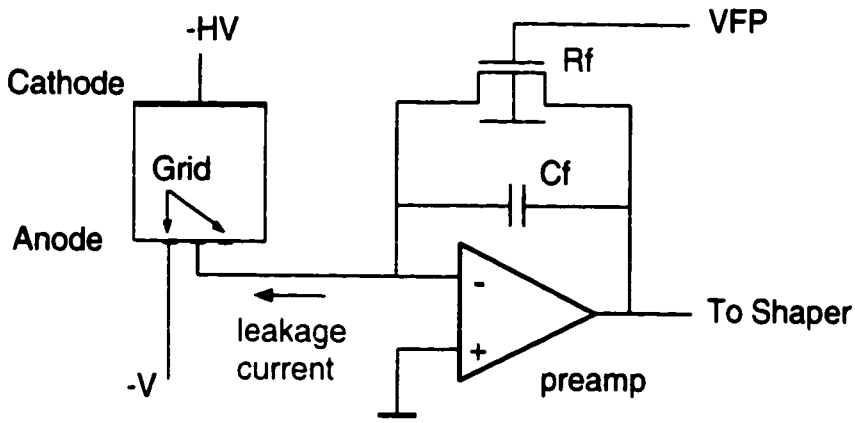

Figure 5.5: The input of the preamp of VA1 chip.

energy gamma rays in this mode.

Fortunately, for the detection of low energy gamma rays, most of the interactions should occur near the surface of the detector. By irradiating from the cathode side, the cathode signal can generate the system trigger signal. In this case the cathode signal has the best signal-to-noise ratio and nearly a constant timing relative to the pixel signal. For this case, the energy threshold can be lowered under 10 keV.

5.1.3 Electronic Noise

The electronic noise of the first generation readout system is mainly due to the preamplifier on the VA1 chip. A schematic plot of a preamplifier and its connection to the detector is shown in figure 5.5. An FET is used as a feedback resistor to perform the discharge of the preamplifier. The equivalent resistance value Rf of the FET can be adjusted by shifting the FET bias VFP. In order to minimize the induced noise, Rf is usually kept as high as possible while allowing the preamplifier to discharge properly. In our two 3-D CZT detectors, the anode pixels are directly wirebonded to the input pads of VA1 channels to form the DC coupling. Without any applied detector bias, the equivalent electronic noise of the VA1 chip in the

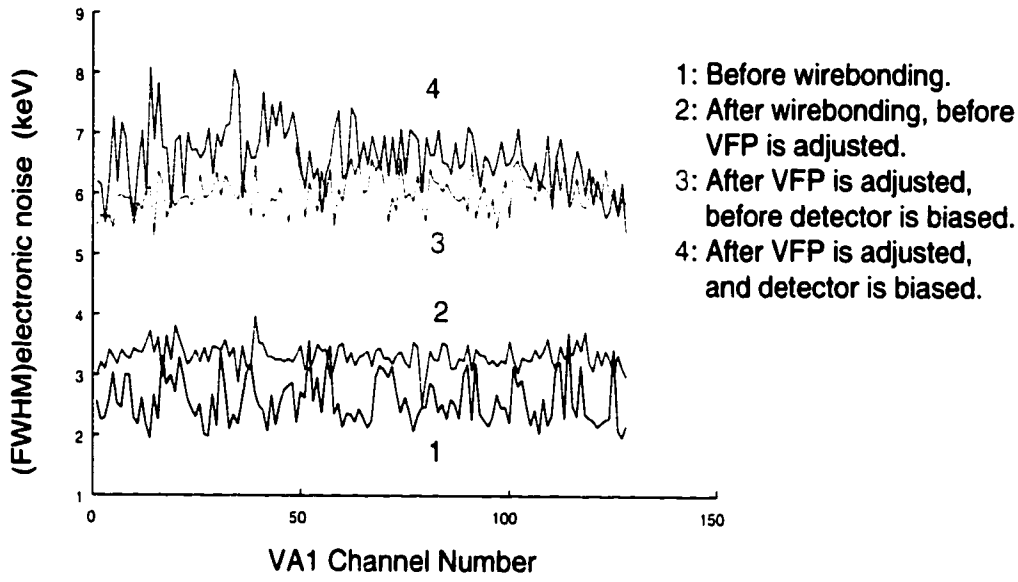

Figure 5.6: The electronic noise for each VA1 channel.

two 3-D CZT detectors were measured before and after the wire bonding. Similar results were acquired for both detectors. Figure 5.6 shows the results in FWHM of equivalent energy for detector #1 before (case 1) and after (case 2) the wirebonding. The equivalent electronic noise in both cases is around 3 keV and approach the manufacturer's performance claims. The slight increase of the electronic noise in case 2 is attributable to the increased capacitance from wirebonding.

After the detector biases are applied, leakage current flows through the pixels and through the feedback FETs of the preamplifiers because of the DC-coupling. Under normal detector biases the leakage current flowing through a pixel is around a few nA, which could saturate the preamp if the feedback FET worked in its normal condition. To compensate, VFP needs to be adjusted so the preamp can tolerate larger leakage current. Unfortunately, the equivalent electronic noise then increases due to the reduced value of Rf. For detector #1, figure 5.6 shows the results after VFP was adjusted to allow operation with an increased cathode bias of -2400 V and

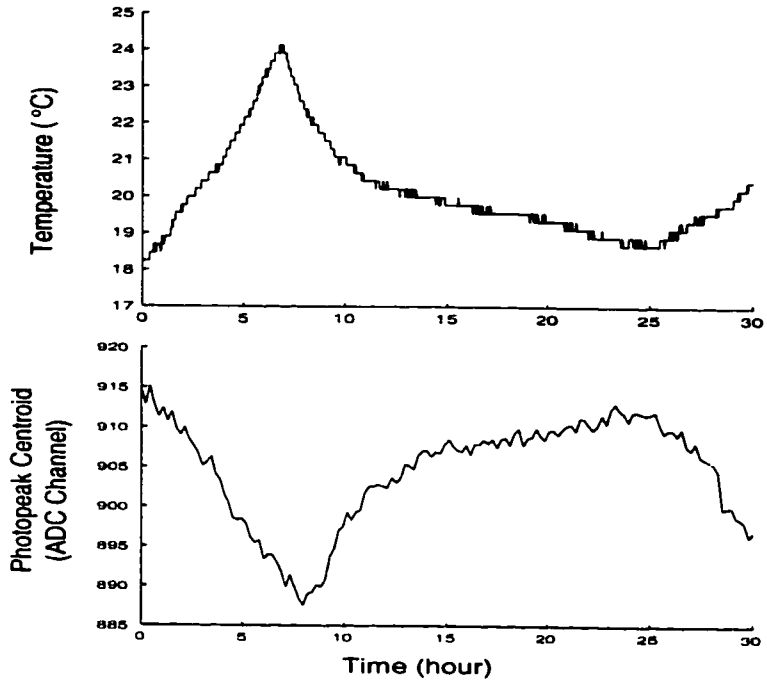

Figure 5.7: Variation of temperature and drift of photopeak centroid at 662 keV in 30 hours.

grid bias of -50 V. The electronic noise of the VA1 chip was measured with (case 4) and without (case 3) the detector biased. The results clearly show the increased noise associated with reducing Rf. For detector #2, a higher leakage current and limit on the VFP adjustment limited the cathode bias to only -1400 V with grid bias of -50 V. The electronic noise of the VA1 chip was still measured to be ~6 keV. The electronic noise of the VA1 chip (~7 keV) should be significantly improved by introducing AC or AC equivalent coupling between the VA1 chip and the detector.

5.1.4 Spectrum Stabilization

To test system stability, the drift of the gain of the VA1 chip was observed while the ambient temperature changed. Figure 5.7 shows the variation of ambient temperature and the drift of 662 keV photopeak centroid as measured by a 3-D CZT detector over 30 hours. During the experiment the baseline of the VA1 chip was also

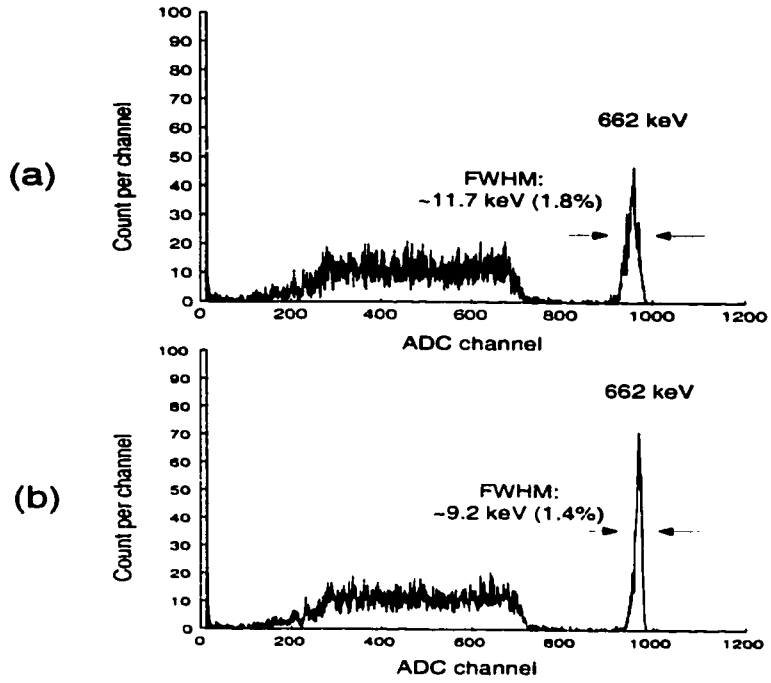

Figure 5.8: ^{137}Cs spectrum of single-pixel events from a voxel in detector #1, collected over ~70 hours. (a) Without stabilization. (b) With stabilization.

recorded and no obvious drift was observed, showing that any drift of the photopeak centroid was due to the variation of system gain. The temperature coefficient of the relative gain was observed to be ~-0.5%/°C and quite uniform for each VA1 channel.

In spectra collected with a 3-D CZT detector, the collection time may extend to as long as a few days for adequate statistics in the voxel-based spectra. This long acquisition time is because of the low activity of the radiation source and low count rate capability of the serial readout. During this long period, the spectrum stabilization is performed by gain correction software. Only one gain correction coefficient is needed because the temperature coefficients are quite uniform for all VA1 channels. To determine the gain correction coefficient, a prominent photopeak in the spectrum is normally needed as the reference peak. The gain correction coefficient is updated periodically according to the reference photopeak centroid from the spec-

trum collected in the most recent counting time interval. This method works well if a prominent photopeak is available in the energy spectrum being measured. For example, figure 5.8 shows the difference of the ^{137}Cs spectra simultaneously collected from a voxel of detector #1 with and without spectrum stabilization. During this ~70 hours experiment, the ambient temperature varied in the range from 18 °C to 24 °C.

5.1.5 Software

The software for system testing was developed using Labview^{TM}. In testing mode, the software tells the DAQ board to send a test signal to the VA1 chip and read the response. The amplitude of the test signal is determined by the output of the DAC unit on the DAQ board, which is also controlled by the testing software. By this means, the software can automatically measure the baseline and the responses to test signals for each of the 128 VA1 channels. The electronic noise and dynamic range of each VA1 channel are available from the measurement results, both of which are important in monitoring the performance of the VA1 chip. The major Labview testing programs are listed in table 5.2, as well as their functions.

The software for spectrum collection and processing is written in C for its fast access to large memory blocks needed in spectrum storage. The flow chart of the software for recording one interaction event in spectrum collection is shown in figure 5.9. For a single-pixel event, after the amount of energy deposition and the 3-D interaction location are determined, the event is recorded in the corresponding energy spectra in an 11×11×20 voxel-based spectra array. For a multiple-pixel event, after the total energy deposition and the number of anode pixels involved are determined, the event is recorded accordingly in another spectra array. For two-pixel events, more

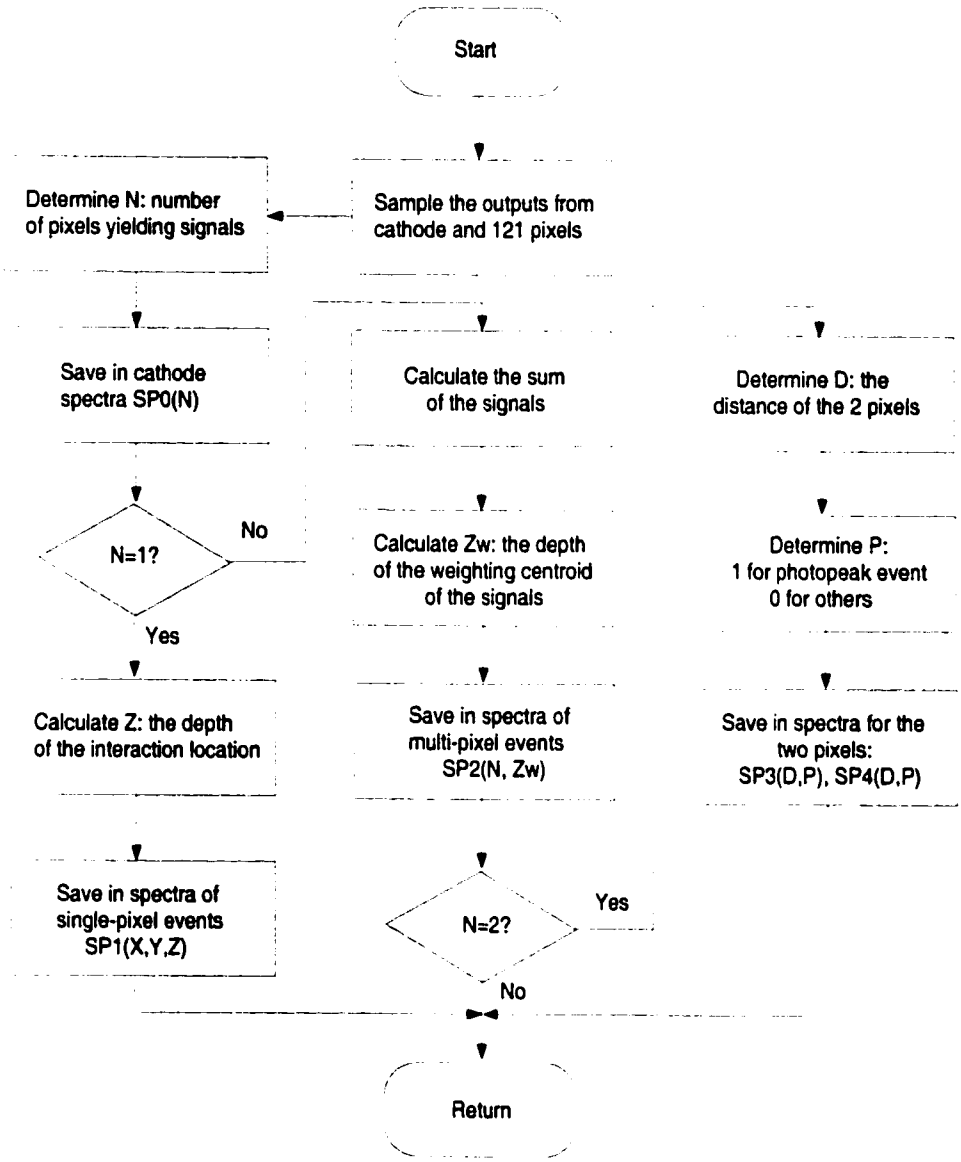

Figure 5.9: Flow chart of software for recording one interaction event.

Table 5.2: Labview programs for testing the first generation readout system.

Subvi Name	Function
Single Test.vi	Testing a selected channel in the VA1 chip.
Multiple VA1 Channel Baseline Analysis.vi	Measuring the baselines and noise levels of all 128 VA1 channels.
Multiple VA1 Channel Test Response.vi	Measuring the responses to a calibration signal from all 128 VA1 channels.
Test Response Curve of Specified VA1 Channel.vi	Automatically measuring the test response curve of a selected VA1 channel.

information (including the distance between the two pixels and the energy spectra from each pixel) is also recorded. This information is used in the investigation of the signal sharing between two pixels and can be compared with the simulation results. All the spectra collected in one measurement can be saved as a binary file, which can be reloaded into the program for display or further analysis.

From the voxel-based energy spectra array of single-pixel events, the 3-D distribution of photopeak centroid and energy resolution can be obtained using the software. This information can be used in the non-uniformity analysis of detector material. In the application of gamma spectroscopy, the 3-D distribution of the photopeak centroid can be used to register the spectra from all the voxels and yields an overall spectrum from the whole detector with high energy resolution.

5.2 Second Generation Readout System

In collaboration with IDE AS, the second generation readout system (MCR3 system) is designed and developed to work with the second generation 3-D CdZnTe detectors[Mae.1]. Compared with the first generation readout system, the MCR3 system has 128 improved energy readout channels and 128 newly-implemented timing channels. In the MCR3 system, not only can the signal pulse heights from the cathode and each anode pixel be read out separately, but also the leading edge timing information associated with each signal. This makes it possible to derive the electron drift time for each energy deposition in the detector. For gamma-ray interactions in the detector, the interaction depths of the single-pixel events can be determined by either the C/A ratio or the electron drift time. For the multiple-pixel events, each individual interaction depth of the multiple energy depositions can be reconstructed with depth sensing by the electron drift time, if the amplitudes of the energy signals are above the threshold of the timing channels. The core of the MCR3 system consists of four custom VAS-TAT chip sets, designed and developed exclusively for the second generation system.

5.2.1 VAS and TAT Chips

Each VAS chip has 32 independent energy readout channels improved from the original design of VA1 chip. The improvements on each channel include the implementations of a leakage current compensation unit (CC unit) and a peak-hold circuit. The CC unit is designed to compensate for the leakage current of a few nA from each anode pixel, thus providing AC-equivalent coupling between the detector and the readout channel and reduced electronic noise. Unfortunately, our CC unit failed to reach a low compensation threshold and the minimum leakage current which

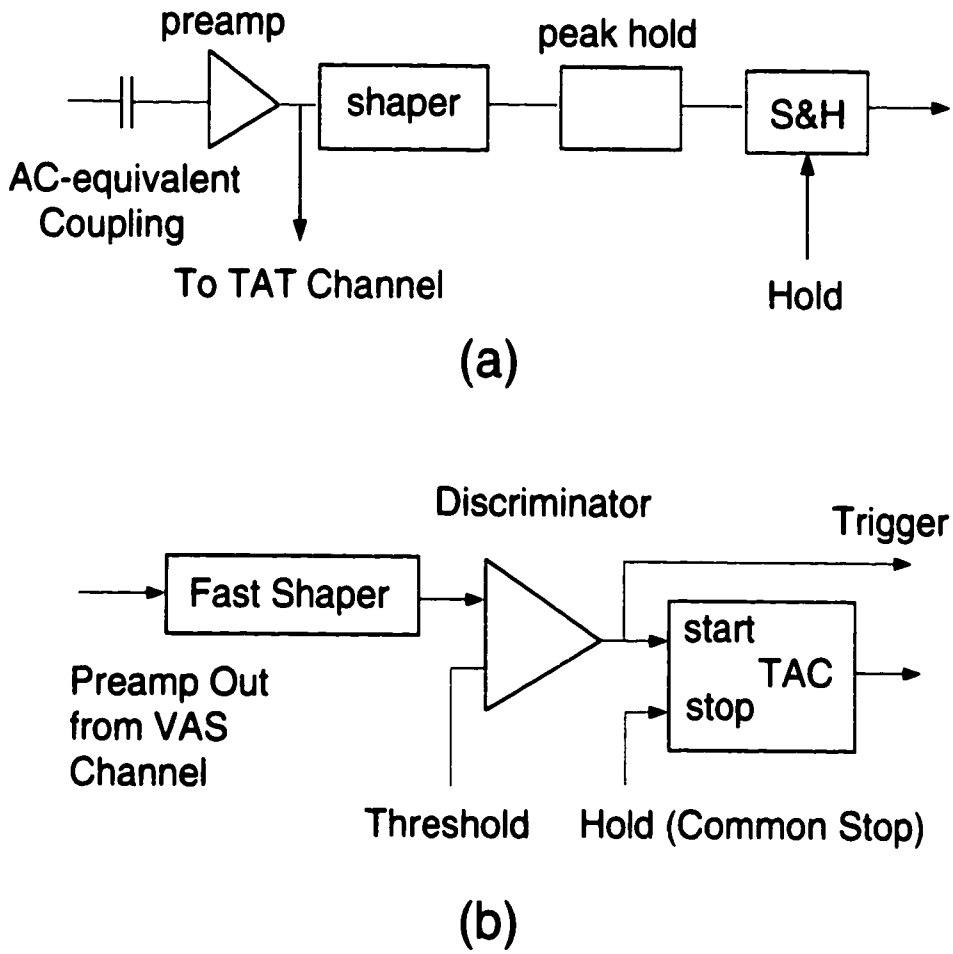

Figure 5.10: Channels in the VAS and TAT chips. (a) VAS channel. (b) TAT channel.

can be compensated is too high (~10 nA). Therefore, the VAS channels still are used in the noisier DC-coupling mode. The new peak-hold circuit makes the pulse height sampling independent of the timing of the Hold signal. As a result, the pulse height sampling is more accurate, especially for the events involving multiple anode pixels. In general, each VAS channel includes a charge sensitive preamplifier, a shaper, a peak-hold circuit and a sample/hold circuit, as illustrated in figure 5.10 (a). The outputs from all the energy channels can be read out serially through a multiplexer built in the VAS chip. In addition, the output of each preamplifier is made available to the corresponding timing channel in the TAT chip.

Each TAT chip has 32 independent timing channels. Each timing channel includes a fast shaper, a discriminator and a TAC unit, as shown in figure 5.10 (b). The fast shaper receives the preamplifier output from the corresponding VAS channel. When its output exceeds a preset threshold, the discriminator will generate a digital trigger signal which is used as the start signal of the TAC unit. The TAC units from all the timing channels share a common stop signal (Hold signal) to guarantee the identical timing reference for each timing channel. Similar to the VAS chip, the outputs from all the timing channels can be read out serially through a multiplexer in the TAT chip. The system trigger signal is generated in the TAT chip by combining the digital trigger signals from all the timing channels. A TAT chip also includes an internal register which contains 32 control bits corresponding to the 32 timing channels. Each control bit can be adjusted separately to enable/disable the digital trigger from the corresponding timing channel.

To accommodate the readout of the cathode and anode grid signals in the VAS-TAT chips, the first channel of each VAS/TAT chip is designed to operate with opposite polarity to the other 31 channels and is referred to as the special channel.

The output of the preamplifier in each special channel is made available to the user through a fast line driver, so the pulse waveforms of the cathode and anode grid signals can be monitored to check the working condition of the detector. However, for the first MCR3 system working with a 3-D detector, the special channel used to read out the cathode signal experienced a gradual decrease in the output pulse height, and finally did not work at all. This might have been due to the large pick-ups in the cathode signal from the digital control signals, which made the cathode readout channel suffer from frequent deep saturation and finally break down. As a replacement for the special channels, a discrete circuit was developed in the readout system we used to read out the cathode and anode grid signals.

5.2.2 System Structure

The block diagram of the MCR3 system is illustrated in figure 5.11. The whole system consists of three major components: the multiple-chip module board, the controller card, and the DAQ board in the PC. The module board is similar to the hybrid board in the first generation system. It provides the physical support to the four VAS-TAT chip sets, which provide the 128 energy readout channels and the 128 timing channels. The module board is also responsible for the connections to the 3-D detector. The controller card is similar to the repeater card in the first generation system. It acts as an interface between the DAQ board and the module board. In addition, the controller card includes a VA readout engine resident in a Xilinx[XIL.1] programmable logic chip. The VA readout engine has the capability to generate the VAS-TAT control signals from the system trigger and the clock signal. The DAQ board is a PCI6110E board from National Instruments, which performs similar functions to the AT-MIO-16E1 board in the first generation system.

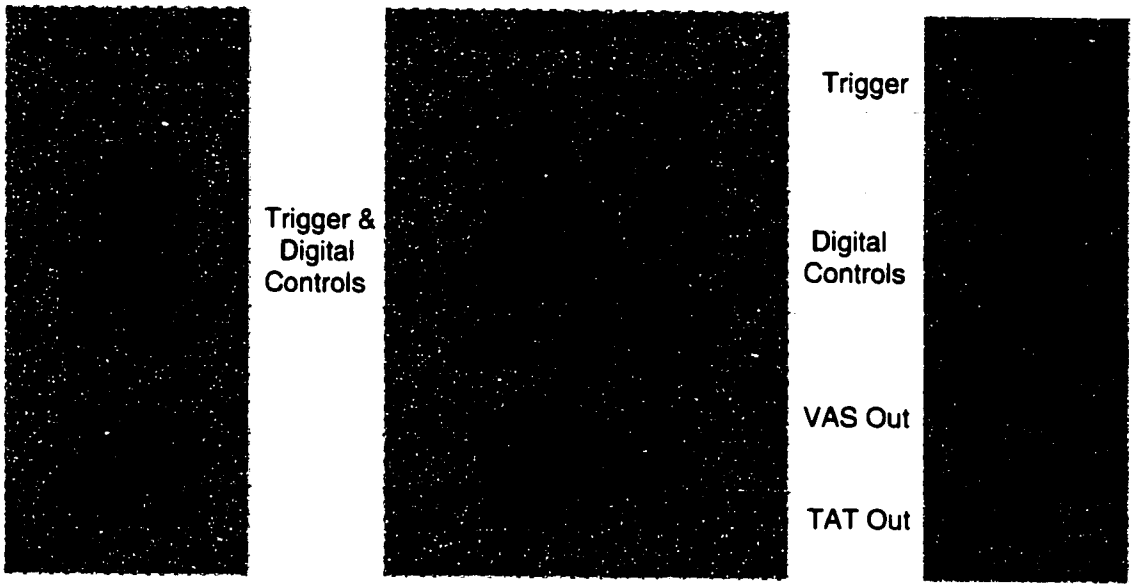

Figure 5.11: Block diagram of the second generation readout system.

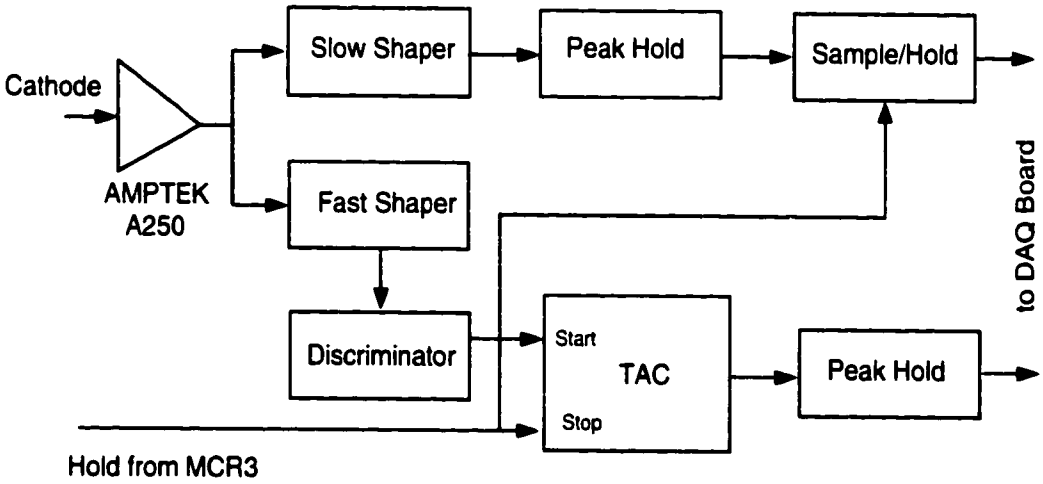

Figure 5.12: Diagram of the discrete circuits for readout of the cathode signal.

The data acquisition of the MCR3 system can be initiated by three different trigger signals: the program trigger, the external trigger, and the trigger from the TAT chips. The program trigger is generated by the software and used for system testing in the absence of the detector. The external triggering mode makes it possible for the data acquisition to synchronize with some other devices (e.g., in a coincidence measurement). The trigger from the TAT chips makes it convenient for the MCR3 system to operate with the signals directly from the 3-D CdZnTe detector.

The readout of the cathode signal is vital input to the two interaction depth sensing techniques. Because the special channels of the MCR3 system do not work as expected, this task can not be performed by the MCR3 system itself. Thus in the second generation readout system, the cathode signal is read out through the discrete circuit diagrammed in figure 5.12. The discrete circuit serves the same function as the special channel in the MCR3 system, and its signals are integrated into the MCR3 system. Therefore, the timing and the pulse height of the cathode signal can be read out simultaneously with the signals from the anode pixels during operation of the MCR3 system.

5.2.3 Software

The software of the MCR3 system is developed in IDE AS with Labview^{TM}. Generally speaking, there are three functions integrated in the software: system setup, system testing, and data acquisition. Each function is performed using different subroutines, known as subvis. The major subvis in the software of the MCR3 system and their functions are shown in table 5.3. The hierarchy of the subvis is shown in figure 5.13.

Table 5.3: The major subvis in the MCR3 system software.

	Subvi Name	Function
System Setup	*MCR3 – EXT ChangeGlobals.vi*	Monitoring and/or changing the system configuration parameters.
	MCR3 – EXT TA – Setup.vi	Monitoring the TAT setup parameters and loading the contents into the TAT register for serial readout mode.
	MCRI – EXT TA – Setup.vi	Setting up the TAT parameters and changing the contents in the TAT register for single channel mode.
System Testing	*MCR3 – EXT AcquirePedestals2.vi*	Measuring the baselines and noise levels of VAS and TAT channels.
	MCR3 – EXT– VA – Display.vi	Single VAS/TAT channel testing with monitoring of the pulse waveforms.
Data Acquisition	*MCR3 – EXT Acquire – StoreData2.vi*	Acquiring data in serial mode and saving the data into a binary or ASCII file.
	MCR3 – v2 Stream.vi	Acquiring data in serial mode and saving the data into a binary file.

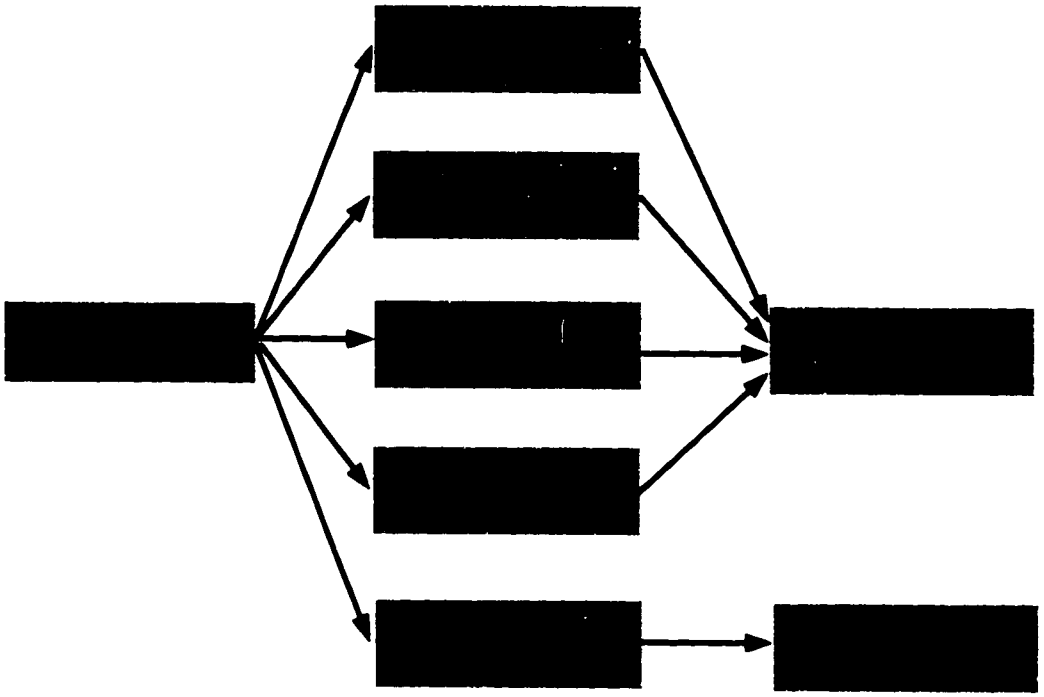

Figure 5.13: Hierarchy of the subvis in the MCR3 software.

5.2.4 Performance

The preamplifiers in the VAS readout channels of the MCR3 system are DC-coupled to the anode pixels. Similar to the first generation system, the resistance of the feedback resistor in each preamplifier needed to be reduced to accommodate the leakage current from the corresponding anode pixel, and caused the equivalent electronic noise to be increased to ~7 keV.

For the TAT channels in the MCR3 system, the dynamic range was measured to be 10 μs by changing the delay of the hold signal, the common stop signal for the TAC units in all the TAT channels. To estimate the timing resolution of the TAT channels, a test pulse, equivalent to 662 keV energy deposition in CdZnTe detectors, was concurrently injected into two individual channels. The TAT threshold was set equivalent to ~50 keV. The fluctuation of the difference of the TAT outputs from the

two channels was measured as 45.2 ns (FWHM), which should be the quadrature sum of the timing resolutions (FWHM) from those two channels. If the timing resolutions from the TAT channels are assumed to be the same, the timing resolution per channel is 32 ns (FWHM). This result is worse than that predicted in Chapter 3 ($\sim$10 ns FWHM), and it may be due to noise in the test pulse and/or the TAT threshold. If it is due to noise in the TAT threshold, the poorer measured timing resolution indicates a poorer depth resolution of $\sim$0.6 mm FWHM (compared to $\sim$0.5 mm FWHM) for 662 keV full energy deposition events by measuring electron drift time.

CHAPTER VI

EXPERIMENTS PERFORMED AND DISCUSSION OF THE RESULTS

6.1 General Description

The experiments performed fall into four categories: (1) investigation of the two interaction depth sensing techniques, (2) improvement of the energy resolution from the single-pixel events using 3-D pulse height correction, (3) measurement of the non-uniformity of $(\mu\tau)_e$, and (4) reconstruction of the energy spectrum from the two-pixel events. In this dissertation, when referring to energy, the FWHM is synonymous with energy resolution since only 662 keV gamma rays are used.

Three 3-D CdZnTe detectors are used in the experiments, two of them are first generation detectors and the other is a second generation detector. For convenience, the first generation detectors will be denoted as detectors 1.1 and 1.2, and the second generation detector will be denoted as detector 2.1. Each of detectors 1.1 and 1.2 has fairly good connections between the 11×11 anode pixels and the substrate using wirebonding. Among the 121 desired connections, detectors 1.1 and 1.2 have two and four bad connections respectively. As introduced in Chapter 4, the technique of plate-through-via is used in the second generation 3-D CdZnTe detectors to make more rigid connections between the anode pixels and the substrate. However, its

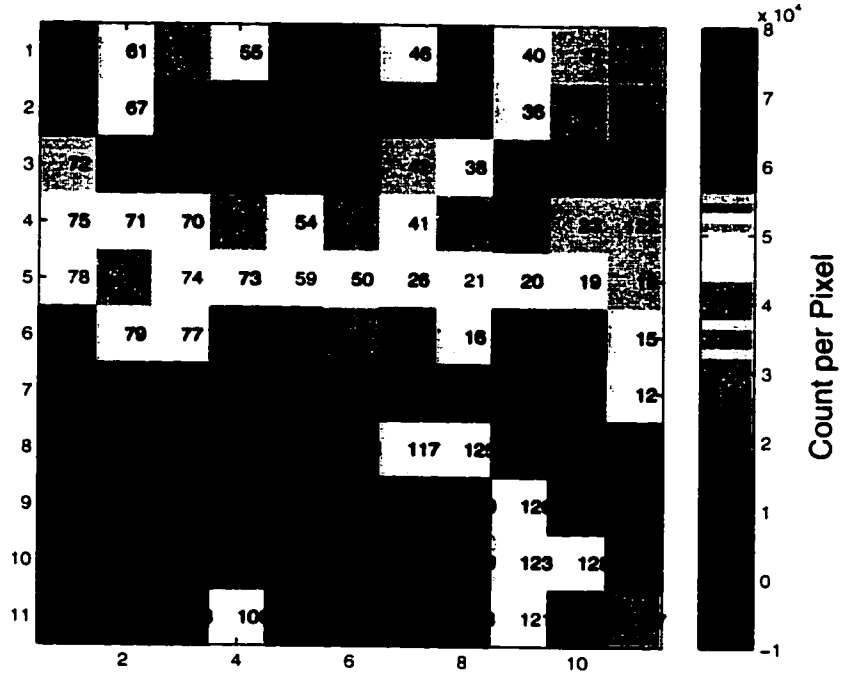

Figure 6.1: Distribution of the 662 keV signal counts from the anode pixels of detector 2.1. The number on each anode pixel indicates the corresponding readout channel.

implementation on detector 2.1 was not very successful. After detector 2.1 is biased and irradiated by gamma rays, about half of the anode pixels did not yield a signal. The distribution of the signal counts at different pixels from 662 keV gamma rays is shown in figure 6.1. For the bad pixels, the corresponding electronic readout channels were tested and worked well with the test pulses, so the problem is likely due to bad connections between the substrate and the detector. Since this was not a problem that could be solved inhouse, the experiments of detector 2.1 were limited to the subset of working anode pixels.

In all of the experiments, a high cathode bias ($\geq$2000 V) is desired to keep the maximum electron trapping across the detector below $\sim$10%. In practice, the actual cathode bias applied to the detector is limited by the amplitude and stability

of the leakage current. Specifically, the highest cathode bias of detectors 1.1 and 1.2 is limited by the leakage current saturating the VA1 chip, and was -2400 V (detector 1.1) and -1400 V (detector 1.2) respectively. The highest cathode bias of detector 2.1 is around -1400 V, and limited by the performance of the cathode signal. With a cathode bias above -1400 V, the fluctuation in the output of the cathode preamplifier was unusually high, which significantly degraded the signal-to-noise ratio of the cathode signal. This is likely due to material defects in the detector, which generate unstable leakage currents when the intensity of the electric field in the detector goes above a certain threshold.

The bias applied to the anode grid is also critical to the operation of the 3-D CdZnTe detectors. The grid bias should be high enough to focus the collection of all the radiation-generated electrons to the anode pixels. Otherwise the electrons in the region near the grid will move too slowly or even be collected by the grid, and consequently lead to pulse amplitude losses in the anode pixel signals. In detectors 1.1 and 1.2, this situation can be monitored using the pulse waveforms from the anode grid. If all the electrons are collected by the anode pixels, the signal from the grid should be transient or negative depending on the interaction depth (see figure 5.4). By this means, the grid bias was set to -50 V for detectors 1.1 and 1.2 since no obvious electron loss was observed. For detector 2.1, the output of the preamplifier connected to the grid was very noisy when the grid bias went above -10 V. This indicates an unstable leakage current at the anode surface. Ignoring the grid signal, the grid bias was increased to -90 V before the leakage current saturated the VAS channels. Thus, the grid bias of detector 2.1 was always set to -90 V in the experiments, unless otherwise mentioned.

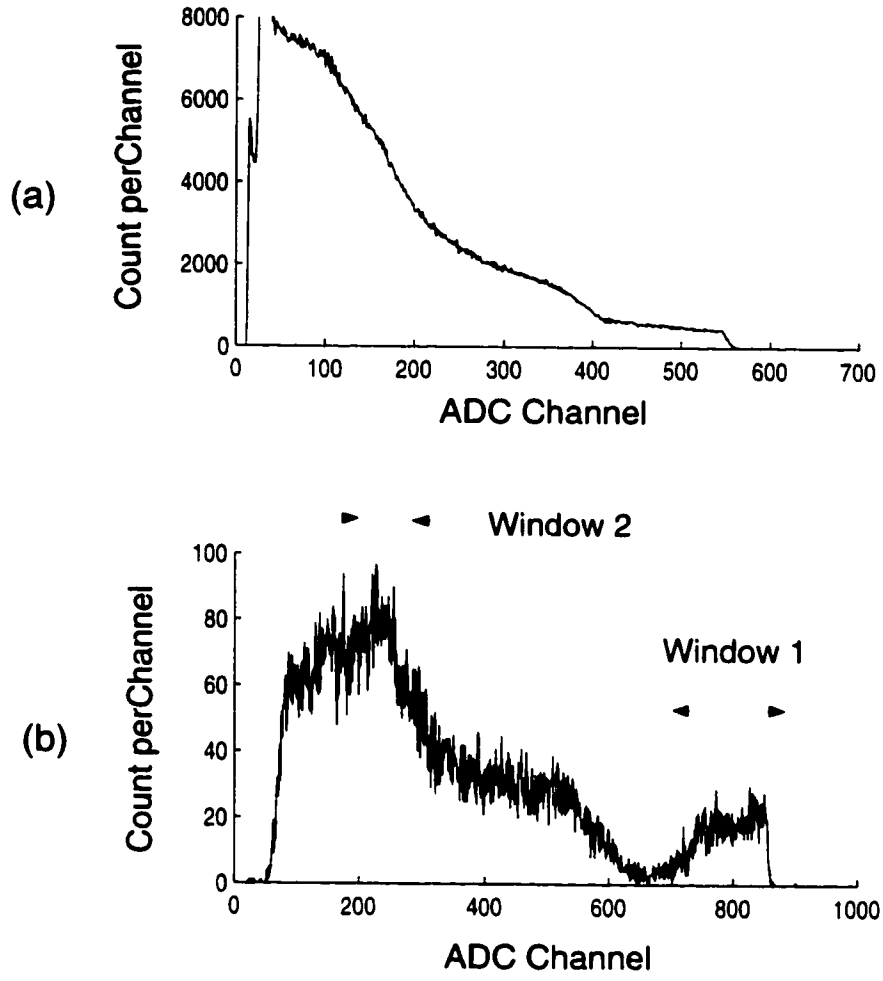

Figure 6.2: ^{137}Cs spectra of the single-pixel events from detector 2.1. (a) From the cathode. (b) From anode pixel #24.

6.2 Interaction Depth Sensing

According to the theoretical analyses and simulations in Chapters 2 and 3, the interaction depth of each single-pixel event in a 3-D CdZnTe detector can be determined by either the C/A ratio or the electron drift time. Because both depth sensing techniques are available with detector 2.1, experiments were performed using detector 2.1 to verify the effectiveness of these two techniques.

With the cathode bias of -1000 V and the grid bias of -90 V, detector 2.1 was irradiated by 662 keV gamma rays from the cathode side. The energy spectra of single-pixel events from the cathode and a typical anode pixel are shown in figure 6.2. Because the cathode is an electrode with conventional planar readout, the 662 keV energy spectrum from the cathode suffers from the trapping of both electrons and holes. Thus it shows no photopeak. In contrast, the energy spectrum from the anode pixel shows a clear photopeak from the single polarity charge sensing. However, the photopeak is severely broadened by the varying amounts of electron trapping coming from different interaction depths. To improve the energy resolution in the energy spectrum from each anode pixel, the interaction depth of each interaction event is read out and used to correct the pulse height for electron trapping. Therefore, interaction depth sensing is the cornerstone of the 3-D pulse height correction. Two experiments were performed to verify that the interaction depth of a single-pixel event can be determined by either the C/A ratio or the electron drift time. The first experiment was a measurement of the correlation between the two parameters. If both of the two depth parameters have a monotonic relationship with the true interaction depth shown in the simulation, they should demonstrate a strong correlation in the experiment. In the second experiment, a more direct verification was achieved using collimated gamma rays.

6.2.1 Correlation between C/A Ratio and Electron Drift Time

The C/A ratio and electron drift time are two parameters measured independently in the experiments. The correlation of these two parameters depends on their relationships with the interaction depth Z. Assume Z is proportional to each of these two parameters:

$$\begin{cases} Z = R + \delta_R \\ Z = T + \delta_T \end{cases} \tag{6.1}$$

where R and T are the measured C/A ratio and electron drift time after normalized to detector thickness. δ_R and δ_T are the errors in determining Z using R and T, respectively. Therefore, the depth resolutions by C/A ratio and by electron drift time are $(FWHM)_{\delta_R}$ and $(FWHM)_{\delta_T}$. Following equation 6.1, R and T should be related to each other as:

$$T = R + \delta_R - \delta_T \tag{6.2}$$

Hence T and R should have a linear correlation with the uncertainty of $\delta_R - \delta_T$. Because δ_R and δ_T are independent from each other, we should have:

$$(FWHM)^2_{\delta_R - \delta_T} = (FWHM)^2_{\delta_R} + (FWHM)^2_{\delta_T} \tag{6.3}$$

Therefore, assuming equation 6.1 is true, $(FWHM)^2_{\delta_R - \delta_T}$, which can be determined by measuring the correlation of R and T, is the quadrature sum of the depth resolutions by C/A ratio and by electron drift time. Because it is difficult to directly measure the depth resolutions, the relationship in equation 6.3 is useful in the estimation of the worst values of $(FWHM)_{\delta_R}$ and $(FWHM)_{\delta_T}$.

In the experiments, for each 662 keV photopeak event in energy window 1 shown in figure 6.2 (b), the C/A ratio and the electron drift time were measured simulta-

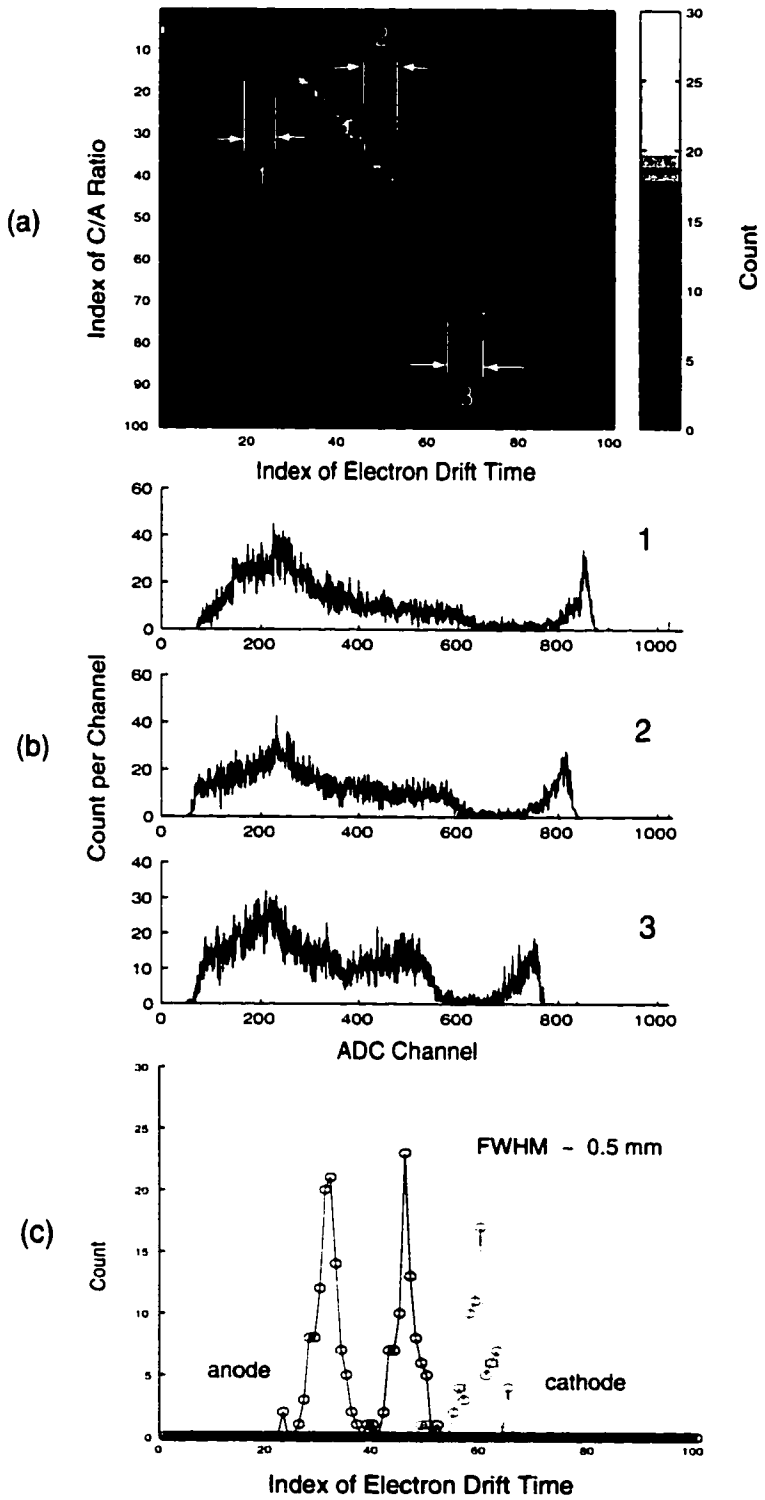

Figure 6.3: (a) Correlation between C/A ratio and electron drift time for the 662 keV single-pixel events in the energy window 1 shown in figure 6.2 (b). (b) Energy spectra from the three parameter windows shown in (a). (c) Profiles of the distribution in (a) with three different C/A ratio indexes.

neously. Each of the measured results was linearly transformed into a normalized depth index for convenience in the analysis. The measured correlation between the indexes for the C/A ratio and the electron drift time is shown in figure 6.3 (a), which demonstrates a nearly linear relationship between the two depth parameters and matches with expectation from equation 6.2. For those events lying in the three parameter windows shown in figure 6.3 (a), the corresponding energy spectra are shown in figure 6.3 (b). The photopeaks in the three spectra show much improved energy resolutions, which indicates each spectrum is associated with specific electron trapping hence from a specific interaction depth. The variation of the 662 keV photopeak centroids from the three spectra implies a different amount of electron trapping for the events originating from the three different interaction depths. This result clearly demonstrates that both the C/A ratio and the measured electron drift time have a monotonic relationship with the true interaction depth.

In addition, the profiles of the measured distribution in figure 6.3 (a) can be used to estimate the worst depth resolution for each of the two depth sensing techniques. Figure 6.3 (c) shows the three drift time profiles acquired using three different C/A ratios. The FWHM of the profiles is about 0.5 mm after being normalized to the detector thickness. Following equation 6.3, this result leads to:

$$(FWHM)^2_{\delta_R} + (FWHM)^2_{\delta_T} = 0.25mm^2, \tag{6.4}$$

Therefore, each depth resolution should be better than 0.5 mm in FWHM for 662 keV full energy deposition events. This result is consistent with the simulation results from Chapter 3 using similar electronic noise.

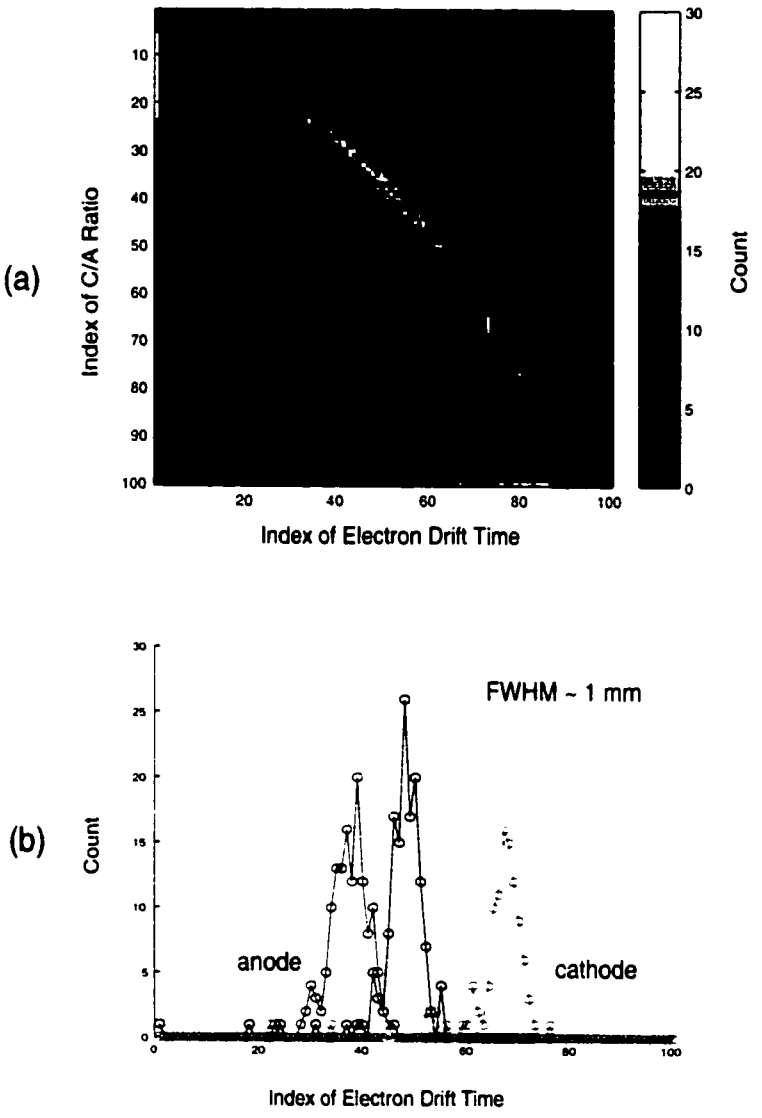

Figure 6.4: (a) Correlation between C/A ratio and electron drift time for the 662 keV single-pixel events in the energy window 2 shown in figure 6.2 (b). (b) Profiles of the distribution in (a) with three different C/A ratio indexes.

For the single-pixel events with lower energy depositions (~200 keV) from the energy window 2 in figure 6.2 (b), the measured correlation between the C/A ratio and the electron drift time is shown in figure 6.4 (a). The profiles shown in figure 6.4 (b) demonstrate a FWHM of ~1 mm, which indicates the depth resolutions of both techniques should be better than ~1 mm for ~200 keV energy deposition events.

With the above results regarding the depth resolutions, the number of the depth layers we choose to consider is set to 20 in the collection of 662 keV gamma spectrum. Each depth layer has an approximate thickness of 0.5 mm and corresponds to a depth index linearly transformed from the depth sensing parameter (C/A ratio or electron drift time).

6.2.2 Experiment Using Collimated Gamma Rays

The relationship between the true interaction depth and each depth sensing parameter can be verified directly using collimated gamma rays. The second generation detector system accommodates a gamma-ray collimator on one side of the 3-D detector, which makes this experiment possible using detector 2.1.

The experiment was set up as shown in figure 6.5 (a). The collimator is made of 1.5 cm lead, which provides a factor of ~7 of attenuation for the 662 keV gamma rays from a ^{137}Cs point source of ~1 mm in diameter. The collimator slit is ~0.4 mm wide and parallel to the lateral dimension of the detector. Since the 1.5 cm lead is not thick enough to block all the 662 keV gamma rays, background subtraction is needed to exclude the gamma rays transmitted through the 1.5 cm lead. The background was measured when the collimator slit was blocked with lead. With the collimator slit located at Z=~5.5 mm, the 662 keV energy spectrum from an anode pixel was collected and separated by both the C/A ratio and the electron drift time.

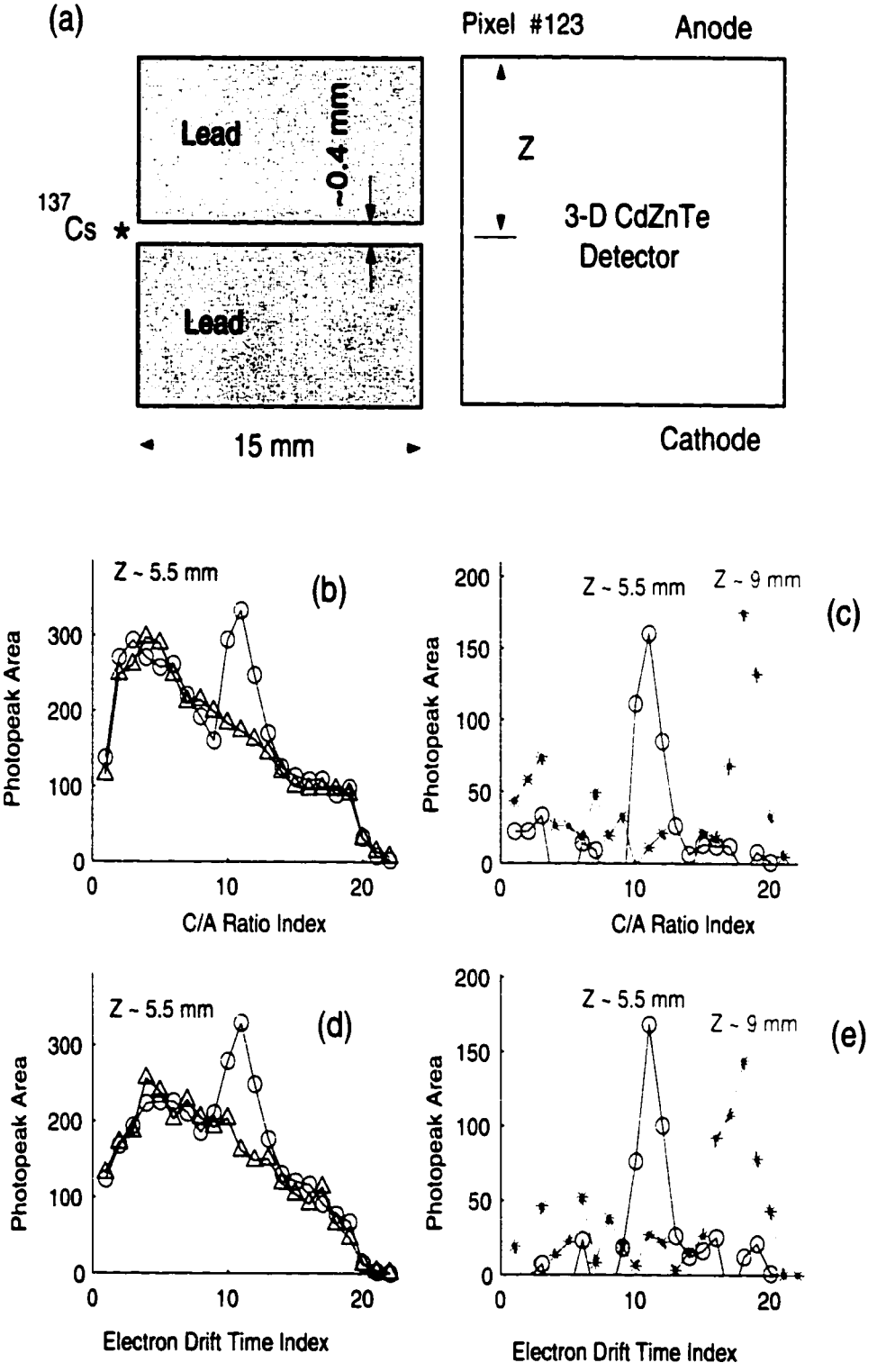

Figure 6.5: Experiment results from pixel # 123 with collimated 662 keV gamma rays. (a) Experiment setup. (b), (d) 662 keV photopeak area as a function of C/A ratio/electron drift time with the collimator slit open (circle) and closed (triangle). (c), (e) Net distributions after the subtractions, for two different Z, the position of the collimator slit.

Figure 6.5 (b) shows the 662 keV photopeak area as a function of the C/A ratio index, from the spectra collected with the collimator open and closed. Figure 6.5 (c) shows the net photopeak area after the subtraction, and with two different collimator slit locations (Z =~5.5, ~9 mm). The results indicate that each C/A ratio index corresponds to a distinct true interaction depth. The results using depth sensing by electron drift time are similar and shown in figure 6.5 (d) and (e). This experiment proves that the C/A ratio and the electron drift time have a monotonic relationship with the true interaction depth for single-pixel events.

6.3 3-D Pulse Height Correction for Single-Pixel Events

In this section, the 3-D pulse height correction for the single-pixel events and the energy resolution for the ^{137}Cs spectra from the three detectors are presented and discussed.

6.3.1 Calibration and the Spectrum from a Pixel

As introduced in Chapter 2, the first step in the 3-D pulse height correction in a 3-D CdZnTe detector is to calibrate the correction coefficients f_{ijk}. For detectors 1.1 and 1.2, these calibrations are done with interaction depth sensing by C/A ratio. During the long calibration runs, the temperature effect of the VA1 chip (described in Chapter 5) changed the overall detector response and degraded the energy resolution. To compensate for this effect, a peak-based spectrum stabilization technique was implemented using the spectrum derived from the entire detector volume.

Figure 6.6 shows the calibration spectra from a typical pixel (pixel #6) of detector 1.1. The calibration was measured in ~60 hours with a cathode bias of -2000 V. Except for the spectra from the nonlinear region near the anode, the photopeak area exceeds 1000 counts for each spectrum and the uncertainty in photopeak centroid

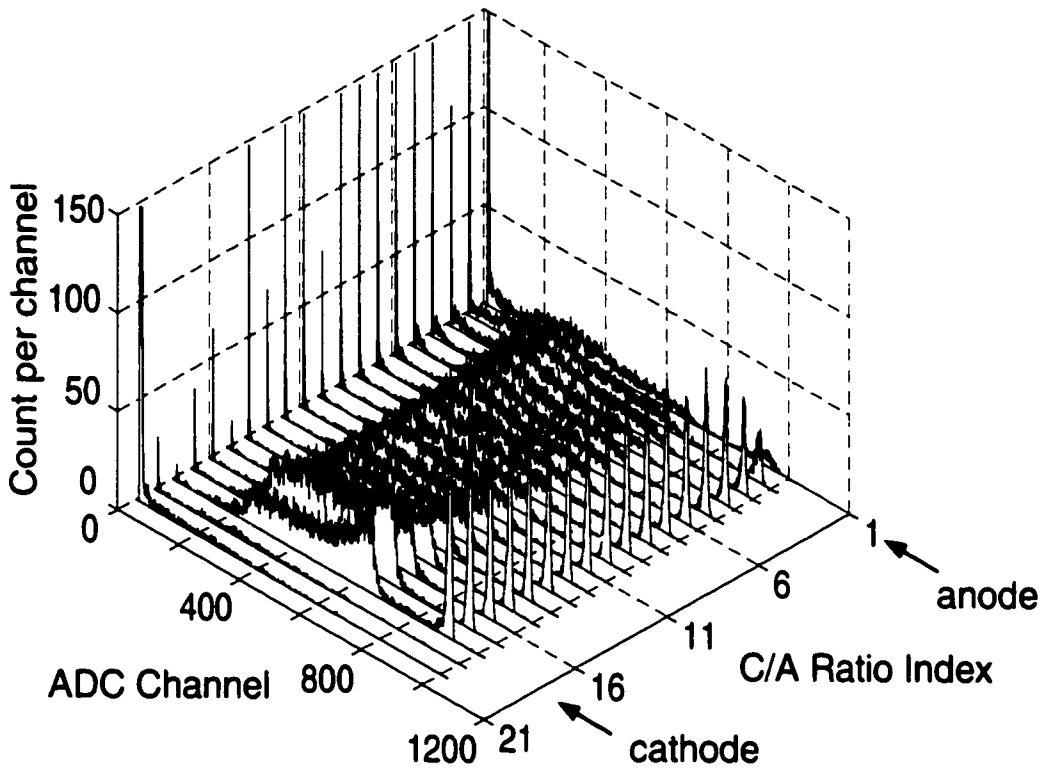

Figure 6.6: ^{137}Cs spectra of single-pixel events from pixel #6 of detector 1.1.

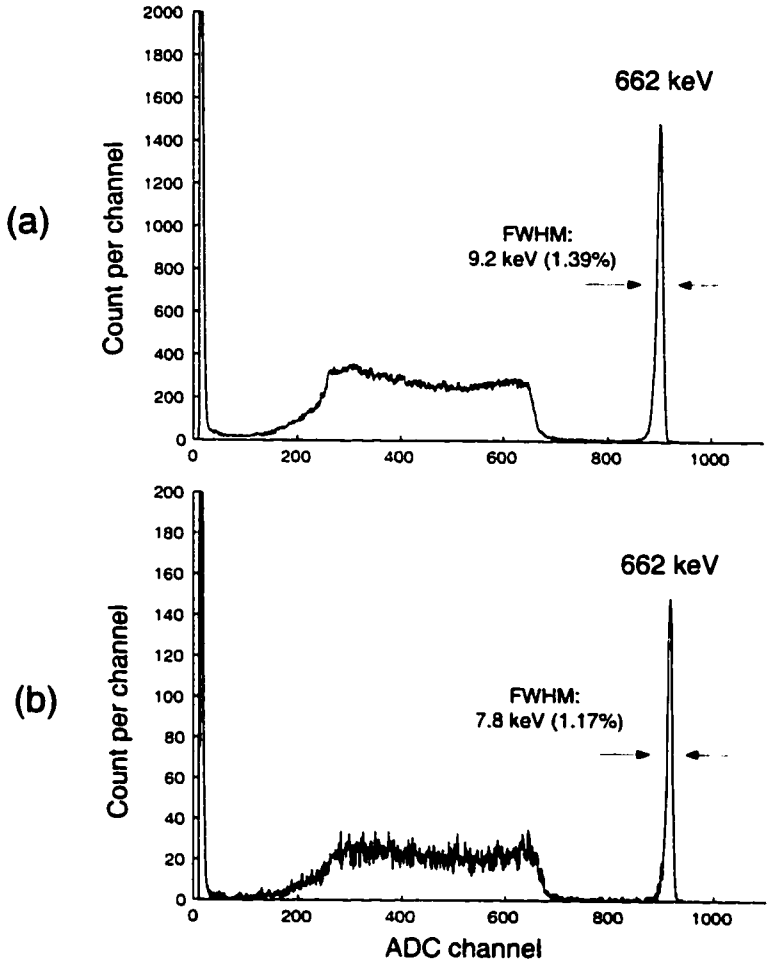

Figure 6.7: ^{137}Cs combined spectrum of single-pixel events from pixel #6 of detector 1.1 after non-uniformity correction along the depth. (a) Self-calibrated (~60 hours). (b) ~6 hours.

location is smaller than 0.1%(FWHM). Using the f_{ijk} derived from this calibration, all the spectra from this pixel were combined to yield the spectrum shown in figure 6.7 (a). Another set of spectra was collected over ~6 hours from detector 1.1 with less variation in the ambient temperature. The combined spectrum from pixel #6 using the same f_{ijk} values is shown in figure 6.7 (b). Comparing the energy resolutions of the two combined spectra, we can see that the degradation in the energy resolution from temperature changes is noticeable even with spectrum stabilization.

For detector 2.1, different calibrations were measured simultaneously with depth sensing by C/A ratio and by electron drift time. The calibration time needed was shorter to reach the same statistics as that in detectors 1.1 and 1.2 because of the larger effective volume of each voxel due to the larger pixel size. Using calibration factors measured over ~16 hours with depth sensing by C/A ratio, the combined spectrum from 662 keV single-pixel events collected during ~8 hours from a typical pixel (pixel #24) is shown in figure 6.8 (a). In addition, the spectrum combined with depth calibration using electron drift time is shown in figure 6.8 (b). The results show that the depth calibration using the C/A ratio yields better energy resolution than the depth calibration using the electron drift time. This difference is typical for the normal pixels, and is due to the better depth resolution of the C/A ratio, as demonstrated in the simulations in Chapter 3.

6.3.2 Variation of FWHM in Lateral Dimension

Using a set of spectra collected over ~6 hours from detector 1.1, the spectra from each pixel were combined using the calibration factors f_{ijk} previously measured over ~60 hours. The histogram and lateral distribution of the FWHM from each pixel are shown in figure 6.9 for detector 1.1 and figure 6.10 for detector 1.2. Significant

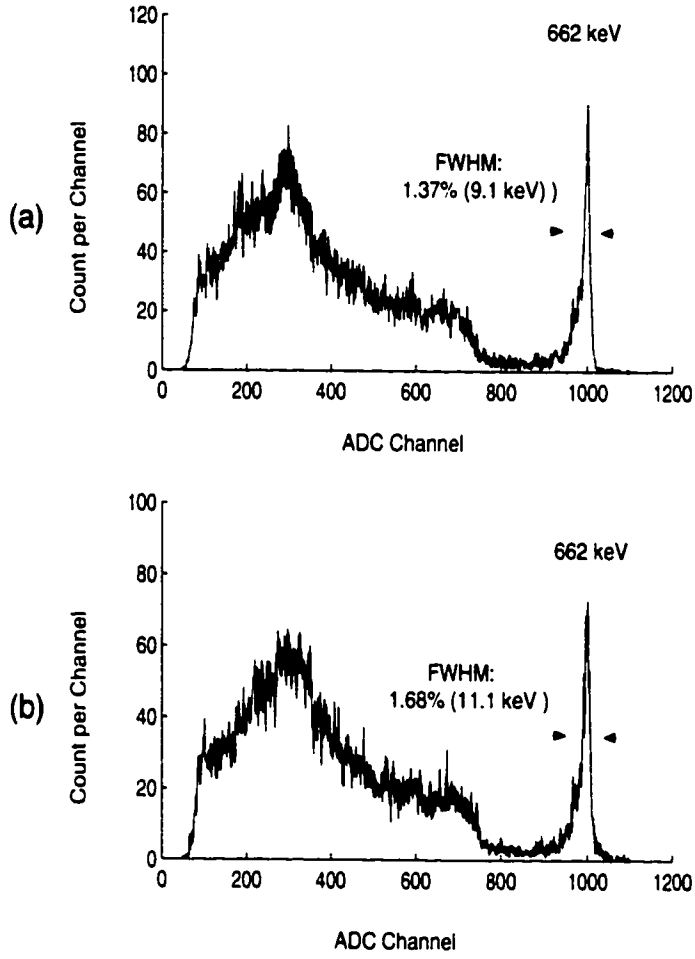

Figure 6.8: ^{137}Cs combined spectrum of single-pixel events from pixel #24 of detector 2.1 after non-uniformity correction along the depth. (a) Depth sensing by C/A ratio. (b) Depth sensing by electron drift time.

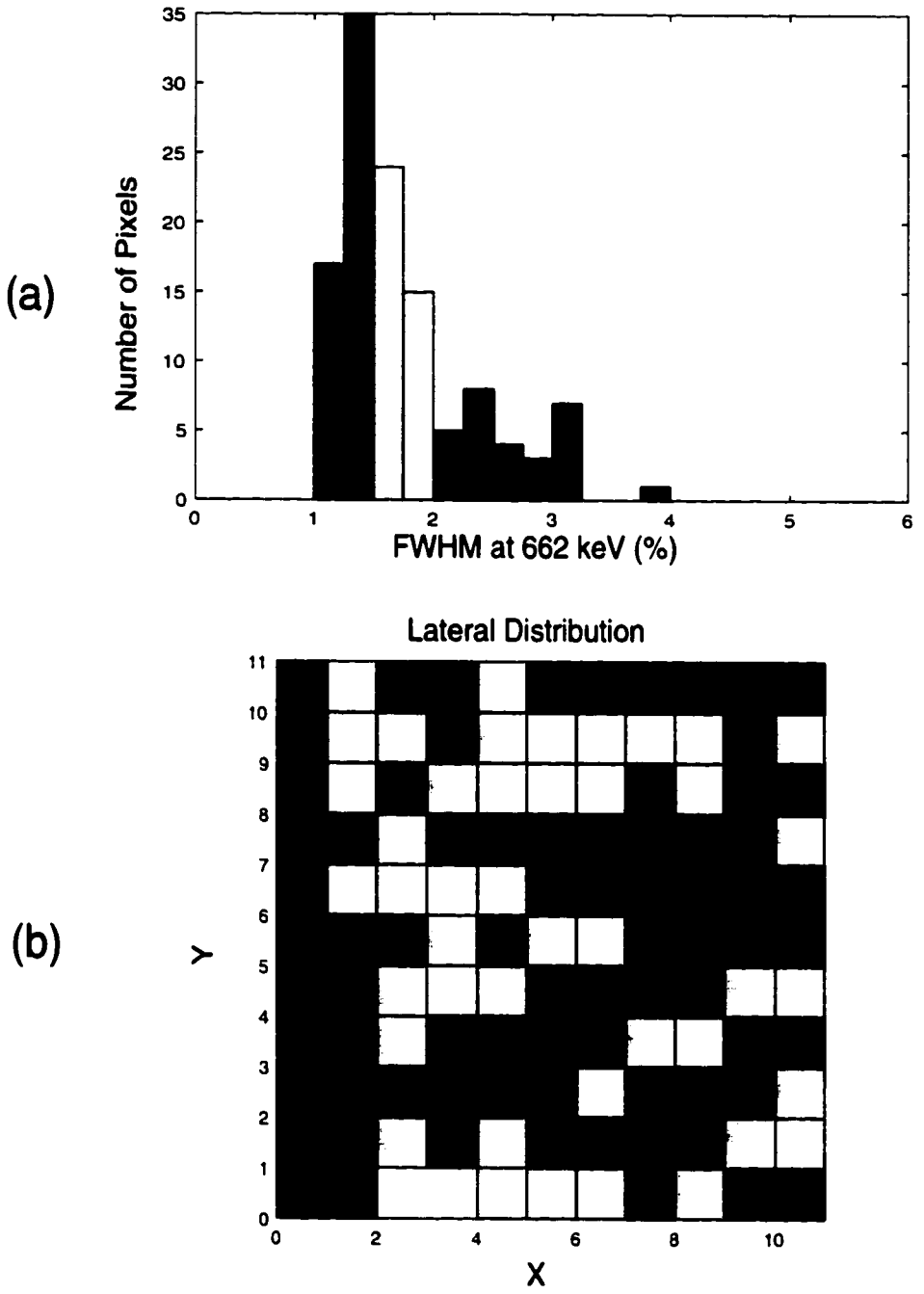

Figure 6.9: Pixel-based distribution of FWHM at 662 keV for single-pixel events from detector 1.1. (a) Histogram. (b) Lateral distribution.

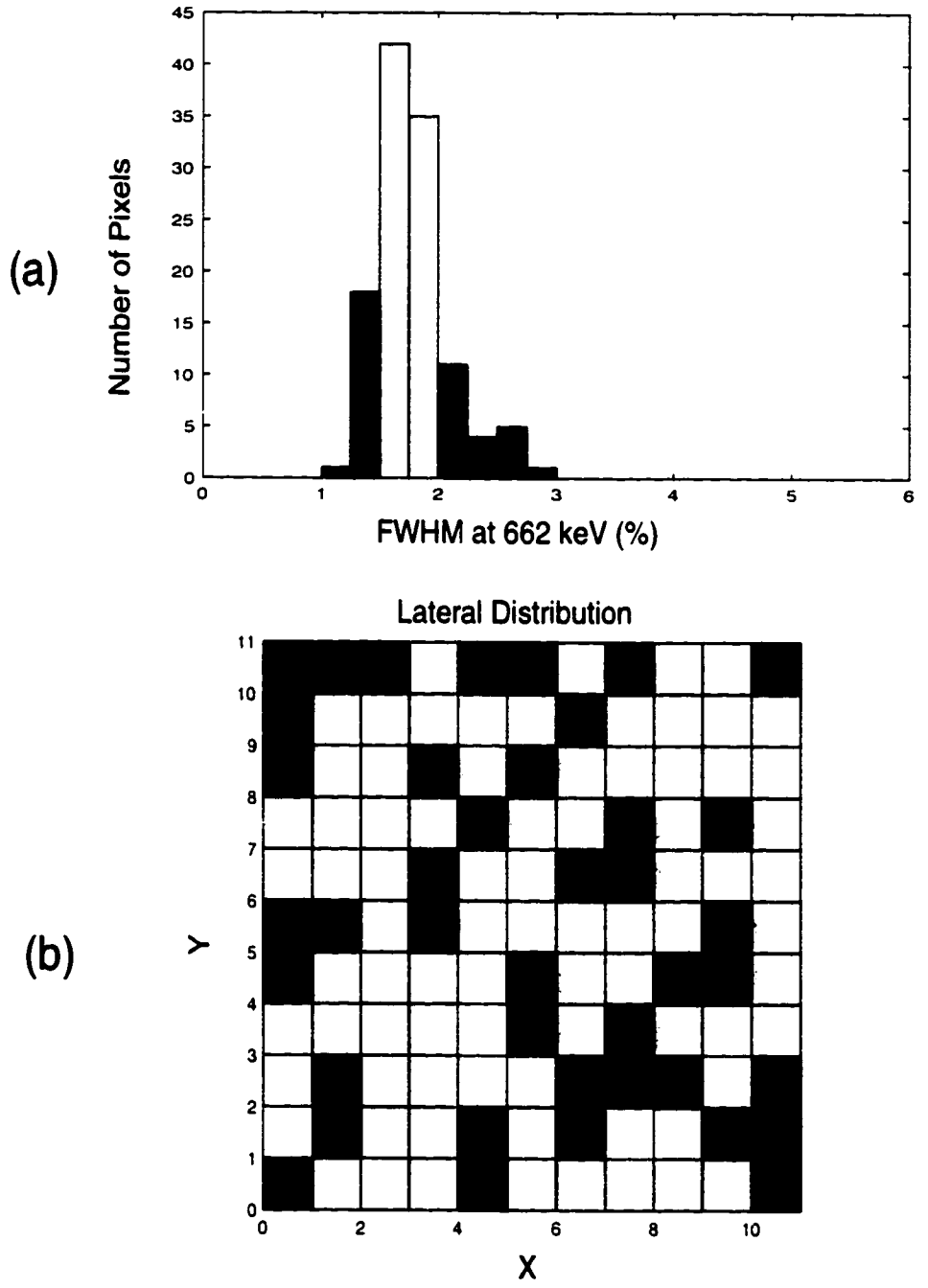

Figure 6.10: Pixel-based distribution of FWHM at 662 keV for single-pixel events from detector 1.2. (a) Histogram. (b) Lateral distribution.

degradations of energy resolution are observed primarily in peripheral pixels. The electronic noise of each VA1 channel was measured, and the energy resolution after the subtraction of electronic noise was calculated for each pixel. The relative variation of the results (not shown) was quite similar to that in figure 6.9, which implies that the cause of the energy resolution variation is from the detector rather than the electronics.

For the peripheral pixels, the degradation of energy resolution can be explained by the gap ($\sim$1 mm) between the peripheral anode pixels and the edge of CZT crystal. Electrons generated in this gap still can be collected at the nearest peripheral pixel (in fact, the photopeak count rates of the peripheral pixels are higher than that of the central pixels), but have a longer trajectory and drifting time, and hence poorer charge collection efficiency. In detector 1.1, the gap corresponding to the peripheral pixels with $x = 1$ or $y = 11$ is about 1.5 times as wide as that corresponding to the pixels with $x = 11$ or $y = 1$ (see figure 6.9 for x and y coordinates). This explains why the degradation of the energy resolution is less serious along the edges with $x = 11$ or $y = 1$.

For the detector 2.1, the variation in the energy resolutions from different pixels has also been observed. However, there is no obvious degradation of the energy resolution from the normal peripheral pixels, because the gap between the peripheral pixels and the detector edge in detector 2.1 is smaller ($\sim$0.2 mm) compared with that in detectors 1.1 and 1.2. Figure 6.11 shows the histograms of the energy resolutions from all the working pixels with the two different calibrations.

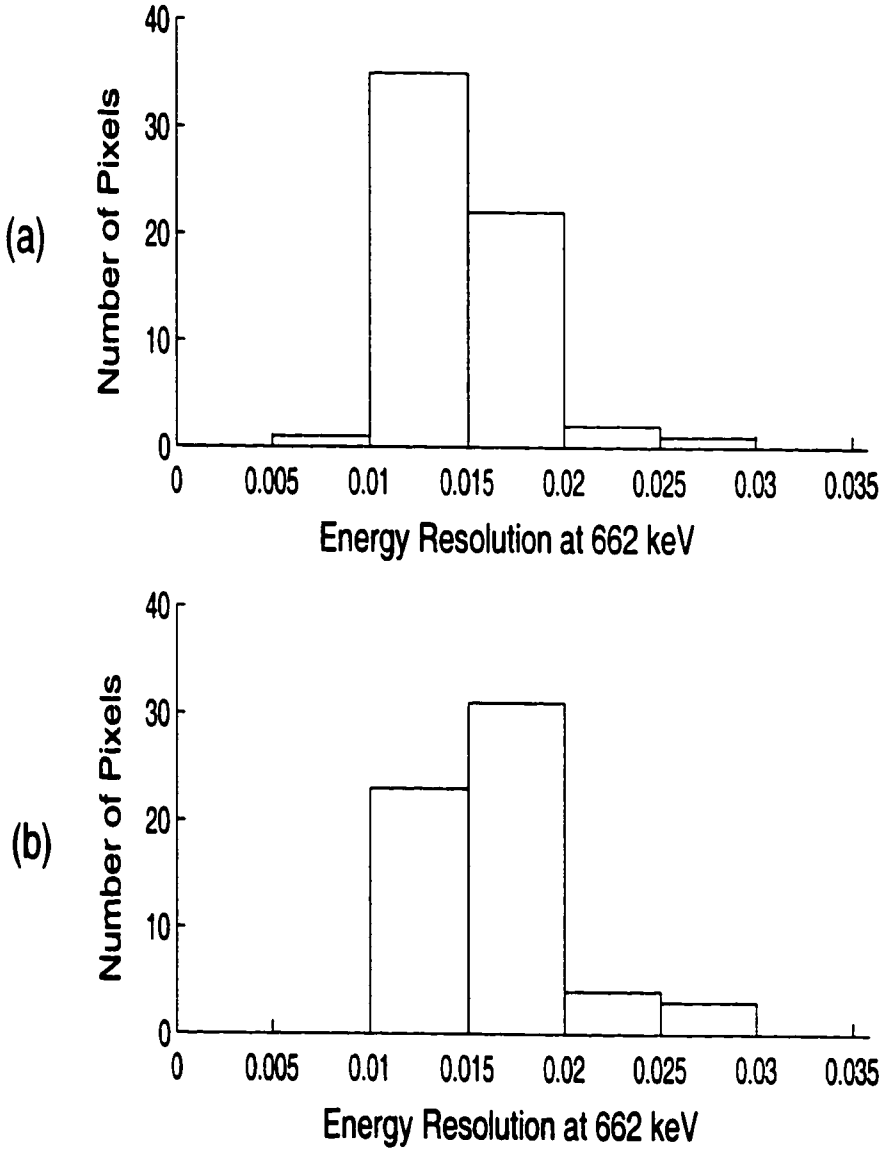

Figure 6.11: Histogram of energy resolution at 662 keV for single-pixel events from the working pixels in detector 2.1. (a) Depth sensing by C/A ratio. (b) Depth sensing by electron drift time.

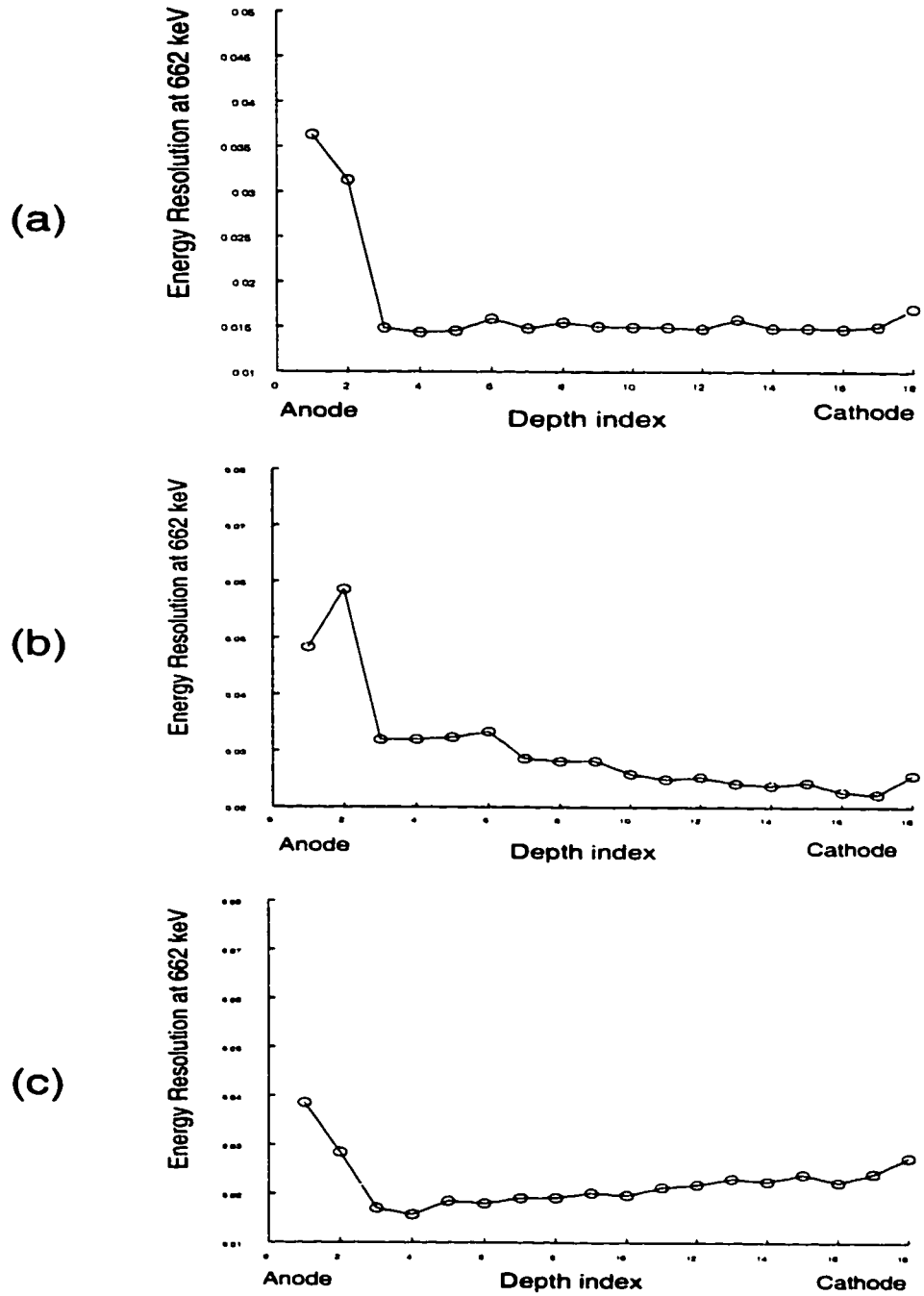

Figure 6.12: Voxel-based distribution of energy resolution at 662 keV from (a) pixel #6 (x=4, y=3), (b) pixel #101 (x=1, y=8), (c) pixel #106 (x=4, y=6) of detector 1.1, expressed as fraction of full energy.

6.3.3 Voxel-based Energy Resolution

The voxel-based energy resolution as a function of the interaction depth from a normal central (non-peripheral) pixel, pixel #6, of detector 1.1 is shown in figure 6.12 (a). For normal central pixels, uniform energy resolution can be achieved from different interaction depths except for the region near the anode. This indicates the non-uniformity of electron trapping on the scale of the voxel is small and has no considerable contribution to the energy resolution.

Figure 6.12 (b) shows the voxel-based distribution of energy resolution from a typical peripheral pixel (x=1, y=8) of detector 1.1, and the corresponding spectra are shown in figure 6.13 (b). The energy resolution in the peripheral pixels is degraded by the events from the gap between the pixel and the edge of CZT crystal. The decreasing FWHM for events further from the anode implies the decreasing difficulty for the electrons in the gap to move in the lateral dimension and be collected. This is probably because the detector has a smaller anode (7.7×7.7 mm^2) than the cathode (10×10 mm^2).

In contrast to the normal central and peripheral pixels, those central pixels having poor energy resolutions have a monotonically increasing FWHM along the depth from the anode to the cathode. This is the typical situation in all of the three detectors. Figure 6.12 (c) shows the distribution of the energy resolution from one of these pixels in detector 1.1, and the corresponding spectra are shown in figure 6.13 (a). The monotonic increase in FWHM from the anode to the cathode implies the existence of a defective region having an unusual non-uniformity in electron trapping. This will contaminate all the spectra from the volume between this region and the cathode. This situation can only be improved by choosing a better quality crystal from which to fabricate the detector.

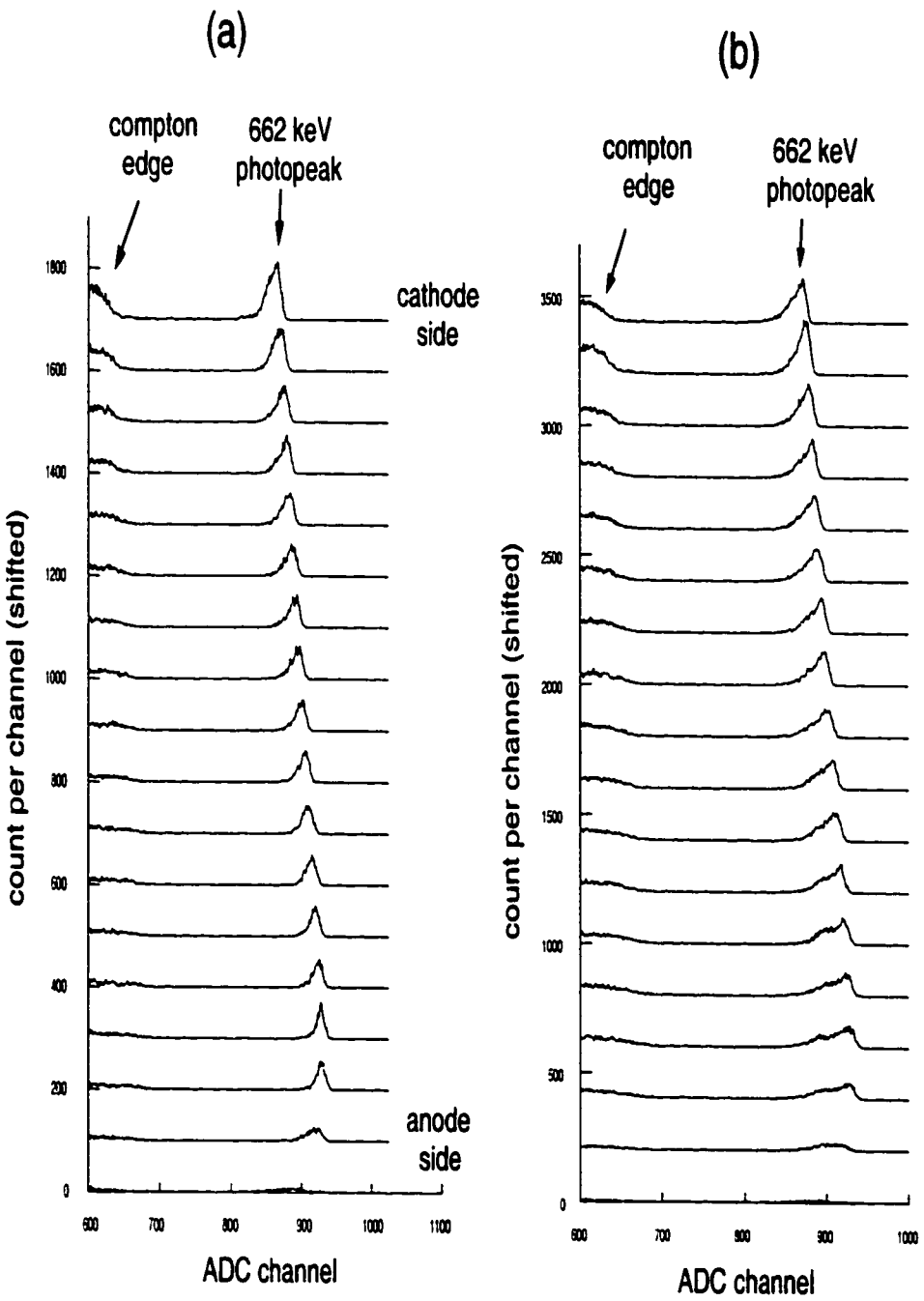

Figure 6.13: Photopeaks in voxel-based ^{137}Cs spectra of single-pixel events from (a) pixel #101 (x=1, y=8), (b) pixel #106 (x=4,y=6) of detector 1.1. From the upper to the lower: from the cathode to the anode.

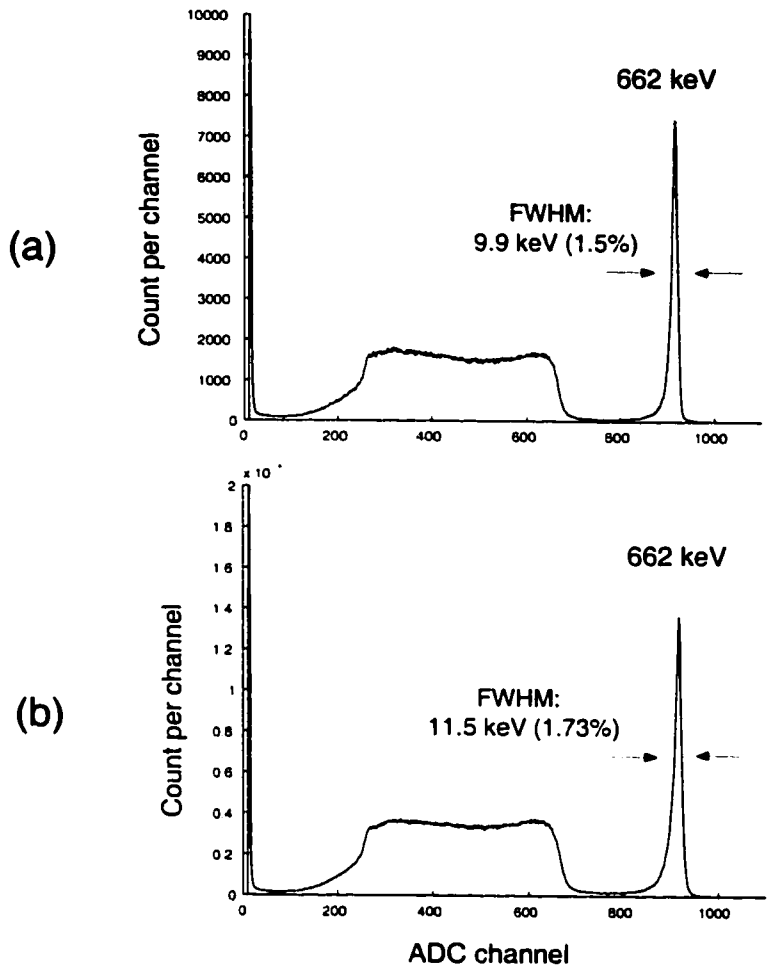

Figure 6.14: ^{137}Cs combined spectrum from single-pixel events in detector 1.1 after 3-D pulse height correction. (a) From the 9×9 central pixels. (b) From the whole bulk.

6.3.4 Energy Resolution from the Global Spectra

Figure 6.14 and 6.15 show the ^{137}Cs combined spectra from the 9×9 central pixels and the whole bulk of detectors 1.1 and 1.2. Compared with the FWHM of 7.8 keV (1.17%) from a normal pixel shown in figure 6.7 (b) of detector 1.1, the FWHM increases to 9.9 keV (1.5%) for the combined spectrum from the 9×9 central pixels, and further increases to 11.5 keV (1.73%) for the combined spectrum from the whole bulk of the detector. Figure 6.16 shows the ^{137}Cs combined spectra from the working

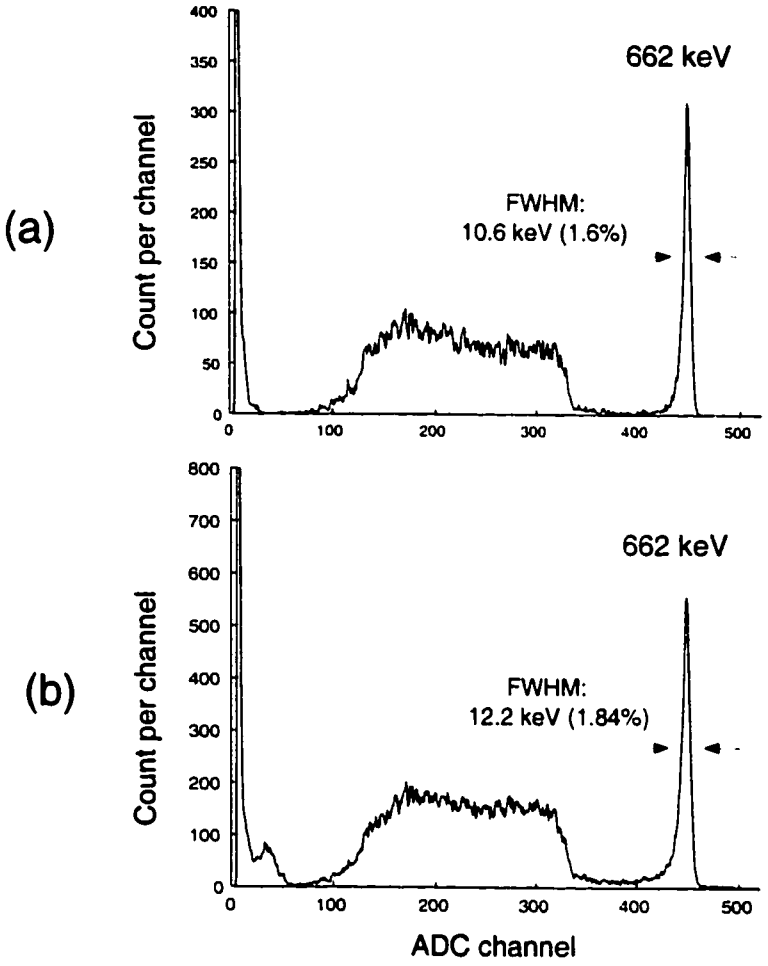

Figure 6.15: ^{137}Cs combined spectrum of single-pixel events from detector 1.2 after 3-D pulse height correction. (a) From the 9×9 central pixels. (b) From the whole bulk.

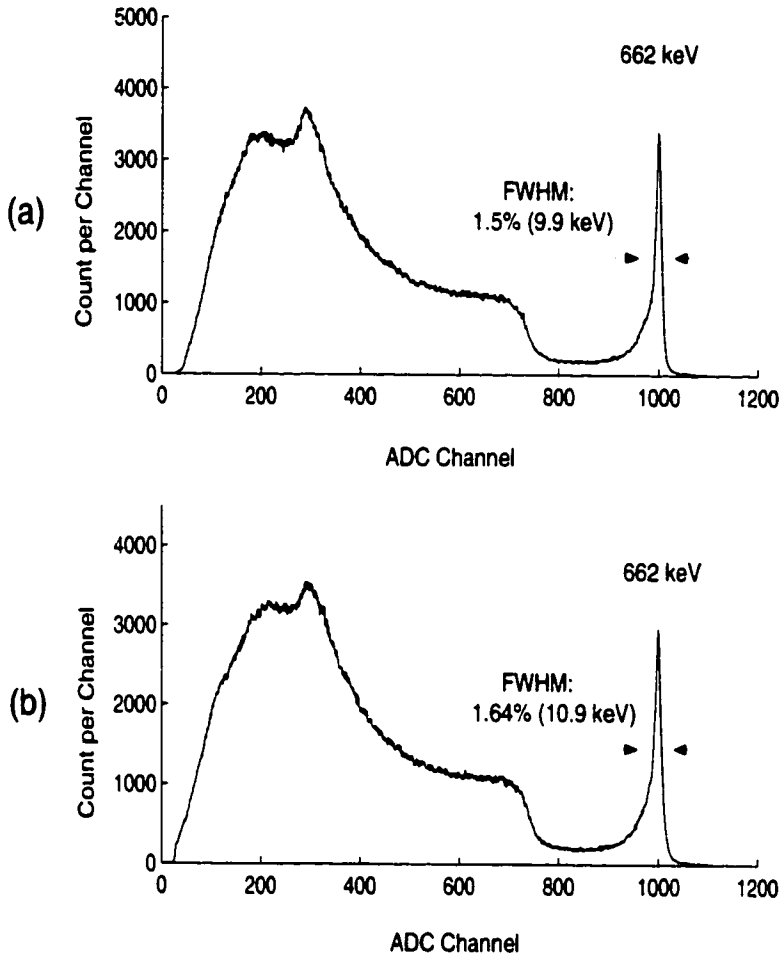

Figure 6.16: ^{137}Cs combined spectrum of single-pixel events from detector 2.1 after 3-D correction. (a) Depth sensing by C/A ratio. (b) Depth sensing by electron drift time.

pixels of the detector 2.1 with the two different depth sensing techniques.

The spatial variation of the energy resolution detailed above accounts for the degradation of the energy resolution from the combined global spectra. However, the unique 3-D position sensitivity provides the flexibility of identifying those voxels with poor energy resolutions in the calibration measurement, and then excluding their contributions from the overall spectrum in the measurements. As an example, excluding the contribution from the peripheral pixels in detectors 1.1 and 1.2 brings obvious improvement to the energy resolution of the combined spectrum.

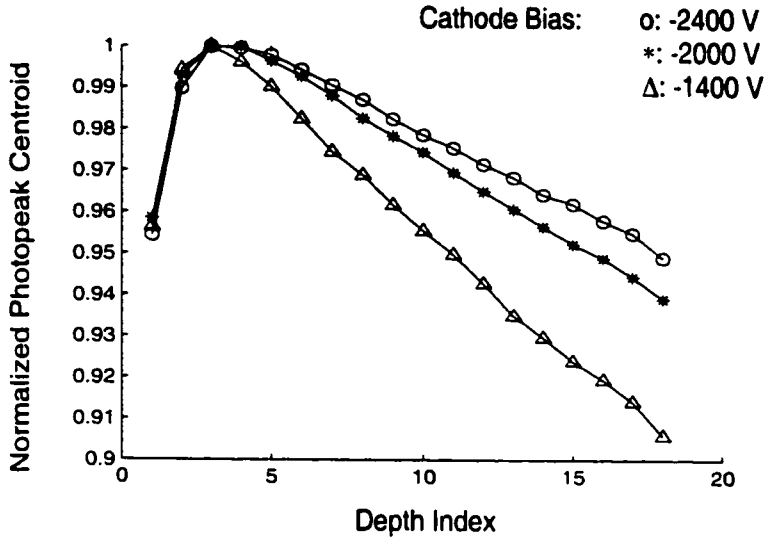

Figure 6.17: Variation of 662 keV photopeak centroid as function of C/A ratio. From pixel #6 of detector 1.1.

6.4 Measurement of the Electron Mobility-Lifetime Product

As introduced in Chapter 2, given the 662 keV energy spectrum of single-pixel events from an anode pixel, the variation of the photopeak centroid as a function of the interaction depth can be used to estimate the electron mobility-lifetime product, $(\mu\tau)_e$, for the material underneath the anode pixel. In this experiment, the position of the 662 keV photopeak centroid as a function of the C/A ratio was measured for pixel #6 of detector 1.1 at three different cathode biases, and the results are shown in figure 6.17. The photopeak centroid location decreases with the increasing interaction depth (represented by the C/A ratio) except in the region near the anode. This result matches well with the simulation result in figure 3.9 (a) for the normalized pulse height from the anode pixel.

The results shown in figure 6.17 (excluding the data from the layer of $\sim$1 mm thickness near the anode surface) were fitted using equation 2.24 to find $(\mu\tau)_e$. The interaction depth used in the fitting is assumed to be linear with the measured C/A

Table 6.1: Estimated $(\mu\tau)_e$ from the variation of 662 keV photopeak centroid shown in figure 6.17.

Cathode Bias (V)	$(\mu\tau)_e$ $(\times 10^{-3} cm^2/V)$	$\sigma_{(\mu\tau)_e}$ $(\times 10^{-3} cm^2/V)$
-2400	6.1	0.08
-2000	6.1	0.05
-1400	5.8	0.08

ratio index. The fitted results are shown in table 6.1. The estimated values of $(\mu\tau)_e$ at three different cathode biases are quite consistent with small fitting errors, and the values are within the normal range of $(\mu\tau)_e$ of the commercially available CdZnTe crystals (see table 1.1). Because the whole detector thickness is represented by ~20 C/A ratio indexes, the transformation from the C/A ratio index to the true interaction depth could have up to 5% round-off error from discretizing. This indicates the absolute values of the results in table 6.1 may have up to 5% systematic error. This error depends on the mapping of the C/A ratio index to the interaction depth, and it may be different from pixel to pixel.

Figure 6.18 shows the distribution of the measured $(\mu\tau)_e$ from the 9×9 central pixels of detector 1.1. The relative standard deviation in the measured $(\mu\tau)_e$ from the different pixels is ~10%, which is significantly larger than the measurement error (up to 5%). Therefore, the variation in the measured $(\mu\tau)_e$ from different pixels is likely due to the non-uniformity of the detector material in the lateral dimension.

In detector 2.1, $(\mu\tau)_e$ can be measured with depth sensing by C/A ratio or by electron drift time. Figure 6.19 (a) shows the variation of 662 keV photopeak centroid as function of the C/A ratio/electron drift time indexes from a normal pixel (pixel

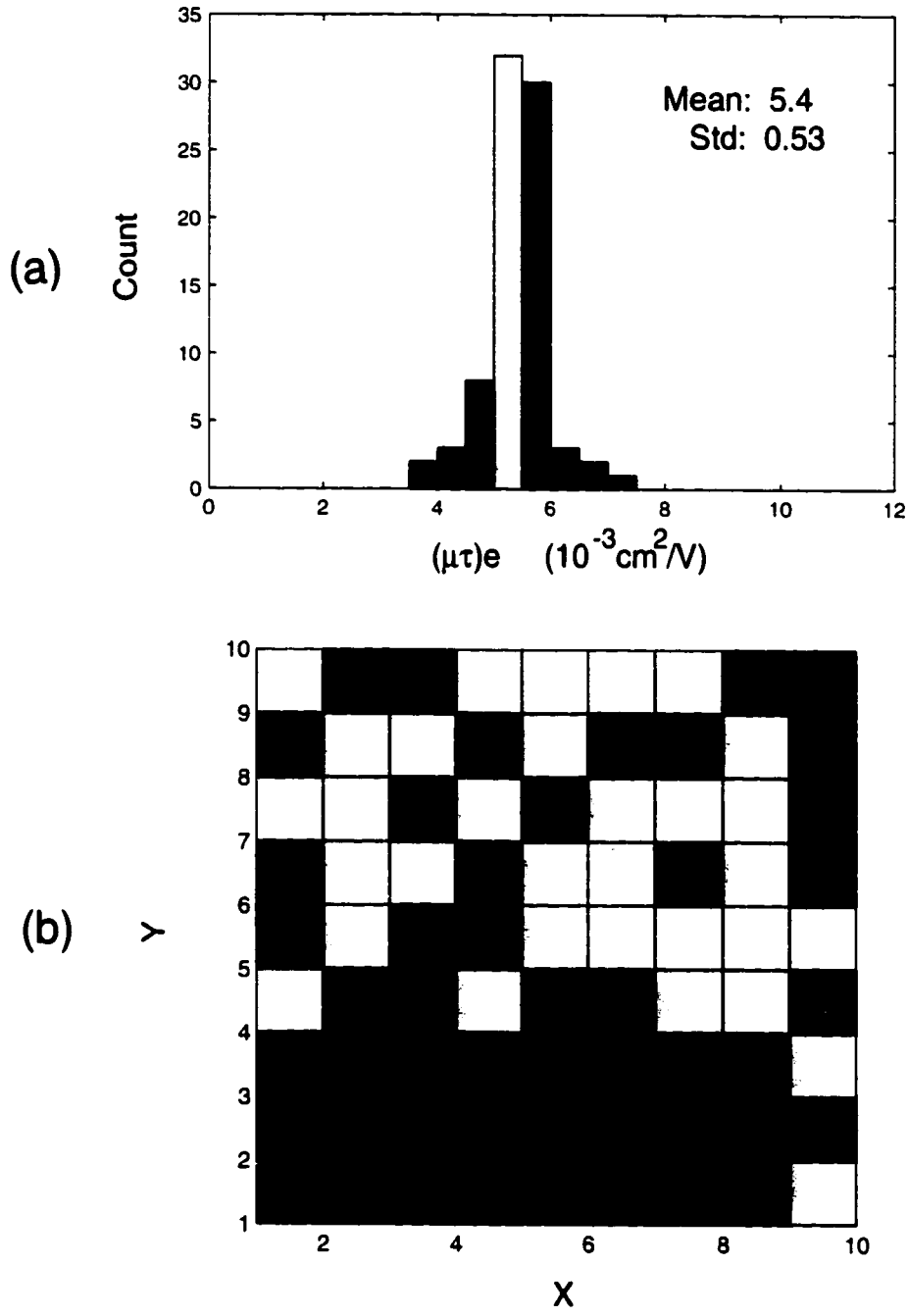

Figure 6.18: Distribution of the measured $(\mu\tau)_e$ from the 9×9 central pixels of detector 1.1. (a) Histogram. (b) Lateral distribution.

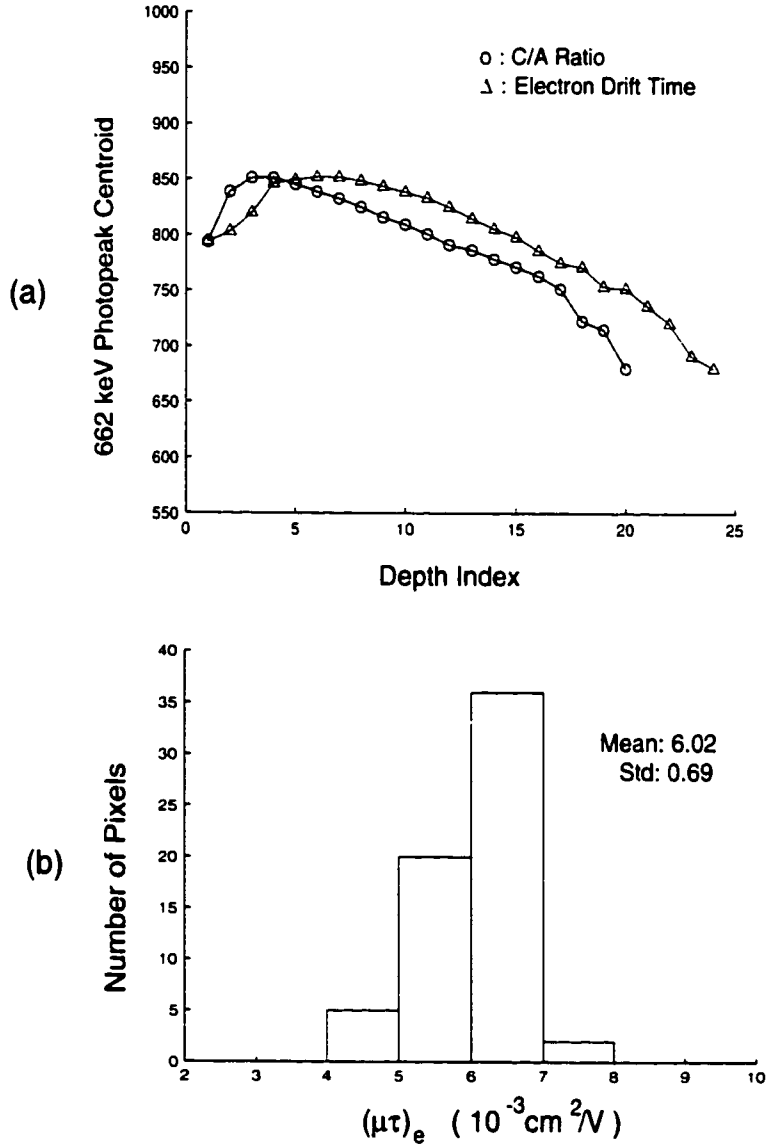

Figure 6.19: Measurement of $(\mu\tau)_e$ for detector 2.1. (a) 662 keV photopeak centroid as function of C/A ratio/electron drift time from pixel #24. (b) Histogram of the measured $(\mu\tau)_e$ from the working pixels.

#24). The results are similar to those acquired from detector 1.1, and are typical for the other working pixels. Using the same fitting method to determine $(\mu\tau)_e$, the histogram of the measured $(\mu\tau)_e$ from the working pixels is shown in figure 6.19 (b). The variation in the measured $(\mu\tau)_e$ from different pixels is also similar to the result from detector 1.1, indicating no significant difference in the CdZnTe materials of the two detectors.

The variation in the measured $(\mu\tau)_e$ from different pixels indicates the non-uniform electron trapping in the lateral dimension. This verifies the necessity of pulse height correction in the lateral dimension, which is uniquely offered by the 3-D CdZnTe detectors. For example, in a detector with ~10% electron trapping for the events near the cathode, a relative variation of ~10% in the $(\mu\tau)_e$ from different pixels implies a ~1% relative variation in the pulse heights (due to non-uniform electron trapping) from different anode pixels for the same energy deposition near the cathode. This variation can be corrected using 3-D pulse height correction in the 3-D CdZnTe detectors, otherwise it will degrade the energy resolution of the detector.

6.5 Multiple-Pixel Events

In the previous sections of this chapter, the results from the 662 keV single-pixel events were presented and discussed. However, a large fraction of the 662 keV gamma interactions in the 3-D CdZnTe detectors yield multiple-pixel events. In the application using the 3-D CdZnTe detectors as gamma-ray spectrometers, reconstruction of the total energy deposition in the detector for the multiple-pixel events is critical to improve the detection efficiency.

6.5.1 Fractions of Multiple-Pixel Events

In detectors 1.1 and 1.2 which use depth sensing by C/A ratio, it's impossible to determine the multiple interaction depths of the multiple-pixel events and accurately reconstruct the total energy depositions in the detector. However, the fraction of multiple-pixel events as a function of the number of the pixels involved can be recorded in an experiment and compared to the simulation results. Figure 6.20 (a) shows the measured fraction of the multiple-pixel events with 662 keV full energy depositions in detector 1.1. For two-pixel full energy deposition events, the measured distribution of the distance between the two pixels is shown in figure 6.20 (b). In addition, figure 6.20 (c) and (d) show how the signal is shared between the two pixels if they are adjacent to each other or separated by another pixel. These results are seen to match well with the simulation results in figure 3.4, which clearly demonstrate that our understanding of the generation of the multiple-pixel events is correct.

For the 662 keV full energy deposition events in detector 2.1, the measured fraction of the multiple-pixel events as a function of the number of the pixels involved is shown in figure 6.21 (a). This result doesn't match the simulation result (shown in figure 3.5) in the fraction of the single-pixel events, because detector 2.1 suffers from bad connections between the detector and the substrate. Thus only about half of the pixels yield signals from the detector. For the two-pixel full energy deposition events, the energy spectrum from one of the two pixels is shown in figure 6.21 (b). The features of the spectrum resemble that from a normal detector (like the one in figure 6.20 (c)), which indicates the two-pixel events in detector 2.1 are still generated from the same mechanism, and thus can be used to investigate the reconstruction of the energy spectrum from the two-pixel events.

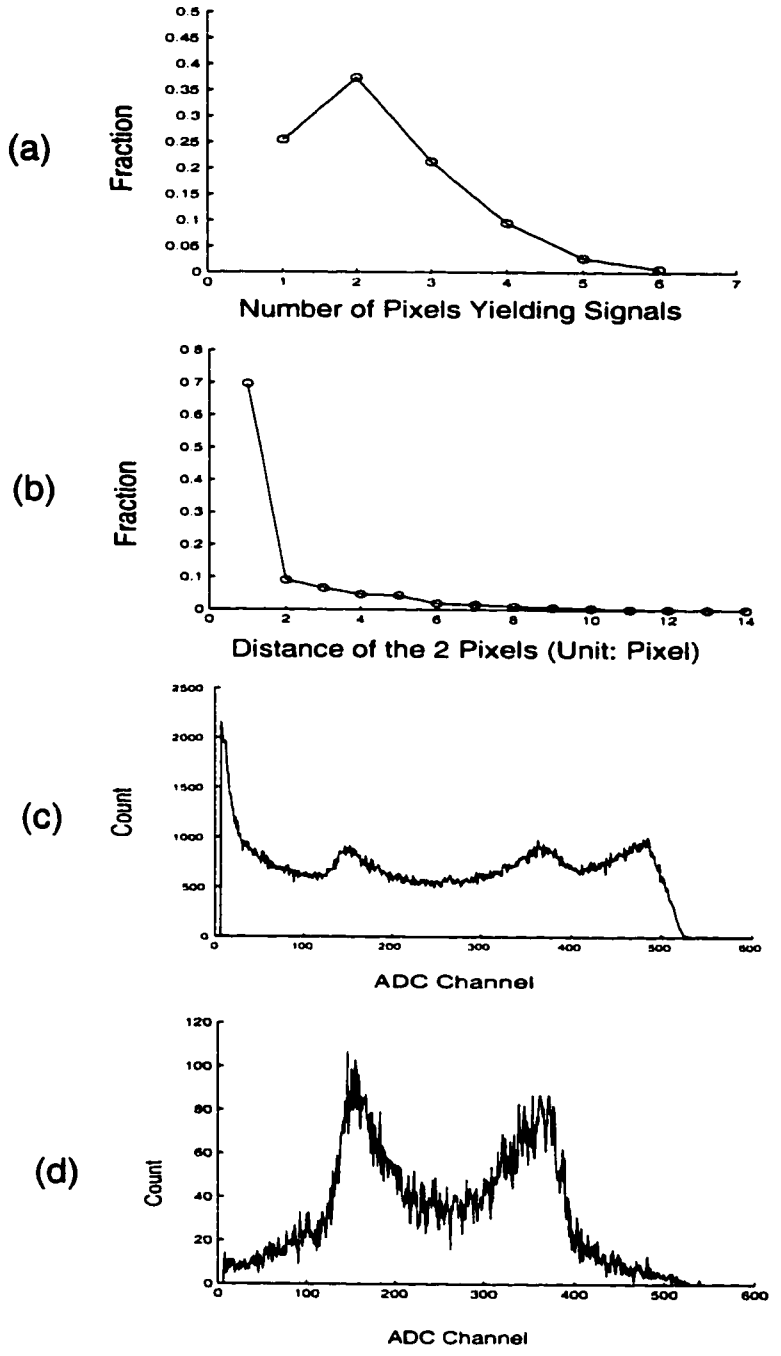

Figure 6.20: Results of the 662 keV multiple-pixel events in detector 1.1. (a) Fraction of the total events as a function of the number of pixels involved. (b) For two-pixel events: the distribution of the distance between the two pixels. (c) The energy spectrum from one pixel in two-adjacent-pixel events. (d) The energy spectrum from one pixel in two-pixel events with the two pixels separated by another pixel.

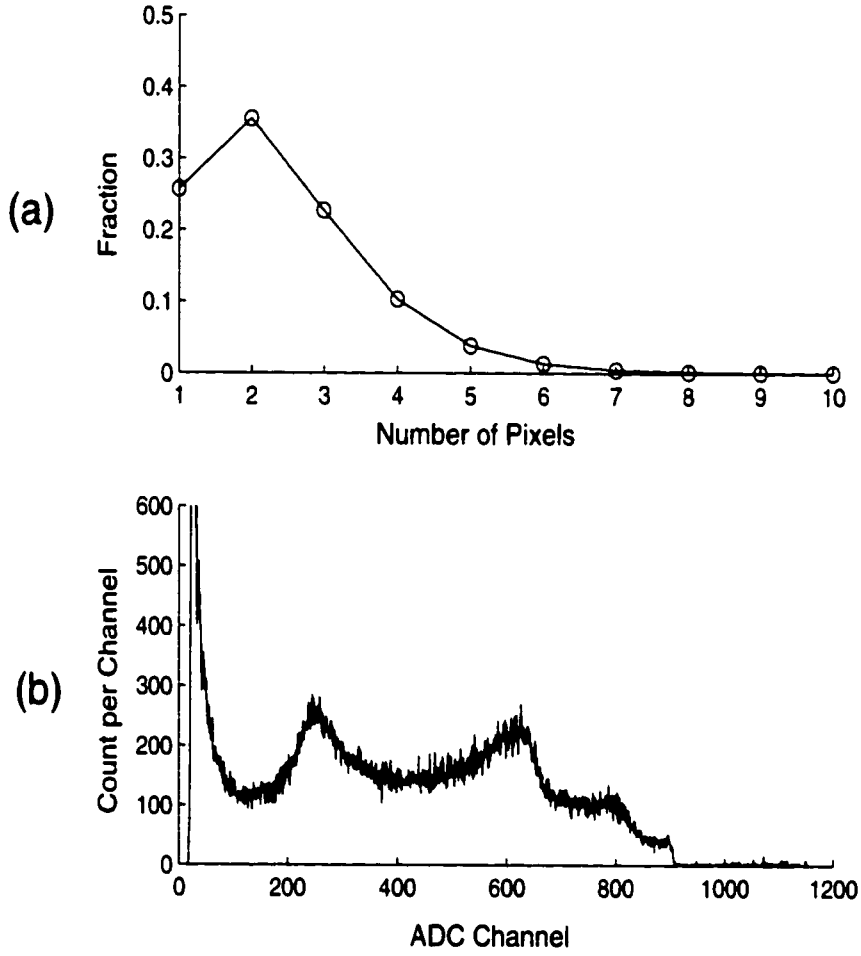

Figure 6.21: (a) Fraction of 662 keV multiple-pixel full energy deposition events in detector 2.1. (b) Energy spectrum from one of the pixels in the 662 keV two-pixel full energy deposition events.

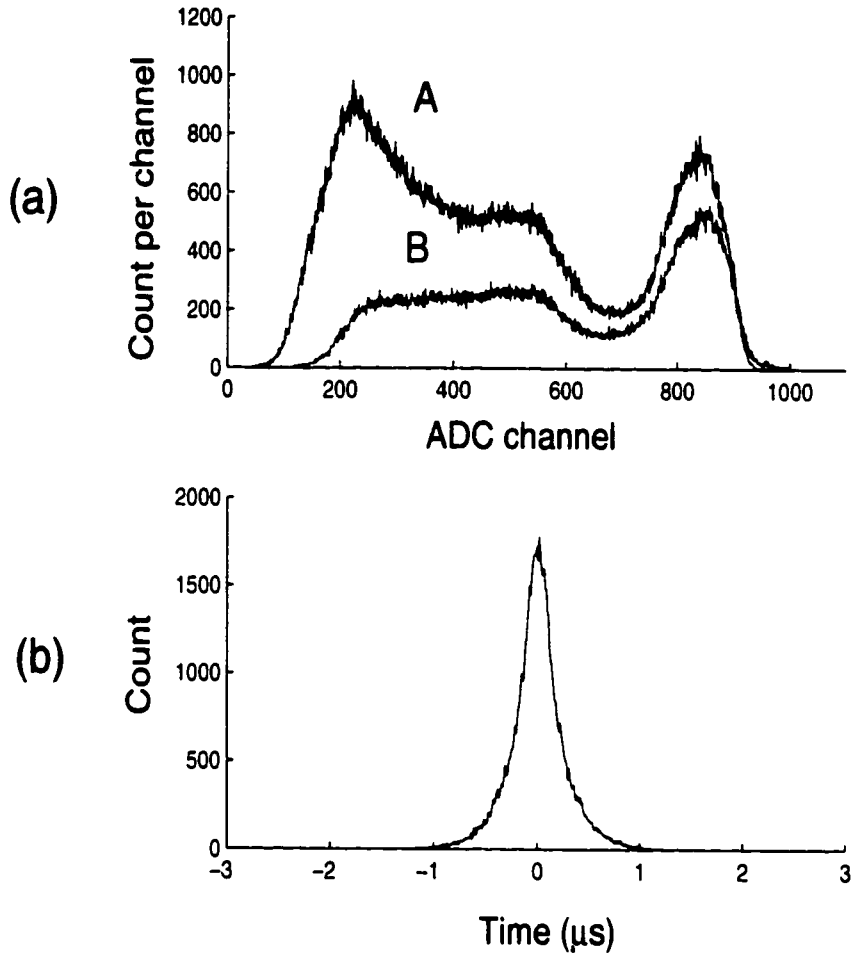

Figure 6.22: (a) 662 keV energy spectra from the two-pixel events in detector 2.1 without correction for electron trapping. (b) Distribution of the difference of the two measured electron drift times in the two-pixel events.

6.5.2 Energy Spectrum from the Two-Pixel Events

For each 662 keV two-pixel event in detector 2.1, the signals from the two involved anode pixels are summed up after being corrected for the non-uniform gains of the two readout channels (using the maximum 662 keV photopeak centroid from each pixel), and yield spectrum A in figure 6.22 (a). If there is no signal loss and the pulse height from each readout channel is proportional to the corresponding energy deposition, the broadening of the 662 keV photopeak in spectrum A should be dominated by the

electron trapping experienced by the signals from the two involved pixels. Therefore, the energy resolution should be significantly improved if the amplitudes of the two signals can be corrected for electron trapping. In detector 2.1, the electron trapping of the two-pixel events can be corrected using the measured electron drift times of the two signals. Due to the intrinsically higher electronic noise, the energy resolution from the two-pixel events should be worse than that from the single-pixel events, which is 1.64% FWHM at 662 keV using depth sensing by electron drift time (see figure 6.16). If the correction for electron trapping is accurate, an energy resolution of ~2% FWHM should be expected from the two-pixel events. Because of the threshold of ~30-~60 keV in the TAT timing channels, only those two-pixel events with both energy signals above the threshold can yield the timing signals for determining the two electron drift times. For those events, the simple summation of the two energy signals yields spectrum B in figure 6.22 (a). For the photopeak events in spectrum B, the distribution of the difference of the two electron drift times is shown in figure 6.22 (b). This distribution resembles the simulation result shown in figure 3.6, which is the distribution of the difference of the two interaction depths from 662 keV two-pixel full energy deposition events. This result indicates the correlation between the measured electron drift times and the corresponding interaction depths.

Using the measured electron drift times and the pulse height correction calibration achieved from the single-pixel events, the two energy signals of each two-pixel event are corrected separately for electron trapping. Before these two signals are summed together to yield a combined energy signal, they are also corrected separately for the nonlinearity of the readout channels using a two-point energy calibration measured with 122 keV and 662 keV single-pixel events. Figure 6.23 (a) and (b) show the energy spectra from the combined signals of two-pixel events at two grid biases of

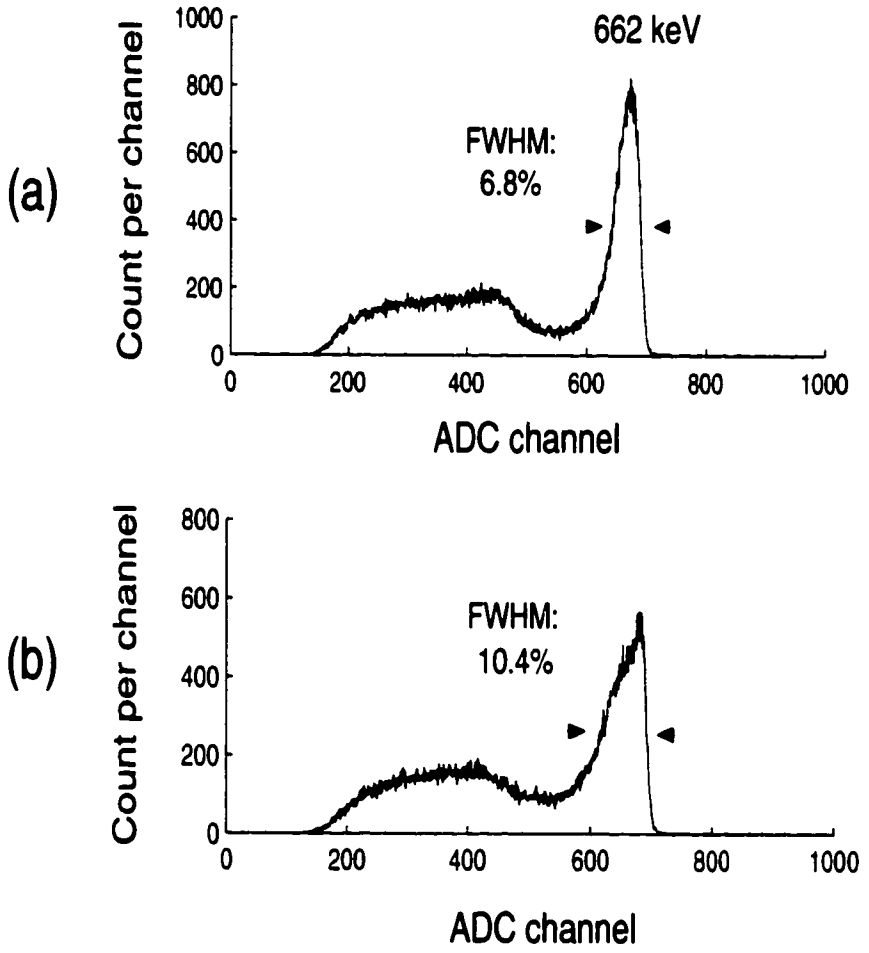

Figure 6.23: 662 keV energy spectra from the overall two-pixel events in detector 2.1. (a) At grid bias of -90 V. (b) At grid bias of -70 V.

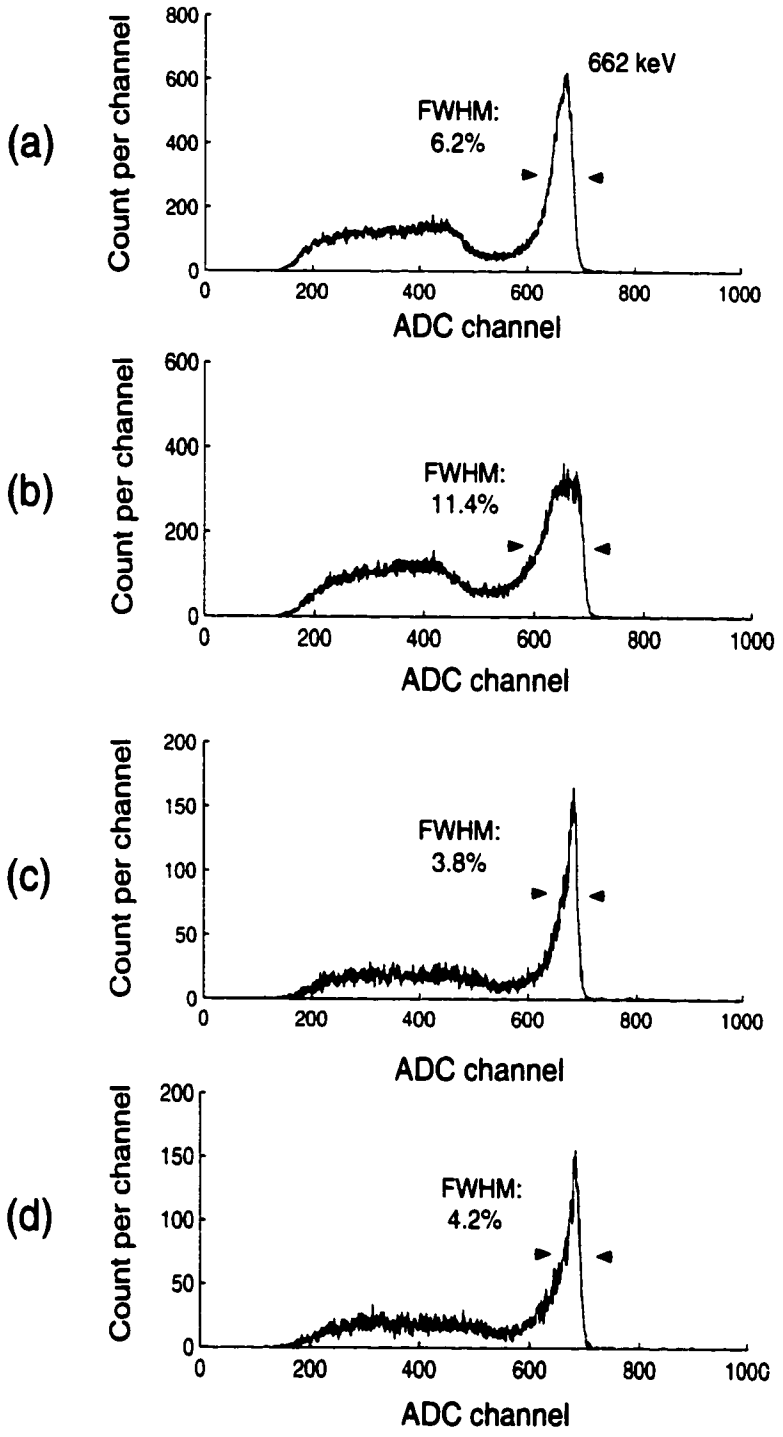

Figure 6.24: 662 keV energy spectra from the two-pixel events in detector 2.1. (a) and (b) From the two-adjacent-pixel events, at grid biases of -90 V and -70 V. (c) and (d) From those two-pixel events with the two pixels separated by another pixel, at grid biases of -90 V and -70 V.

-90 V and -70 V, respectively. The energy resolutions of the spectra are much worse than the expected value of ~2% FWHM, indicating the existence of a problem in the system. Moreover, the improvement of the energy resolution with the increased grid bias indicates that the degradation of the energy resolution is related to the electron loss near the grid electrode. In the region near the anode, if the electric field is not strong enough in the lateral dimension, those electrons in the region near the grid could move too slowly or even be collected by the grid electrode, thus providing no contribution to the anode pixel signals[Bol.1]. If this situation is true for detector 2.1, the degradation of the energy resolution should be more severe for the two-adjacent-pixel events, because a large fraction of the two-adjacent-pixel events are from the electron cloud sharing between two neighboring pixels. As a consequence, those events should inherently suffer from the problem of electron loss near the grid. To verify this explanation, the reconstructed spectra from the two-adjacent-pixel events at the two grid biases are shown in figure 6.24 (a) and (b), and the spectra from the two-pixel events with the two pixels separated by another pixel are shown in figure 6.24 (c) and (d). The worse energy resolutions of the spectra in figure 6.23 (a) and (b) (compared to (c) and (d)) provide support to the hypothesis of electron loss near the grid electrode. While the energy spectra in figure 6.23 (c) and (d) show improved energy resolution over that from the two-adjacent-pixel events, the improved energy resolution with increased grid bias and the presence of low energy tails on the photopeaks still indicates electron loss near the grid. However, the sharp peak and the steep high energy falloff of the photopeaks indicate the potential improvement of the energy resolution which can be achieved if the problem of electron loss near the grid is eliminated.

As a general approach, electron loss between two neighboring pixels can be studied

by measuring the correlation of the signals from these two pixels[Bol.1][Bol.2]. In the next section, this approach was used for direct evidence about the electron loss near the grid in detector 2.1.

6.5.3 Electron Loss Near the Grid Electrode

The cathode of detector 2.1 was irradiated with 122 keV gamma rays and the signals from the two-pixel events were recorded. The two signals (after correcting for the non-uniform gains of the readout channels) from the two-adjacent-pixel events are plotted against each other for three different grid biases. The results are shown in figure 6.25 (a), (b) and (c), respectively. Figure 6.25 (d) shows the same plot for the two signals but with the two pixels separated by another pixel, and at a grid bias of -90 V. Different from figure 6.25 (a), (b) and (c), figure 6.25 (d) shows no obvious correlation. This indicates the 122 keV two-pixel events are dominated by two-adjacent-pixel events. Due to the fact that most of the 122 keV gamma interactions in the detector are photoelectric events, most of the two-adjacent-pixel events should be generated by the electron cloud sharing. If there is no electron loss near the grid electrode, the summation of the two signals in the two-adjacent-pixel events should be equal to the 122 keV energy deposition, therefore the distribution of those events with different sharing fractions should follow the dashed line in the correlation plot. However, the measured correlation plots deviate from the dashed lines, which clearly demonstrates the electron loss near the grid. The deviation of each point from the dashed line indicates the amount of the electron loss in each case. It is also shown from the results that the amount of the electron loss can be reduced by increasing the grid bias. However, the electron loss is still significant at the grid bias of -90 V, which is the maximum grid bias for detector 2.1. This result

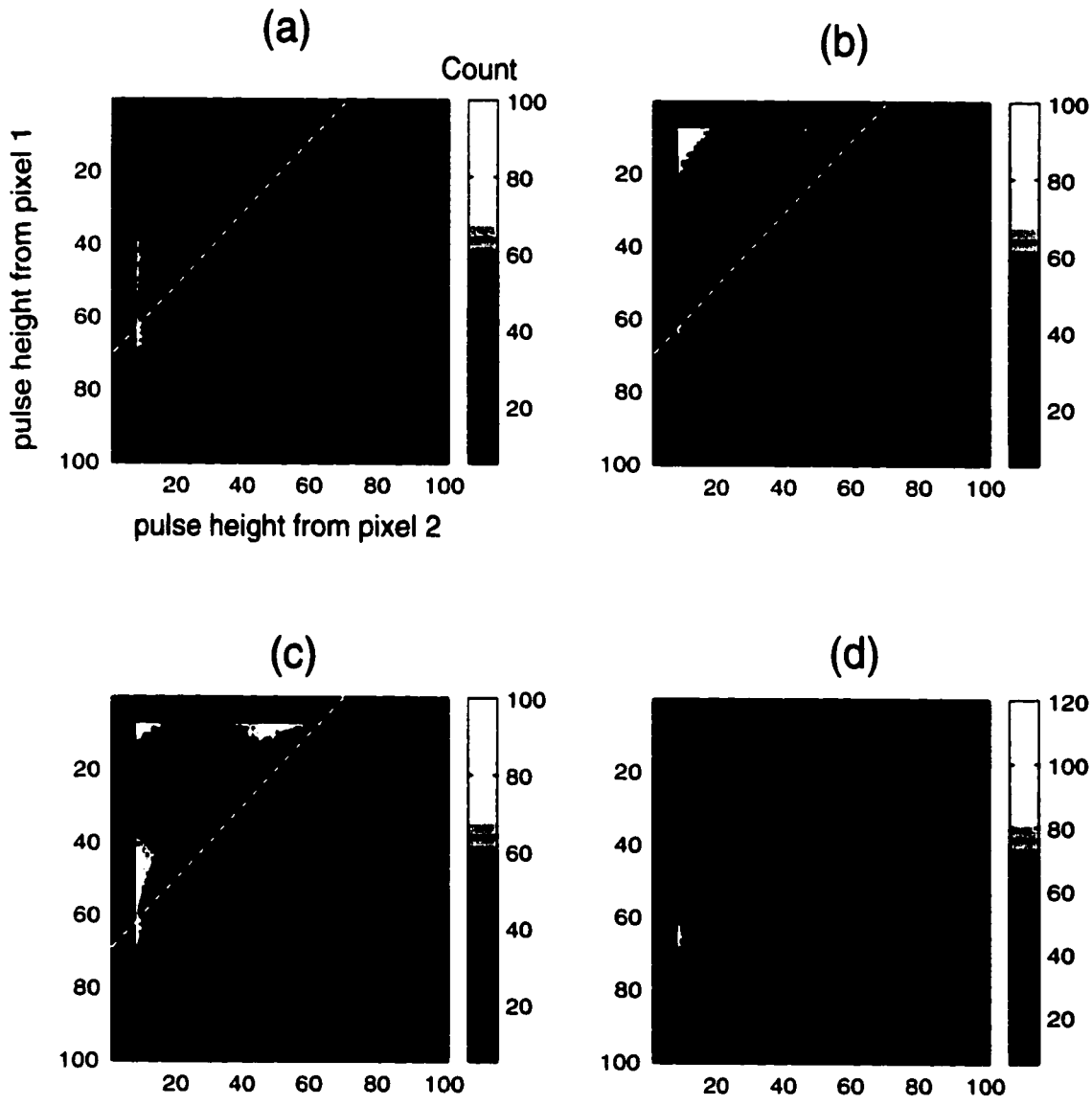

Figure 6.25: Correlation of the signal amplitudes from the two pixels in the 122 keV two-pixel events of detector 2.1. (a), (b), (c) Two-adjacent-pixel events, with different grid biases of -30 V in (a), -70 V in (b), -90 V in (c). (d) Two-pixel events, with the two pixels separated by one pixel. The grid bias is -90 V.

provides a direct evidence of the electron loss near the grid, which accounts for the degradation of the energy resolution from the reconstructed two-pixel events.

The problem of the electron loss near the grid electrode in detector 2.1 may be due to some defects in the anode surface processing, which is related to the problem of unstable leakage current through the grid. This problem of electron loss near the grid was not observed in the operation of detectors 1.1 and 1.2 which have the same 100 μm width of the grid and the same 200 μm gap between the grid and the pixel pads, even at a lower grid bias of -50 V. This fact indicates the electron loss problem is not intrinsic to the 3-D CdZnTe detectors having the same anode pattern of detector 2.1. If this problem can be eliminated using better electrode fabrication in the future 3-D CdZnTe detectors, significant improvement of the energy resolution from the two-pixel events should be expected.

CHAPTER VII

SUMMARY AND FUTURE WORK

The research presented in this dissertation consisted of three parts: the modeling of the 3-D CdZnTe detectors, the development of the two generations of 3-D CdZnTe detectors and readout electronics, and the experiments performed with three 3-D CdZnTe detectors. In the following, the major results of these works are summarized. In addition, recommended future work based on open problems is discussed.

7.1 Modeling Results

The modeling involved two separate topics. The first was the Monte Carlo simulation of the fraction of the multiple-pixel events in the 3-D CdZnTe detectors. For a 1 cubic centimeter 3-D CdZnTe detector with 11×11 anode pixels and the pixel size of 0.7×0.7 mm^2, the simulation results showed that less than 30% of the 662 keV full energy deposition events are single-pixel events. It was also shown that this small fraction will not be significantly increased by using a larger pixel size, at least up to 1.8×1.8 mm^2. These results indicated the necessity to reconstruct the energy spectrum from the multiple-pixel events, such as the two-pixel events that account for ~40% of the 662 keV full energy deposition events. The second topic was the modeling of the two interaction depth sensing techniques (depth sensing by

C/A ratio and by electron drift time) by modeling the charge transport in the detector and the electronic processing of the signals. For interaction events occurring at most of the detector depths, the modeling results demonstrated that both the C/A ratio and the electron drift time have monotonic relationships with the interaction depth. Assuming normal charge transport properties and electronic noise, the modeling showed that for 662 keV single-pixel full energy deposition events, a depth resolution (FWHM) of ~2-3% of the detector thickness could be achieved using the C/A ratio method, except in the region near the anode or cathode. Using the drift time method, a depth resolution (FWHM) of ~5% the detector thickness could be achieved for 662 keV full energy deposition events, a result dominated by the timing resolution of the cathode signal.

7.2 Detectors and Electronics

Two generations of 3-D CdZnTe detectors were developed in this research. Each of the first generation detectors is a 1 cubic centimeter CdZnTe crystal fabricated with a conventional planar cathode and an 11×11 anode pixel array. The anode is fabricated with a non-collecting grid electrode, which is negatively biased relative to the anode pixels during operation. Each anode pixel has a size of 0.7×0.7 mm^2 and is connected to a substrate using wirebonding. The second generation detectors have the same electrode geometries but a larger detector volume of 1.5×1.5×1 cm^3, thus a larger pixel size of 1.2×1.2 mm^2. To make more rigid connections between the anode pixels and the substrate, the technique of plate-through-via is used in the second generation detectors instead of wirebonding in the first generation detectors.

To read out the signals from the 3-D CdZnTe detectors, two generations of readout systems have been developed and each works with the corresponding generation of

3-D CdZnTe detectors. The first generation readout system was built using an integrated VA1 chip, which has 128 independent energy readout channels. 121 of the channels are DC-coupled to the 11×11 anode pixels to read out the signals. The trigger signal of the readout system is derived from either the cathode or the anode grid signal using a discrete circuit. For each interaction event in the detector, the energy signals from each anode pixel and the cathode can be read out. The dynamic range of the readout channels in the VA1 chip is ~1 MeV for CdZnTe detectors, and the equivalent electronic noise is ~7 keV FWHM, limited by the leakage currents from the anode pixels and the DC-coupling used. The second generation system was built with 128 energy readout channels and 128 timing channels based on 4 VAS-TAT chip pairs. The energy readout channels are based on the VA1 chip and thus have similar performance. Similar to the first generation system, 121 energy readout channels are DC-coupled to the anode pixels to read out the energy signals. The leading edge timing of each energy signal is read out by the corresponding timing channel with a dynamic range of 10 μs, and the trigger signals from all the timing channels are combined together to yield the system trigger. A discrete circuit was also developed to read out the energy and timing signals from the cathode. Therefore, for each interaction event in the detector, in addition to the energy signals from the anode pixels and the C/A ratio, the electron drift time corresponding to each individual interaction is also available in the second generation system.

7.3 Experiments

The experiments performed in this research involved two first generation 3-D CdZnTe detectors and one second generation detector. The experiments included the investigation of the two depth sensing techniques, the 3-D pulse height correction

and the resulting improvement in energy resolution from the single-pixel events, the measurement of $(\mu\tau)_e$ and its spatial variation, and the reconstruction of the energy spectrum from the two-pixel events.

7.3.1 Interaction Depth Sensing

The two interaction depth sensing techniques were investigated using a second generation 3-D CdZnTe detector. In the measurement of the dual-parameter distribution of the single-pixel events over the C/A ratio and the electron drift time, an almost linear relationship between the two parameters was obtained in the experiment. The strong correlation indicates that both the C/A ratio and the electron drift time have monotonic relationships with the interaction depth and can be used in the depth sensing for single-pixel events. Furthermore, the FWHM of the profiles of the measured dual-parameter distributions shows that the depth resolutions of the two depth sensing techniques are better than ~0.5 mm FWHM for 662 keV full energy deposition events, and better than ~1 mm FWHM for ~200 keV energy deposition events. Another experiment using collimated 662 keV gamma rays also provides evidence that both the two depth sensing parameters have true correlations to the interaction depth.

7.3.2 3-D Pulse Height Correction

Based on depth sensing by C/A ratio, the 3-D pulse height correction was used in the spectrum collection from the 662 keV single-pixel events in the two first generation 3-D CdZnTe detectors. The energy resolutions of the corrected global spectra from the two detectors are 1.73% and 1.84% FWHM, respectively. Variation in the energy resolutions from different pixels was observed. The typical energy resolution achieved from the normal pixels was ~1.2-1.5% FWHM, which approaches the elec-

tronic noise of ~1% FWHM. This demonstrated the potential of the 3-D CdZnTe detectors. The energy spectra from those central pixels having worse energy resolutions showed a gradual degradation of energy resolution from the anode to the cathode, which indicates non-uniform electron trapping within the dimension of the anode pixel. The 3-D pulse height correction was also applied to the second generation 3-D CdZnTe detector using the two interaction depth sensing techniques. The energy resolutions of the corrected global spectra from the working pixels were 1.5% and 1.64% FWHM using depth sensing by C/A ratio and by electron drift time, respectively. Interaction depth-dependent degradation of energy resolution was also observed from a few pixels, which resembles the situation in the first generation detectors. This result indicates non-uniform electron trapping within the dimension of the anode pixel is a common problem in 3-D CdZnTe detectors. This problem can only be mitigated by choosing CdZnTe crystal of better quality to fabricate the detector.

7.3.3 Measurement of $(\mu\tau)_e$

In the experiment with a 3-D CdZnTe detector, the $(\mu\tau)_e$ of the CdZnTe material underneath each anode pixel was estimated separately, using the measured photopeak centroid in the anode pixel spectrum as a function of the interaction depth. The measured $(\mu\tau)_e$ from the three detectors are similar, with an average value of $\sim 6\times10^{-3}$ cm^2/V and a relative standard deviation of ~10% for the results from different pixels. Different values of $(\mu\tau)_e$ from different pixels indicates the material non-uniformity in the lateral dimension across the detector. This material non-uniformity will contribute to the degradation of energy resolution in the global spectrum if there is no correction in the lateral dimension. This result verifies the

necessity of using 3-D pulse height correction during the energy spectrum collection.

7.3.4 Reconstruction of Energy Spectrum from Two-Pixel Events

Using one of the first generation detectors, the fraction of the 662 keV multiple-pixel full energy deposition events as a function of the number of pixels involved was measured. The measured fraction matched well with the simulation result and showed that ~27% of the 662 keV full energy deposition events are single-pixel events, while ~40% are two-pixel events. This result shows the advantage in reconstructing the energy spectrum from the multiple-pixel events, especially the two-pixel events. The experiment of reconstructing the energy spectrum from two-pixel events was performed with the second generation detector. For those two-pixel events with both energy signals above the thresholds of the corresponding timing channels, the electron drift times were read out and used with the calibration measured using the single-pixel events, to correct the two energy signals separately for electron trapping. In addition, the two energy signals were corrected for the nonlinearity of the readout channels using a two-point energy calibration (122 keV and 662 keV) before they were summed together. The reconstructed energy spectrum from overall two-pixel events showed a poor energy resolution (~7% FWHM) and a dependence of the energy resolution on the grid bias. This result indicates the existence of electron loss near the grid electrode. The problem of electron loss is confirmed by the better energy resolution (3.8% FWHM at -90 V grid bias) achieved from those two-pixel events with the two pixels separated by another pixel. To investigate the situation of electron loss near the grid, the correlation of the signals from 122 keV two-adjacent-pixel events was measured at different grid biases. The results clearly demonstrated the existence of electron loss near the grid electrode even with a grid bias of -90

V. Since the problem of electron loss was not observed in the two first generation detectors at a grid bias of -50 V, it is possible to eliminate this problem in the future 3-D CdZnTe detectors and consequently yield better energy resolution in the reconstructed spectrum from the two-pixel events.

7.4 Recommended Future Work

To achieve fully-functional 3-D CdZnTe detectors which can be used in practical gamma ray spectroscopy, further work is needed. In this section, some future work will be recommended involving the 3-D CdZnTe detector, the readout electronics, and the 3-D pulse height correction.

The second generation 3-D CdZnTe detector used in this research has the desired rigid connections between the detector and the substrate. However, it has two serious problems: the bad connections between the substrate and a fraction of the anode pixels, and the electron loss near the grid electrode. Fortunately both problems are not intrinsic, so in the fabrication of the future 3-D CdZnTe detectors, special attention should be paid to the solutions of these two problems. In addition, the connection between the detector substrate and the readout electronics also needs to be improved. Currently the connection is done by wirebonding, which makes it difficult to switch the detector to different readout electronics boards. The performance of different 3-D CdZnTe detectors is quite different, as is the performance of different readout electronics boards. Therefore, it is necessary to develop a more convenient approach to connect the detector to the readout electronics (e.g., using multiple-pin connectors), which makes it easy to change either of them. If implemented, this improvement would make it easy to identify whether some problems are related to the detector or the electronics board. More importantly, it would be much easier to

match the best detector with the best readout electronics board, thus achieve the best spectroscopic performance.

The second generation readout system was successfully developed to read out the multiple-channel energy and timing signals from the 3-D CdZnTe detectors. However, two important components did not work properly in the current system, namely the leakage current compensation units in the VAS channels and the special readout channels. These problems need to be addressed in the development of the future systems. The leakage current compensation unit is designed to absorb the leakage current of a few nA from the anode pixel, thus achieve AC-equivalent coupling between the detector and the readout electronics. This would consequently reduce the equivalent electronic noise of the VAS channels. However, the compensation threshold in the current system is too high ($\sim$10 nA), so the readout system still has to work in the DC-coupling mode. In the future, solutions need to be developed to have the compensation threshold reduced to under $\sim$1 nA. Otherwise, the implementation of reliable AC-coupling using integrated resistor and capacitor arrays needs to be investigated. The special channels in the readout system are designed to integrate the readout of the cathode and anode grid signals into the VAS-TAT chip pairs. In the experiments with a 3-D detector, the special channel connected to the cathode had a gradual decrease in the output pulse height and finally broke down. It is suspected that this problem is due to the large pick-ups in the cathode signal from the digital control signals. Further experiments using other new readout boards need to be performed in the future to verify this explanation. If this is true, the future readout electronics board needs to be modified to provide the electric shielding for the cathode signal from the digital control signals. In addition, the uniformities of the different VAS and TAT channels also need to be improved in the future read-

out systems. This includes uniformities in electronic noise and baseline of the VAS channels, and the threshold in the TAT channels.

Currently, the 3-D pulse height correction for single-pixel events in the 3-D CdZnTe detectors is performed using depth sensing by either the C/A ratio or the electron drift time. The measured C/A ratio and electron drift time are two independent depth parameters, so theoretically they can be used together to get a better depth resolution and hence a better result of the 3-D pulse height correction. It would be interesting to investigate how to use these two measured parameters together to achieve the optimized spectroscopic performance from the single-pixel events of the 3-D CdZnTe detectors. In the future, the reconstruction of the energy spectrum from the multiple-pixel events also needs to be further investigated using 3-D CdZnTe detectors that do not have the problem of electron loss near the grid electrode.

BIBLIOGRAPHY

BIBLIOGRAPHY

[Amm.1] M. Amman, P.N. Luke, J.S. Lee, "CdZnTe Material Uniformity and Coplanar-Grid Gamma-Ray Detector Performance," IEEE Trans. Nucl. Sci. NS-47 (3) (2000) 760-767.

[AMP.1] Amptek Inc., 6 De Angelo Drive, Bedford, MA 01730, USA.

[Apo.1] B. Apotovsky, C.L. Lingren, A. Oganesyan, et al., "Semiconductor Radiation Detector with Enhanced Charge Collection," US Patent 5677539, (1996).

[Arm.1] G.A. Armantrout, S.P. Swierkowski, J.W. Sherohman, J.H. Lee, "What Can Be Expected from High-Z Semiconductor Detectors," IEEE Trans. Nucl. Sci. NS-24 (1977) 121-125.

[Bar.1] H.H. Barrett, J.D. Eskin, H.B. Barber, "Charge Transport in Arrays of Semiconductor Gamma-Ray Detectors," Physical Review Letters, vol.75, no.1 (1995) 156-159.

[Bel.1] R.O. Bell, G. Entine, H.B. Serreze, "Time-Dependent Polarization of CdTe Gamma-Ray Detectors," Nucl. Instr. and Meth. 117 (1974) 267-271.

[Bol.1] A.E. Bolotnikov, S.E. Boggs, C.M. Hubert Chen, et al., "Investigation of Optimal Contact geometries for CdZnTe Pixel Detectors," Proceedings of SPIE Vol.4141 (2000) 243-252.

[Bol.2] A.E. Bolotnikov, W.R. Cook, F.A. Harrison, et al., "Charge Loss between Contacts of CdZnTe Pixel Detectors," Nucl. Instr. and Meth. 432 (1999) 326-331.

[Bra.1] T. Mohammed-Brahim, A. Friant, J. Mellet, "Structure Mis Effects on Polarization of HgI_2 Crystals Used for Gamma-Ray Detection," IEEE Trans. Nucl. Sci. NS-32 (1) (1985) 581.

[Bur.1] A. Burger, K. Chattopadhyay, H. Chen, et al., "Defects in CZT Crystals and Their Relationship to Gamma-Ray Detector Performance," Nucl. Instr. & Meth. A448 (2000) 586-590.

[But.1] J.F. Butler, C.L. Lingren, F.P. Doty, "$Cd_{1-x}Zn_xTe$ Gamma Ray Detectors," IEEE Trans. Nucl. Sci. NS-39 (4) (1992) 605-609.

[But.2] J.F. Butler, F.P. Doty, B. Apotovsky, Mater Sci. Eng. B 16 (1993) 291.

[Chi.1] L. Chibani, M. Hage-Ali, P. Siffert, "Electrically Active Defects in Detector-Grade CdTe:Cl and CdZnTe Materials Grown by THM and HPBM," Journal of Crystal Growth 161 (1996) 153-158.

[Coo.1] A. James Cook, "Mortran3 User's Guide," SLAC Computation Research Group Technical Memorandum Number CGTM 209 (1983).

[COU.1] Coulomb, Integrated Engineering Software, 46-1313, Border Place, Winnipeg, Manitoba, Canada.

[Cuz.1] M. Cuzin, "Some New Developments in the Field of High Atomic Number Materials," Nucl. Instr. and Meth. A253 (1987) 407-417.

[Du.1] Y.F. Du, Z. He, W. Li, et al., "Monte Carlo Investigation of the Charge Sharing Effects in 3-D Position Sensitive CZT Gamma-Ray Spectrometers," IEEE Trans. Nucl. Sci. NS-46 (3) (1999) 187-192.

[Eis.1] Y. Eisen, "Current State-of-the-Art Industrial and Research Applications Using Room-Temperature CdTe and CdZnTe Solid State Detectors," Nucl. Instr. and Meth. A380 (1996) 431-439.

[EGS.1] Http://ehssun.lbl.gov/egs/code.html.

[Fri.1] O. Frisch, **British Atomic Energy Report** BR-49 (1944).

[Ger.1] V.M. Gerrish, D.J. Williams, A.G. Beyerle, "Pulse Filtering for Thick Mercuric Iodide Detectors," IEEE Trans. Nucl. Sci. NS-34 (1) (1987) 85-90.

[Hag.1] M. Hage-Ali, J.M. Koebel, R. Regal, et al., "Cadmium Telluride Small Probes for Gamma-Ray Spectrometry," Nucl. Instr. and Meth. A380 (1996) 427-430.

[He.1] Z. He, "Potential Distribution within Semiconductor Detectors Using Coplanar Grid Electrodes," Nucl. Instr. and Meth. A365 (1995) 572.

[He.2] Z. He, G.F. Knoll, D.K. Wehe, et al., "1-D Position Sensitive Single Carrier Semiconductor Detectors," Nucl. Instr. & Meth. A380 (1996) 228-231.

[He.3] Z. He, G.F. Knoll, D.K. Wehe, et al., "Position-Sensitive Single Carrier CdZnTe Detectors," Nucl. Instr. & Meth. A388 (1997) 180-185.

[He.4] Z. He, W. Li, G.F. Knoll, et al., "3-D Position Sensitive CdZnTe Gamma-Ray Spectrometers," Nucl. Instr. & Meth. A422 (1999) 173-178.

[He.5] Z. He, W. Li, G.F. Knoll, et al., "Effects of Charge Sharing in 3-D Position Sensitive CdZnTe Gamma-Ray Spectrometers," Nucl. Instr. & Meth. A439 (2000) 619-624.

[Hec.1] K. Hecht, Z. Phys. 77, 235 (1932).

[IDE.1] IDE AS, Veritasveien 9, N-1322 Hovik, Norway.

[IDE.2] The VA Circuits Catalogue, IDE AS, 1995/1996.

[INT.1] National Instruments Corporation, 11500 N Mopac Expwy, Austin, TX 78759-3504, USA.

[Jer.1] J.W. Jerome, **Analysis of Charge Transport**, Springer, Verlag Berlin Heidelberg, 1996.

[Jon.1] L.T. Jones, P.B. Woollam, "Resolution Improvement in CdTe Gamma Detectors Using Pulse-Shape Discrimination," Nucl. Instr. and Meth. 124 (1975) 591-595.

[Kno.1] G.F. Knoll, **Radiation Detection and Measurement**, Wiley, New York, 1989.

[Lee.1] E.Y. Lee, et al., "Device Simulation of a Unipolar Gamma-Ray Detector," Proceedings of MRS, 487 (1998) 537.

[Li.1] W. Li, Z. He, G.F. Knoll, et al., "A Data Acquisition and Processing System for 3-D Position Sensitive CZT Gamma-Ray Spectrometers," IEEE Trans. Nucl. Sci. NS-46 (3) (1999) 187-192.

[Li.2] W. Li, Z. He, G.F. Knoll, et al., "Spatial Variation of Energy Resolution in 3-D Position Sensitive CZT Gamma-Ray Spectrometers," IEEE Trans. Nucl. Sci. NS-46 (6) (1999) 1989-1994.

[Li.3] W. Li, Z. He, G.F. Knoll, et al., "Experimental Results from an Imarad 8×8 Pixellated CZT Detector," Nucl. Instr. and Meth. A458 (2001) 518-526.

[Luk.1] P.N. Luke, "Unipolar Charge Sensing with Coplanar Electrodes- Application to Semiconductor Detectors," IEEE Trans. Nucl. Sci. NS-42 (4) (1995) 207-213.

[Luk.2] P.N. Luke, E.E. Eissler, "Performance of CdZnTe Coplanar-Grid Gamma-Ray Detectors," IEEE Trans. Nucl. Sci. NS-43 (3) (1996) 1481-1486.

[Lun.1] J.C. Lund, R. Olsen, J.M. Van Scyo, R.B. James, "The Use of Pulse Processing Techniques to Improve the Performance of $Cd_{1-x}Zn_xTe$ Gamma-Ray Spectrometers," IEEE Trans. Nucl. Sci. NS-43 (3) (1996) 1411-1416.

[Mae.1] G. Maehlum, J.R. Henriksen, K. Ellingsberg, et al., "The MCR3 System for VA/TA-Readout," Preliminary Product Information, IDE AS, 2001.

[Mal.1] H.L. Malm, M. Martini, "Polarization Phenomena in CdTe Nuclear Radiation Detectors," IEEE Trans. Nucl. Sci. NS-21 (1) (1974) 322.

[Mar.1] D.G. Marks, H.B. Barber, H.H. Barrett, et al., "A 48×48 CdZnTe Array with Multiplexer Readout," IEEE Trans. Nucl. Sci. NS-43 (3) (1996) 1253-1259.

[Mcg.1] D.S. McGregor, et al., "CdZnTe Semiconductor Parallel Strip Frisch Grid Radiation Detectors," IEEE Trans. Nucl. Sci. NS-45 (3) (1998) 443.

[Mcg.2] D.S. McGregor, et al., "Geometrically Weighted Semiconductor Frisch Grid Radiation Spectrometers," Nucl. Instr. and Meth. A422 (1999) 164-168.

[Nel.1] W.R. Nelson, H. Hirayama, D.W.O. Rogers, "The EGS4 Code System", SLAC-Report-256, December 1985.

[NOV.1] NOVA R&D, Inc., 1525 Third Street, Suite C, Reiverside, CA 92507, USA.

[Par.1] K. Parnham, J.B. Glick, Cs. Szeles, K.G. Lynn, "Peroformance Improvement of CdZnTe Detectors Using Modified Two-Terminal Electrode Geometry," Journal of Crystal Growth 214/215 (2000) 1152-1154.

[Pre.1] T. Prettyman, M.R. Sullivan, D. Mercer, "Physics-Based Simulation of the Response of CdZnTe Radiation Detectors," Scientific Symposium on Room-Temperature Semiconductor X-Ray, Gamma-Ray and Neutron Detectors, March 11-12, 1997.

[Rai.1] Martin Feuerstack-Raible, "Overview of Microstrip Read-out Chips," Nucl. Instr. & Meth. A447 (2000) 35-43.

[Ram.1] S. Ramo, "Currents Induced by Electron Motion," Proceedings of the I.R.E., Sept. 1939, p.584.

[Sak.1] E. Sakai, "Present Status of Room Temperature Semiconductor Detectors," Nucl. Instr. and Meth. 196 (1982) 121-130.

[Sch.1] M.M. Schieber, I. Beinglass, G. Dishon, et al., Nucl. Instr. and Meth. 150 (1978) 71.

[Sho.1] A. Shor, Y. Eisen, I. Mardor, "Spectroscopy with CdZnTe γ- and X-ray Detectors by Modifying the Electron Trapping to Compensate for Incomplete Charge Collection Caused by Large Hole Trapping," Nucl. Instr. and Meth. A426 (1999) 491-496.

[Sho.2] W. Shockley, "Currents to Conductors Induced by a Moving Point Charge," Journal of Applied Physics, Vol.9, (1938) 635.

[Sif.1] P. Siffert, J. Berger, C. Scharager, A. Cornet, R. Stuck, "Polarization in Cdmium Telluride Nuclear Radiation Detectors," IEEE Trans. Nucl. Sci. NS-23 (1) (1976) 159.

[Ton.1] J.E. Toney, B.A. Brunett, T.E. Schlesinger, et al., "Uniformity of $Cd_{1-x}Zn_xTe$ Grown by High-Pressure Bridgman," Nucl. Instr. and Meth. A380 (1996) 132-135.

[Wal.1] F.V. Wald, G. Entine, Nucl. Instr. and Meth. 150 (1978) 13.

[War.1] W.K. Warburton, J.S. Iwanczyk, "Timing Techniques for Improving Thick HgI_2 Gamma-Ray Detector Performance," Nucl. Instr. and Meth. A254 (1987) 123-128.

[XIL.1] Xilinx, Inc., 2100 Logic Drive, San Jose, CA 95124-3400, USA.